



UNIVERSITAT POLITÈCNICA DE CATALUNYA
BARCELONATECH
Escola d'Enginyeria de Barcelona Est

MASTER THESIS

Master's degree in advanced Material Science and Engineering

**CAN SURFACE MODIFICATION ENHANCE THE MECHANICAL
PROPERTIES THROUGH MICROSTRUCTURAL CHANGES OF
MAGNESIUM ALLOYS?**



Memory and Annexes

Author: Lucas Todeschini
Director: Joan Josep Roa Rovira
Co-Director: Antonio Manuel Mateo García
Convocation: January/February 2021

Resumen

El objetivo principal de este trabajo final de máster (TFM) consiste en estudiar el efecto de la modificación microestructural, así como la directa modificación de las propiedades mecánicas bajo diferentes campos de tensión (dureza Vickers y fatiga Herziana de contacto monótonico) de aleaciones de Mg-Zn-Y, que contienen estructuras ordenadas de apilamiento de largo período (LPSO en inglés Long Period Stacking Ordered Structures). En este contexto, se estudiaron tres aleaciones diferentes con distintas composiciones y temperaturas de extrusión (350 y 450°C). En primer lugar, se han evaluado la microestructura y las propiedades mecánicas de las muestras pulidas (denominadas muestras de referencia) mediante técnicas avanzadas de caracterización como la microscopía electrónica de barrido, ensayos de macro y microindentación, etc. Posteriormente, la modificación superficial se llevó a cabo mediante un proceso de arenado con partículas de alúmina de 110 µm de tamaño promedio. Este proceso se realizó a diferentes presiones de trabajo (1, 3 y 5 bares) con el objetivo de poder ver la repercusión de dichas presiones en las propiedades finales del material. La rugosidad inducida durante dicho proceso se ha caracterizado mediante un perfilómetro de no contacto y el efecto de endurecimiento inducido por el proceso de arenado se ha determinado mediante ensayos de indentación a diferentes escalas.

Los resultados obtenidos en este TFM muestran que las aleaciones presentan tanto una fracción volumétrica diferente de la fase LPSO como un tamaño de grano medio. Este fenómeno se debe principalmente a su diferente composición y temperaturas de extrusión. Además, las propiedades mecánicas en términos de dureza Vickers aumentan con la cantidad de la LPSO y disminuyen con el incremento de la temperatura de extrusión. También se observó anisotropía, tanto microestructural como mecánica, en términos de dureza entre las mismas muestras evaluadas en sección transversal como longitudinal al proceso de extrusión. Posteriormente, se observó que la presión de arenado afecta considerablemente la calidad superficial, tanto en términos microestructurales como mecánicos. De hecho, la amplitud de la rugosidad aumentó con la presión de ensayo. Finalmente, se encontró que el proceso de arenado mejora considerablemente las propiedades mecánicas superficiales entre un 15 y un 50 % respecto al valor de las aleaciones de referencia.

Abstract

The main goal of this Master's thesis is to investigate the effect of microstructural surface modification as well as the mechanical properties under different stress fields (Vickers hardness and monotonic contact fatigue) of Mg-Zn-Y alloys, which contains Long Period Stacking Ordered Structures (LPSO). Three different alloys with different compositions and extrusion temperatures (350 and 450°C) were studied. First, the microstructure and mechanical properties of mirror-like polished samples (denoted as reference samples) have been evaluated by advanced characterization technics such as Scanning Electron Microscopy, macro- and microindentation tests, etc. Afterwards, the surface modification was conducted by sandblasting with alumina particles of 110 µm in average at different pressures (1, 3 and 5 bars). The roughness induced during the surface treatment process has been investigated by non-contact profilometer and the hardening effect induced by the sandblasting process has been investigated by hardness tests at different length scales.

The microstructural results showed that the alloys had different volume fraction of LPSO phase and average grain size due to their different composition and extrusion temperatures. Furthermore, the mechanical properties in term of Vickers hardness increase with the amount of the LPSO phase and decrease with the increase of the extrusion temperature. Besides, microstructural and hardness anisotropy was observed between the plain view and the cross-section profiles due to the extrusion process. Then, it was found that the pressure employed in order to superficially modify the superficial roughness considerably affects the superficial quality in terms of microstructure and mechanical properties. In fact, the amplitude of the roughness increased with the sputtering pressure. Finally, it was found that the sandblasting process enhanced the hardness of the material surface from 15% to 50%.

Acknowledgements

First, I would like to thank my thesis director Joan Josep Roa Rovira and Antonio Manuel Mateo García for giving me the opportunity to work on this project. Their support and guidance helped me to carry out this project in the best conditions possible. Also, I would like to thank the CIEFMA laboratory technicians Fernando and Marc, who trained me to use the equipment necessary to carry out this project.

Finally, I would like to thank my family, flatmates and friends who kept pushing and emotionally supporting me during this long process.

Glossary

Al: Aluminium

At%: Atomic percentage

Be: Beryllium

BSE: Backscattered Electrons

C: Carbon

Ca: Calcium

CCM: Chromatic Confocal Microscope

Ce: Cerium

Co: Cobalt

COF: Coefficient of friction

Cr: Chromium

Cu: Copper

DLIP: Direct Laser Interference Patterning

EBSD: Electron Backscatter Diffraction

EDS: Energy Dispersive Spectroscopy

FCC: Face-Centered Cubic

FESEM: Field Emission Scanning Electron Microscope

FIB: Focused Ion Beam

Ga: Gallium

LMIS: Liqui Metal Ion Source

LPSO: Long Period Stacking Ordered

LSCM: Laser Scanning Confocal Microscope

LSP: Laser Shock Processing

LST: Laser Surface Texturing

Mg: Magnesium

Mn: Manganese

O: Oxygen

OM: Optical Microscope

RE: Rare Earth

SB: Sandblasted

SE: Secondary Electrons

SEM: Scanning Electron Microscope

SF: Stacking Faults

SFE: Stacking-Faults Energy

SP: Shot Peening

Vol%: Volume percentage

XRD: X-Ray Diffraction

Y: Yttrium

Zn: Zinc

Zr: Zirconium

Summary

RESUMEN	2
ABSTRACT	3
ACKNOWLEDGEMENTS	4
GLOSSARY	5
1. INTRODUCTION	1
1.1. Magnesium and its alloys	1
1.1.1. Properties of pure Magnesium	3
1.1.2. Magnesium alloys	5
1.1.3. Nomenclature of Mg alloys	6
1.1.4. Applications	7
1.2. Mg-Zn-Y alloys	12
1.2.1. Mg-Zn-Y system	13
1.2.2. Stacking and chemical order of LPSO structures	15
1.2.3. Formation of LPSO structure	18
1.2.4. Mechanical properties	21
1.2.5. Corrosion behaviour	25
1.2.6. Wear behaviour	28
1.3. Surface modification techniques	31
1.3.1. Shot peening	31
1.3.2. Sandblasting	32
1.3.3. Laser surface texturing	34
2. STATE OF THE ART	42
3. OBJECTIVES	45
4. EXPERIMENTAL METHODS	46
4.1. Materials	46
4.2. Sample preparation	47
4.2.1. Polishing process	47
4.2.2. Sandblasting process	48
4.3. Characterisation techniques	50
4.3.1. Microstructural techniques	50
4.3.2. Mechanical characterization	59

5. RESULTS AND DISCUSSION	63
5.1. Microstructure analysis of reference alloys	63
5.2. Surface characterization of the sandblasted samples	72
5.3. Mechanical properties	76
5.3.1. Vickers Hardness	76
5.3.2. Hertzian contact: spherical indentation.....	82
ENVIRONMENTAL IMPACT ANALYSIS	89
CONCLUSIONS	91
FUTURE WORKS	93
REFERENCES	95
ANNEX	103
A1. EDS maps of the alloys	103
A2. EDS point composition of the alloys	109



1. Introduction

This introductory chapter will present the required information to understand the material of study along this master's thesis as well as different surface modification techniques. This chapter is divided into three different sections:

- I. The first section gives a general overview of magnesium (Mg) in terms of its production, microstructure, main properties, etc. Afterwards, it is presented the principal Mg alloys and their current applications in a wide range of field.
- II. The second section is focused on the properties of Mg-Zn-Y alloys investigated along this master's thesis. First is presented the crystallographic characteristics of Long Period Stacking Ordered (LPSO) structures that are found in the microstructure of this alloy. Then are described their mechanical properties as well as their corrosion behaviour.
- III. Finally, an overview of several surface modification techniques used to superficially modify the microstructure and as a consequence to enhance the mechanical properties of materials.

1.1. Magnesium and its alloys

Discovered in 1809 by Davy and isolated for the first time in 1826, magnesium (Mg) is the eighth most present element in the earth crust and represents more than 2% of its composition. It belongs to the alkaline earth metals group and cannot be found under its elemental form on earth. Instead, it can be found in several minerals or in the sea water. The principal minerals from which Mg can be extracted are: Magnesite ($MgCO_3$), Dolomite ($CaCO_3, MgCO_3$) and Carnallite ($MgCl_2, KCl, 6H_2O$) [68].

Australia holds the largest and highest levels of Mg reserves in the world in 2019, accounting for 30.4% of the available raw material, followed by China with 28.3% of the available raw material. They are followed by North Korea and Russia with 19.6% and 17.4%, respectively. The global primary production of Mg is steadily growing in the last decade by at least 50% compared to the level of 2010, except in 2018 where a slight decrease occurred (**Figure 1.1**). **Figure 1.2** shows the global production of Mg metal by country. It is obvious that producers in China dominate global production of it in 2019.

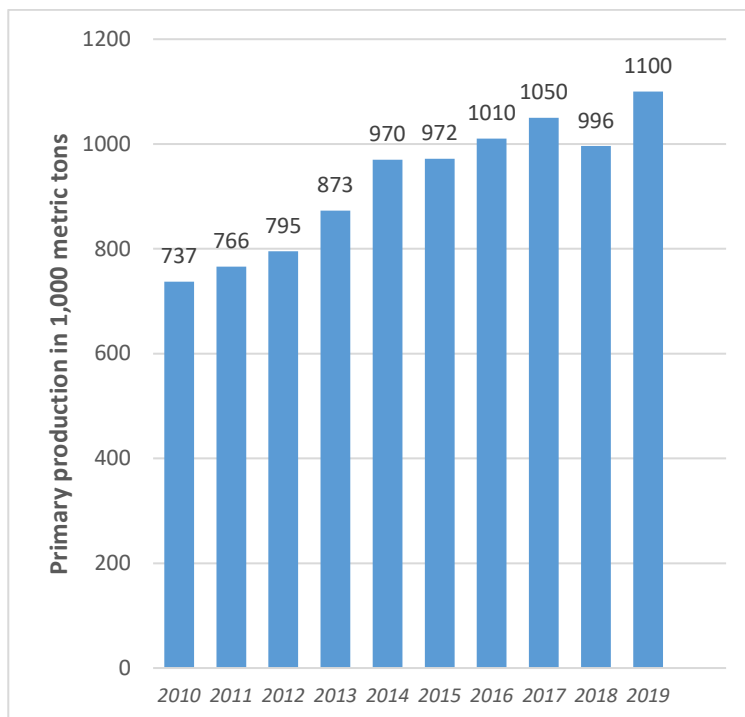


Figure 1.1: Global production of Mg since 2010. [69]

The principal processes of fabrication of Mg needs to go through the obtaining of magnesia by calcinating the minerals or by precipitating sea water using lime. Then the magnesia is treated by 2 different routes:

- In the **electrolytic process**, it is transformed in anhydrous chloride by chlorination, which is then electrolysed.
- In the **thermal process**, the magnesia is reduced at high temperature, in vacuum in the presence of strong reductants [1].

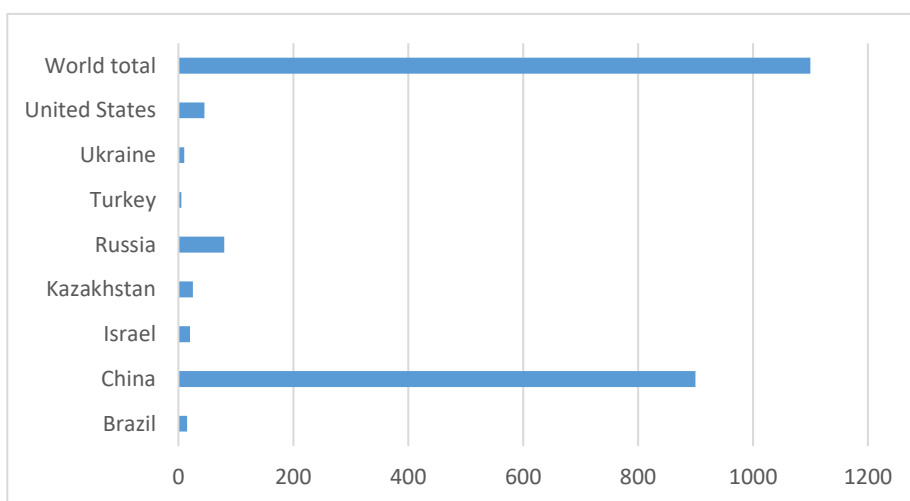


Figure 1.1.2: Primary production of Mg metal in 1,000 metric tons by country in 2019 [70].

1.1.1. Properties of pure Magnesium

The crystallographic structure of pure Mg is hexagonal compact with the atom positions as shown in **Figure 1.3**. The plans are in the order ABA. Its lattice parameters are at room temperature: $a = 0.3209 \text{ nm}$, $c = 0.521 \text{ nm}$ which gives a ratio $c/a = 1.62$. The compacity of this structure is near 74%, which is maximal compacity possible [1].

Below 225°C, slide in the Mg structure is only possible in the base plane $\{0001\}\langle 11\bar{2}0 \rangle$, together with twinning in the plane $\{1012\}\langle 1011 \rangle$. Pure Mg and conventional cast Mg-alloys have a tendency to brittleness, characterised by an intercrystalline fracture and a local transcrystalline fracture in the twin zones or in the base plane $\{0001\}$ with large grains. A new base plane is activated above 225°C $\{1011\}$, causing good Mg deformability [3].

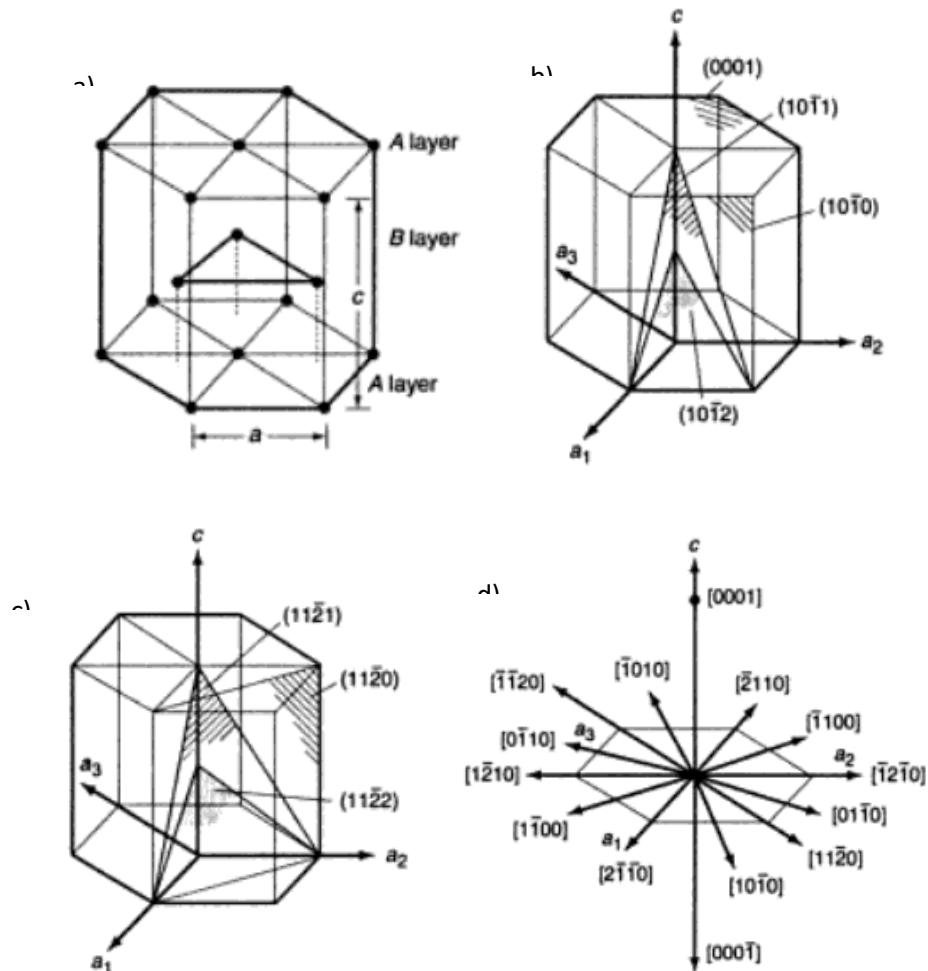


Figure 1.3: Mg unit cell crystal (a) atom positions; (b) Basal plane, a face plane and principal planes of the $[1\bar{2}10]$ zone; (c) Principal planes of the $[1\bar{1}00]$ zone and (d) Principal directions (continuation) [35].

The main physical and mechanical properties of Mg are shown in **table 1.1**. As shown in this table, Mg has a density of 1.74g/cm^3 , which represents $2/3$ of the density of aluminium ($\rho_{Al} = 2.7\text{g/cm}^3$), making Mg the less dense industrial metal.

Table 1.1: Physical and mechanical properties of Mg [1,3].

Properties	Value
Density, $\text{g}\cdot\text{cm}^{-3}$	1.738
Melting temperature, $^{\circ}\text{C}$	650
Boiling temperature, $^{\circ}\text{C}$	1,107
Thermal conductivity at 20°C, $\text{W}\cdot(\text{m}\cdot\text{K})^{-1}$	155
Resistivity at 20°C, $\text{n}\Omega\cdot\text{m}$	44.5
Tensile strength, MPa	180-220
Yield strength, MPa	115-140
Elongation, %	2-10
Young's modulus, GPa	40

In addition to its low density, Mg has several **advantages**:

- *High vibration damping capacity.*
- *Higher mechanical resistance compared to other metals for the same mass.*
- *Good machinability.*
- *High thermal conductivity.*

However, as said before, Mg has a low ductility making it difficult to cold work. Other aspects to take in account are its low Young's modulus and its tendency to oxidise at high temperatures during foundry, heat treatment and machining operations. Furthermore, Mg is a flammable substance which flash point is $\sim 760^{\circ}\text{C}$. The flash point is reduced to $\sim 470^{\circ}\text{C}$ when the Mg is in divided form [1].

1.1.2. Magnesium alloys

Mg is used most frequently in aluminium (Al) alloys as an alloy additive, which is added to improve strength and corrosion resistance. It is also used as an additive in zinc (Zn) alloys to improve mechanical properties and dimensional stability. Mg gained its largest application area by creating alloys in combination with other elements. These elements have different effects on the structure and properties of Mg-alloys, and many of them are useful applications, but some of them are used for very specific cases [3]. The effect of some typical alloying elements is shown in **table 1.2**.

Table 1.2: Alloying elements and their effects in Mg-based alloys [3].

Element	Effect
Al	Increases hardness, strength and castability while only increasing density minimally. Increased amount of Al decreases the ductility of the alloy. Average alloy contains about 2-9 weight percent (wt. %) of Al.
Beryllium, Be	Significantly reduces surface melt-oxidation during processing. Grain coarsening can occur. Can be carcinogenic material and is being rejected by some companies for use. Included only in very small quantities.
Calcium, Ca	Improves thermal and mechanical properties as well as assists in grain refinement and creep resistance. Reduces oxidation during processing when added to cast alloys. Allows for better rollability of sheet metal. Reduces surface tension. Addition exceeding 0.3 wt.%, increases the risk of cracking during welding.
Cerium, Ce	Improves corrosion resistance. Increases plastic deformation capability, Mg elongation, and work hardening rates.
Copper, Cu	Assists in increasing both room and high temperature strength. Negatively impacts ductility and corrosion resistance.
Manganese, Mn	Increases saltwater corrosion resistance within some Al containing alloys. Reduces the adverse effects of iron, usually present in 2-4 wt.%.
Zirconium, Zr	Refine grain size in sand and gravity castings. Not to be combined with Al.
Zinc, Zn	Increases the alloys fluidity in casting. It can improve corrosion resistance. Additions of 2 wt.% or greater tend to be prone to hot cracking.

Table 1.2: Alloying elements and their effects in Mg-based alloys [3] (continuation).

Element	Effect
Yttrium, Y	Enhances high temperature strength and creep resistance. Can be combined with other rare earth metals.
Rare earth, RE	Increase in high temperature creep and corrosion resistance and strength. Allows lower casting porosity and weld cracking in processing.

1.1.3. Nomenclature of Mg alloys

Commercial Mg-alloys can be easily identified according to an ASTM (American Society for Testing Materials) norm. The nomenclature is divided into 4 parts:

1. The **first part** consists of a 2 letters code representing the two main alloying elements arranged in order of decreasing percentage (or alphabetically if percentages are equal). **Table 1.3** summarizes the letters and the corresponding elements.
2. The **second part** consists of two numbers corresponding to rounded-off percentages of the main alloying elements and arranged in same order as alloy designations in first part.
3. The **third part** distinguish between different alloys with the same percentage of the two principal alloying elements. It consists of a letter except I and O.
4. The **final part** indicates the treatment and consists of a letter followed by a number. It is separated from the third part of the designation by a hyphen. **Table 1.4** summarizes the classification of treatments.

Table 1.3: Designation of elements according to the ASTM (1990) [18].

Letter	Element	Letter	Element	Letter	Element	Letter	Element
A	Aluminium	J	Strontium	R	Chromium	F	Iron
B	Bismuth	K	Zirconium	S	Silicon	H	Thorium
C	Copper	L	Lithium	T	Tin	P	Lead
D	Cadmium	M	Manganese	V	Gadolinium	Y	Antimony
E	Rare earth	N	Nickel	W	Yttrium	Z	Zinc

Table 1.4: Designation of thermal treatments on Mg-alloys according to the ASTM (1990) [18].

Type of treatment	Code	Type of treatment	Code
<i>As fabricated</i>		F <i>Solution heat treated and cold worked</i>	T3
<i>Annealed</i>		O <i>Solution heat treated</i>	T4
<i>Strain hardened (wrought products only)</i>		H <i>Cooled and artificially aged only</i>	T5
<i>Strain hardened and partially annealed</i>		H2 <i>Solution heat treated and artificially aged</i>	T6
<i>Strain hardened and then stabilized</i>		H3 <i>Solution heat treated and stabilized</i>	T7
<i>Solution heat treated, unstable temper, only for alloys that spontaneously age at room temperature</i>		W <i>Solution heat treated, cold worked, and artificially aged</i>	T8
<i>Thermally treated to produce stable tempers (other than O, H and F)</i>		T <i>Solution heat treated, artificially aged, and cold worked</i>	T9
<i>Cooled and naturally aged</i>		T1 <i>Cooled, artificially aged, and cold worked</i>	T10

1.1.4. Applications

The chemical composition of modern Mg-alloys has been constantly improved, to enhance various properties and find new field of applications. **Figure 1.4** shows schematically the future directions of Mg-alloys development for industrial applications [3].

Mg-alloys are constructional materials widely used in various industries due to low density and high specific strength. In addition, they exhibit good corrosion resistance, no aggressiveness with respect to the mould material and small melting heat. A high vibration damping ability and low inertia allow to use magnesium alloys for rapidly moving parts in places where there are rapid changes in speed. For these reasons, Mg-alloys are used worldwide on many different applications.

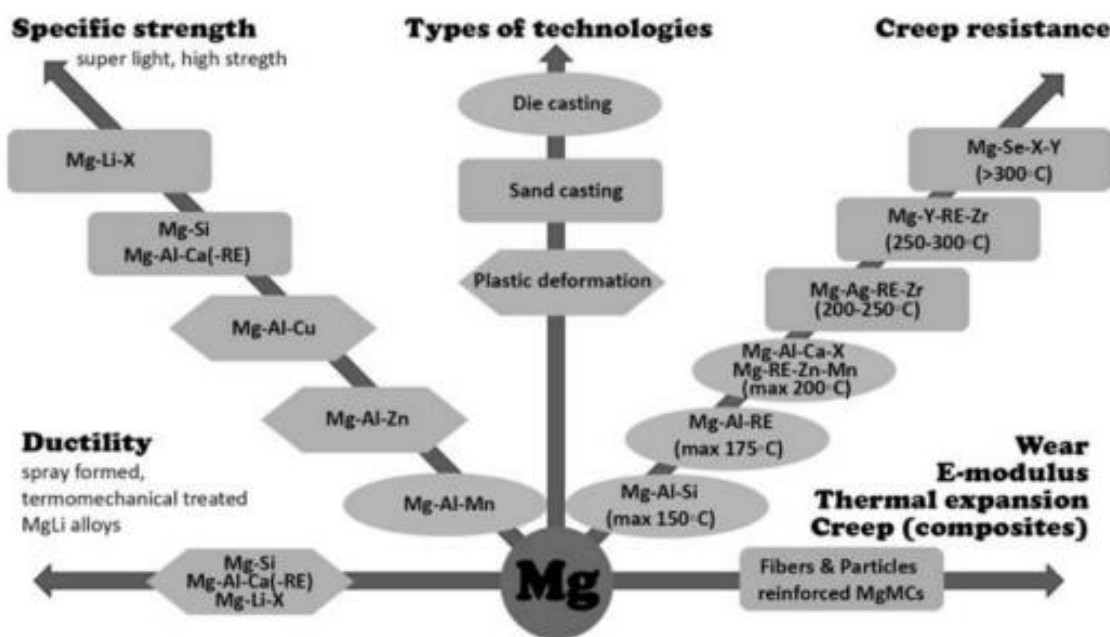


Figure 1.4: Scheme of future directions of Mg-alloys development for industrial applications [3].

1.1.4.1. Automotive industry

One of the broad areas of application of Mg, and mainly its alloys, is the automotive and land transport industry. The use of Mg in automobile part has continued to increase as automobile manufacturers sought to decrease vehicle weight to comply with fuel-efficiency standards. Mg castings have substituted for Al, iron (Fe) and steel in some automobiles. The substitution of Al for steel in automobile sheet was expected to increase consumption of Mg in Al-alloy sheet. Although some Mg sheet applications have been developed for automobiles, these were generally limited to expensive sports cars and luxury vehicles, automobiles where the higher price of Mg is not a deterrent to its use. Some examples of Mg pieces in the automotive industry are shown in **Figure 1.5** [3].

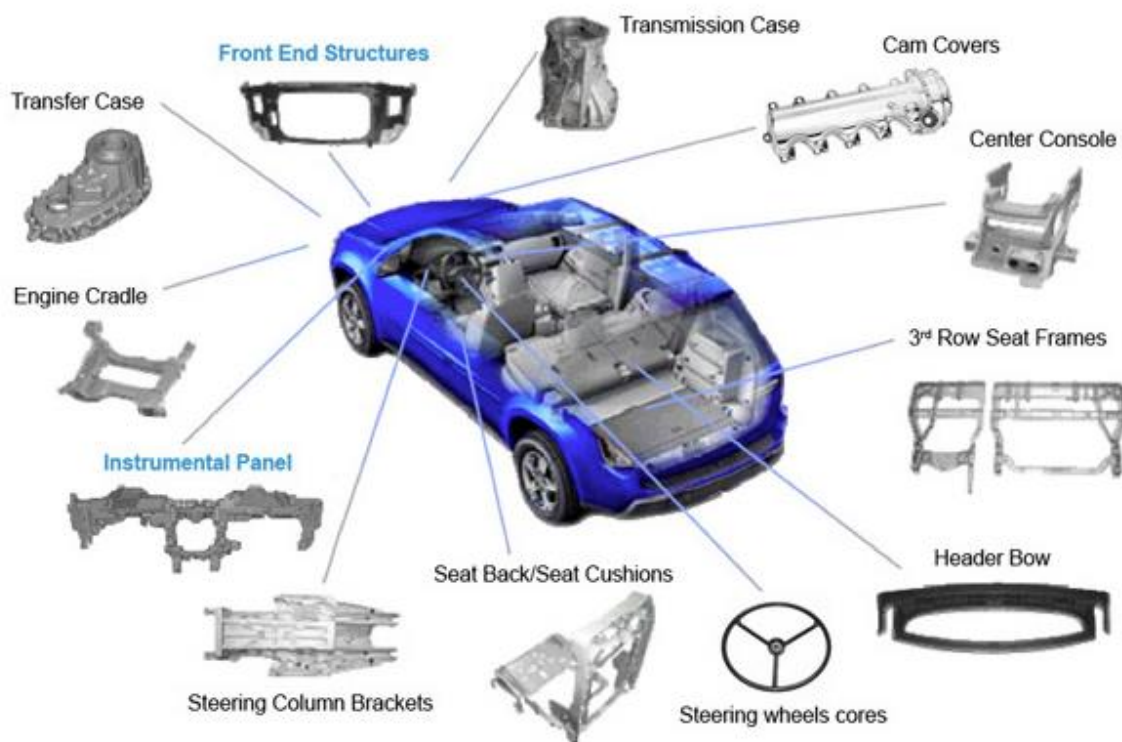


Figure 1.5: Examples of applications of Mg-alloys in automotive industry [19]

1.1.4.2. Aerospace industry

There is quite a long history of Mg usage in the aerospace industry for multiple applications, both civil and military ones. The idea is to reduce the weight of aircrafts and aviation constructions, space and missile vehicles, in order to reduce fume gas emissions and increase fuel efficiency, which has also a major impact on reducing operating costs. Some applications include the thrust reverser (for Boeing 737, 747, 757 and 767), gearbox, engines and helicopter transmission casings, etc. (Figure 1.6). Military aircraft, such as Tornado and F16 also benefit from the lightweight characteristics of Mg-alloys for transmission casings.

There is also widespread use of Mg in spacecraft and missiles due to the requirement for lightweight materials to reduce the lift-off weight. This coupled with its high specific mechanical properties, ease of fabrication, and other attractive features such as [2]:

- Its capacity to withstand elevated temperatures.
- Exposure to ozone.
- Bombardment of high-energy particles and small meteorites.



Figure 1.6: Examples of applications of Mg-alloys in the aerospace industry [19].

1.1.4.3. Medical applications

Mg-alloys were first introduced as orthopaedic biomaterials in the first half of the last century. However, because of its low corrosion resistance, a large amount of hydrogen accumulates around the implant during in-vivo corrosion process, confining the widespread use of Mg-based materials as biomaterials. Despite this, Mg still possesses many attractive characteristics that make Mg-based materials potential candidates to serve as implants for load-bearing applications in the medical industry (Figure 1.7).



Figure 1.7 : Compressive bioabsorbable screw in Mg-alloy for fracture fixation [36].

Mg has a much lighter density than other implant materials (Table 1.5). It also has greater fracture toughness as compared to hydroxyapatite (HA). Furthermore, its elastic modulus and compressive yield strength values are more comparable to that of natural bone than other commonly used metallic

implants. Mg has good biocompatibility and it is biodegradable in human body fluid by corrosion, thus eliminating the need for another operation to remove the implant.

Table 1.5: Summary of the main mechanical properties of bones and implant materials [2].

Materials	Density (g/cm³)	Fracture Toughness (MPa.m^{1/2})	Elastic Modulus (GPa)	Compressive Yield Strength (MPa)
<i>Natural Bone</i>	1.8-2.1	3-6	3-20	130-180
<i>Ti alloy</i>	4.4-4.5	55-115	110-117	758-1117
<i>Co-Cr alloy</i>	8.3-9.2	-	230	450-1000
<i>Stainless steel</i>	7.9-8.1	50-200	189-205	170-310
<i>Magnesium</i>	1.7-2.0	15-40	41-45	65-100
<i>Hydroxyapatite</i>	3.1	0.7	73-117	600

In order to overcome the corrosion issues that limit the use of Mg-based materials in orthopaedics application, in recent years, much research efforts are focused to explore the use of different alloying elements in Mg and surface treatments such as protective coatings on Mg-based materials. The developing composites with the magnesium matrix composites (MgMCs) can also be a solution to the problem [2].

1.1.4.4. Other applications

The excellent specific strength and ability of Mg-alloy and MgMCs to form intricate shapes resulted in many applications in sport related equipment. For example, Mg-based materials are used in the handles of archery bows, tennis rackets and golf clubs. In addition, their lightweight excellent damping characteristics also made them popular in bicycle frames and the chassis of in-line skates. Bicycle frames made from Mg-alloys or composites are capable of absorbing shock and vibration, hence allowing the rider to exert less energy and enjoy a more comfortable ride (**Figure 1.8**).



Figure 1.8: Mg-alloy based bicycle frame [71]

Mg-based materials are also interesting for electronic applications. In fact, the trend in the electronic equipment industry is to make products more personal and portable. Hence, it is important that the components that make up the equipment are lightweight and durable. Then, Mg-alloys meet the necessary requirements as they are as light as plastic, but exhibit great improvement in strength, heat transfer and the ability to shield electromagnetic interference and radio frequency interference, as compared with their plastic counterparts. Therefore, they are used in housings of cell phones, computers and laptops [2].

1.2. Mg-Zn-Y alloys

Rare earth (RE) metals are a set of 17 chemical elements in the periodic table exhibiting similar chemical properties. It is compound of the fifteen lanthanides as well as scandium (Sc) and yttrium (Y) (**Figure 1.9**). As mentioned in **table 1.2**, the alloying of Mg with RE metals allows to produce lightweight materials with an increased strength and creep resistance at high temperatures, thanks to the formation of stable precipitates at high temperature. Furthermore, the addition of RE improve the ductility of Mg-alloys, because of the decrease of stacking-faults energy, SFE [11].

H																				He
Li	Be											B	C	N	O	F	Ne			
Na	Mg											Al	Si	P	S	Cl	Ar			
K	Ca	Sc	Ti	V	Cr	Mn	Fe	Co	Ni	Cu	Zn	Ga	Ge	As	Se	Br	Kr			
Rb	Sr	Y	Zr	Nb	Mo	Tc	Ru	Rh	Pd	Ag	Cd	In	Sn	Sb	Te	I	Xe			
Cs	Ba	La-Lu	Hf	Ta	W	Re	Os	Ir	Pt	Au	Hg	Tl	Pb	Bi	Po	At	Rn			
Fr	Ra	Ac-Lr	Rf	Db	Sg	Bh	Hs	Mt												

lanthanide series	La	Ce	Pr	Nd	Pm	Sm	Eu	Gd	Tb	Dy	Ho	Er	Tm	Yb	Lu
-------------------	----	----	----	----	----	----	----	----	----	----	----	----	----	----	----

actinide series	Ac	Th	Pa	U	Np	Pu	Am	Cm	Bk	Cf	Es	Fm	Md	No	Lr
-----------------	----	----	----	---	----	----	----	----	----	----	----	----	----	----	----

Figure 1.9: RE metals in the periodic table [72]

This last decade, a particular attention has been given to the development and study of the ternary systems Mg-TM-RE with $TM = Zn, Ni$ or Cu . It has been proven that the combination of a transition metal with RE leads to a significant increase in the yield values, in particular for Mg-Zn-Y and Mg-Zn-RE systems. These alloys commonly contain a precipitation phase with a long-period stacking-ordered (LPSO) structure, which has been considered to play essential roles for their attractive mechanical properties.

1.2.1. Mg-Zn-Y system

During the solidification of Mg-Zn-Y alloys, the α -Mg phase solidifies first forming dendrites, in a way that the remaining liquid becomes richer in Zn and Y elements. Depending on the concentration of these elements, different phases can be observed in the interdendritic space such as:

- The icosahedral quasicrystal phase I (Mg_3YZn_6).
- The W phase ($Mg_3Y_2Zn_3$) with a face-centered cubic crystal structure.
- Laves phase ($MgZn_2$) with a hexagonal lattice.
- Intermetallic phases Mg_xY ($x = 3, 5, \text{ or } 7$).
- Long-period stacking-ordered phases.

Figure 1.10 shows the phase diagram at room temperature of the Mg-Zn-Y system with the coexistence of the several phases possible. Table 1.6 summarizes the composition and the crystalline structure of each phases. The ratio Zn/Y present in the alloy composition governs the presence and the coexistence of these phases [11].

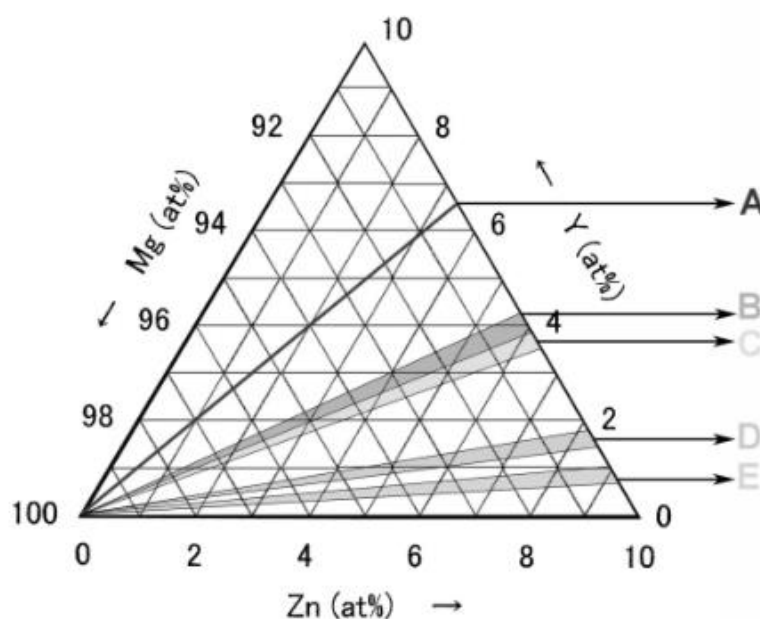


Figure 1.10: Phase diagram of coexistence at room temperature of the different phases of the Mg-Zn-Y system, in the Mg-rich region [11].

Table 1.6: Coexistence of phases in the Mg-Zn-Y system depending of the ratio Zn/Y [11].

Mg-Zn-Y systems	Zn/Y ratio	Phases
A	0.5	$\alpha - \text{Mg} + \text{LPSO}$
B	1.5-2	$\alpha - \text{Mg} + \text{W} (\text{Mg}_3\text{Y}_2\text{Zn}_3, \text{FCC})$
C	2-2.5	$\alpha - \text{Mg} + \text{I} (\text{Mg}_3\text{YZn}_6, \text{Icosahedral}) + \text{W}$
D	5-7	$\alpha - \text{Mg} + \text{I}$
E	10	$\alpha - \text{Mg} + \text{Mg}_7\text{Zn}_3$ (Orthorombic)

Even though this work will investigate the effect of the LPSO phases in more details, the other phases also present an interest in the strengthening of Mg-alloys. I-phase, with an icosahedral quasicrystal structure, has high hardness and can greatly improve the mechanical properties of the Mg-alloys by promoting dynamic crystallization and providing particle strengthening. The yield strength of the Mg-Zn-Y alloys was reported to be 125-400 MPa depending on the amount and size of the I-phase and

aging treatment. On the other hand, W-phase, with a face-centered cubic (fcc) crystal structure, forms an incoherent interface with the Mg matrix and thus atomic bonding between W-phase and the Mg matrix is weak. W-phase may not be as effective as I-phase for a strengthening phase, but W-containing extruded Mg-Zn-Y alloy could exhibit the high yield strength of 350 MPa when W-phase was effectively broken and well dispersed in the matrix. In addition, it has been reported that I-phase is more effective in strain hardening than LPSO- and W-phases and is considerably more resistant to interfacial debonding than W-phase, leading to production of a much higher tensile ductility [20].

1.2.2. Stacking and chemical order of LPSO structures

LPSO structures are an isotope of the hexagonal close-packed (hcp) crystallographic structure of Mg crystals and exhibit rhombohedral (R) and hexagonal (H) Bravais lattice, depending on the stacking period of the closed-packed atomic layers. The hcp structure is constructed by stacking the close-packed layers with a two-layer periodicity (**Figure 1.12a**), and its long-period stacking derivatives are generated by introducing the stacking faults (SFs) periodically into the original hcp crystal. Generally, LPSO structures in Mg-alloys mainly exist in the form of a three-dimensional quasi-continuous honeycomb-like network at grain boundaries, as shown in **Figure 1.11**.

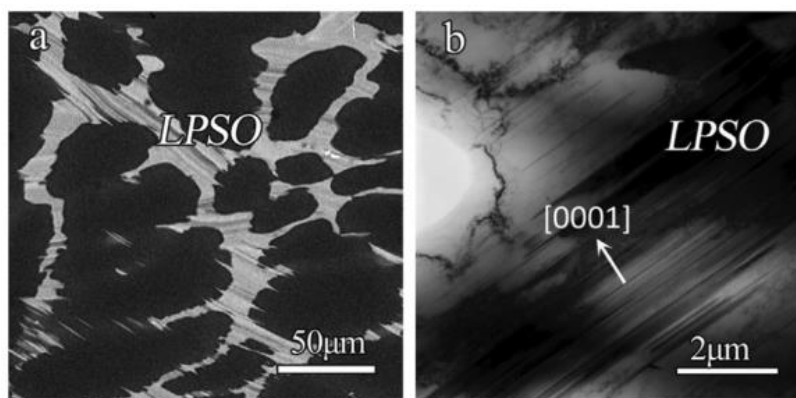


Figure 1.11: (a) Scanning Electron Microscopy (SEM) micrograph and (b) low magnification Transmission Electron Microscopy (TEM) micrograph exhibiting salient structure of the LPSO phase of Mg-Zn1-Y2 (at.%) alloy [7].

According to their different stacking sequences, so far, four types of LPSO structures including 10H, 18R, 14H and 24R have been reported in Mg-M-RE systems ($M = \text{Al, Ni, Cu, Zn}$; $\text{Re} = \text{Y, Gd, Dy, Ho, Er, Tb}$ and Tm). These structures contain an $\text{AB}'\text{C}'\text{A}$ -type building block ($\text{AB}'\text{C}'\text{A}/\text{CA}'\text{B}'\text{C}/\text{BC}'\text{A}'\text{B}$) along the c -axis, as shown in **Figure 1.13**. Here, C represents the SF with respect to the original AB stacking in hcp structure of Mg, and the layers denoted by a prime are enriched with M/RE elements (bright contrast on **Figures 1.12b** to **12e**). In addition, there are 1-4 layers of Mg sandwiched in between $\text{AB}'\text{C}'\text{A}$ -type building block. Three other types of LPSO structures have been reported in as-cast Mg-Co-Y alloy: 15R, 12H and 21R. The stacking sequence of these LPSO structures includes an $\text{AB}'\text{C}$ -type building block with 2-4 layers of Mg in between [7].

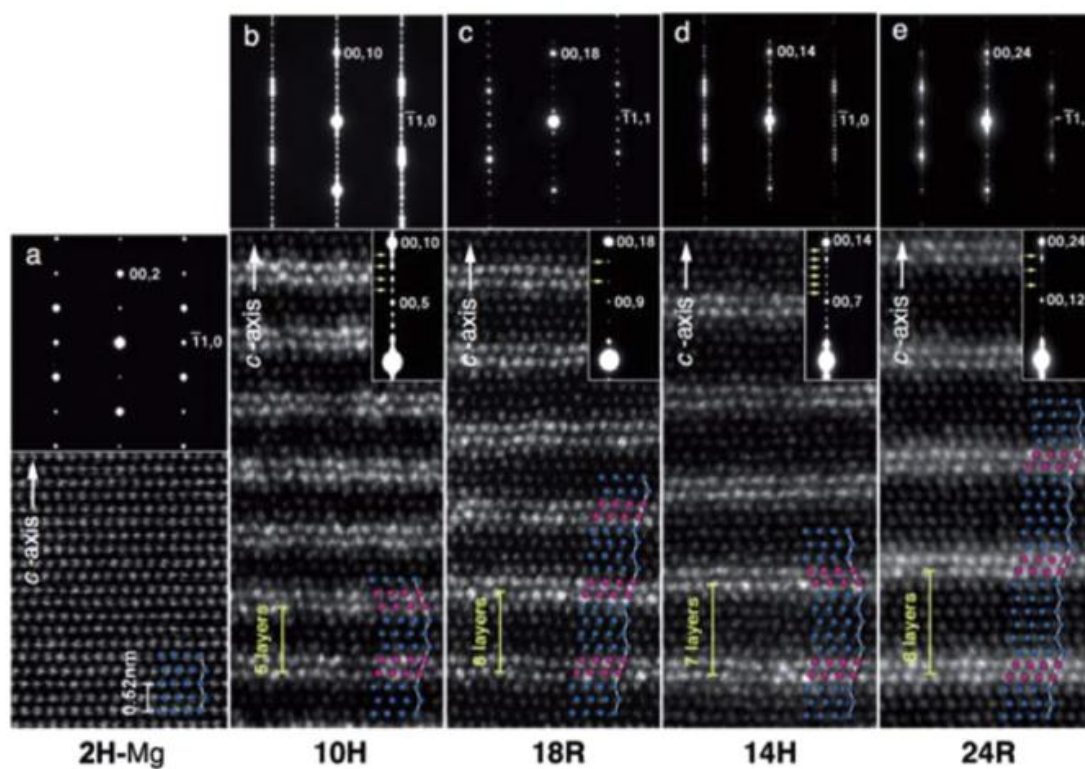


Figure 1.12: Selected area electron diffraction (SAED) patterns and Z-contrast Scanning-TEM (STEM) images of (a) hcp-Mg and LPSO structures of (b) 10H (c) 18R (d) 14H (e) 24R in MgZn₁Y₂ alloy [9].

The model structures of the 10H, 18R, 14H and 24R with their cyclic stacking represented by A-B-C sequences are shown in **Figure 1.13**.

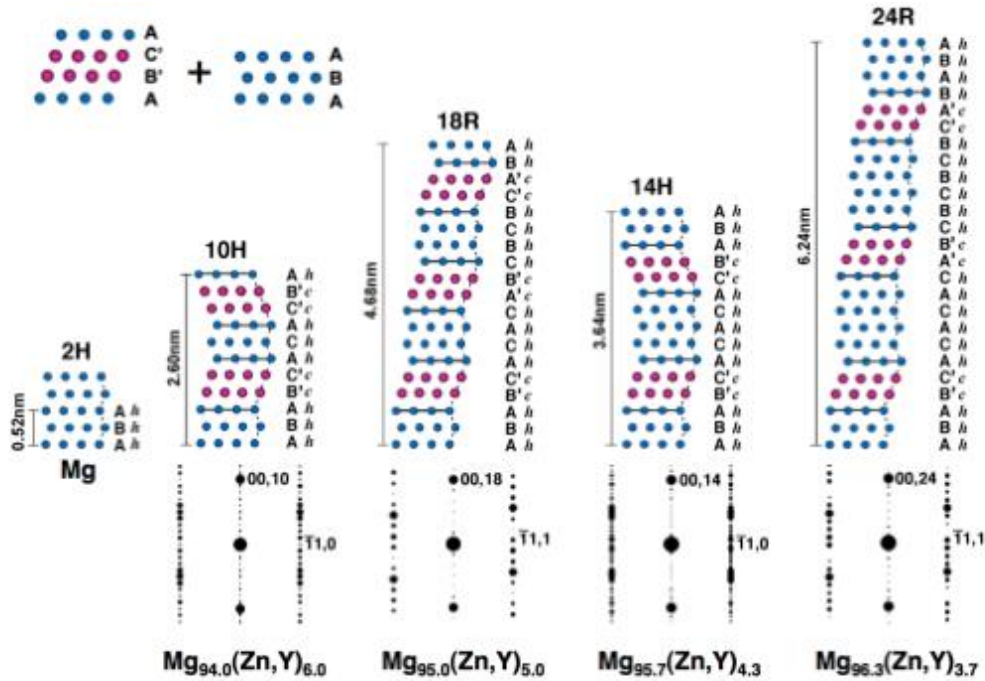


Figure 1.13: Structure models of the Mg-Zn-Y LPSO polytype structures. Blue and red circles denote the Mg occupation sites and the Zn/Y occupation sites, respectively [9].

The stacking sequences presented in Figures 1.12 and 1.13 are summarized in Table 1.7.

Table 1.7: Stacking sequences of various LPSO phases [7].

LPSO Structure	Stacking Sequence along c-axis
10H	AB'C'ACAC'B'AB
18R	AB'C'ACACA'B'CBCBC'A'BAB
14H	AB'C'ACACAC'B'ABAB
24R	AB'C'ACACACA'B'CBCBCBC'A'BABAB
15R	AB'CBC BC'ACA CA'BAB
12H	AB'CBCBCB'ABAB
21R	AB'CBCBC BC'ACACA CA'BABAB

Besides the stacking and chemical ordering of the LPSO phase along the basal plane, the in-plane ordering of solute elements has attracted increasing attentions. The features of in-plane ordering or disordering of M-RE clusters are crucial for understanding the stability and formation of LPSO structures in Mg-based ternary alloys because they can influence and even determine the allowable range of composition and stoichiometry for the formed LPSO phases. M and RE elements were further found to be ordered within the AB'C'A-type building block forming $L1_2$ -type short-range order clusters that are arranged according to an ideal superlattice dimension of $6x(1\bar{2}10)_{hcp}$ with respect to the fundamental hcp Mg lattice. A recent study proved that Highly-ordered Mg-Zn-Y LPSO phases with the 18R-, 14H- and 10H-type stacking sequences possess the in-plane long-range ordering of the Zn_6Y_8 (Figure 1.14) atomic clusters in their structural blocks [6].

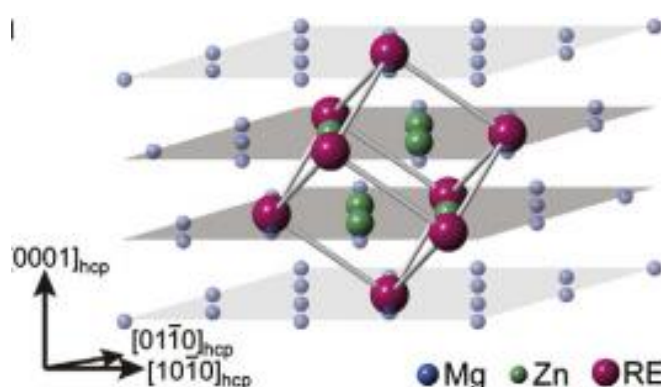


Figure 1.14: Model of Zn_6Y_8 cluster [21].

1.2.3. Formation of LPSO structure

There exist criteria for RE that could participate in the formation of LPSO phases in Mg-Zn-RE (Y, La, Ce, Pr, Sm, Nd, Gd, Dy, Ho, Er, Tb, Tm and Yb) systems. The criteria mainly include the following aspects:

- *Negative mixing enthalpy for Mg-RE and Zn-RE pairs.*
- *HCP structure at room temperature.*
- *Large solid solubility limits above approximately 3.75 at. % in Mg.*
- *Larger atomic size than Mg by 8.4-11.9% [22].*

After observation of LPSO phases in Mg-Co-Y alloy, the above criteria were specified in Mg-TM-RE ternary systems. The mixing enthalpy between Mg-TM, Mg-RE should be - 4 to 3 kJ/mol and - 38 to - 22 kJ/mol, respectively. Additionally, the atomic diameter of TM should be 0.124-0.143 nm.

Table 1.8 summarizes the atomic radius, the mixing enthalpy between Mg-TM and the LPSO phases observed in several Mg-TM-RE systems. It is noticeable that the mixing enthalpies between Mg-TM are negatives except for the system Mg-Co-Y. Generally, the 10H-, 14H-, 18R- and 24R-LPSO phases in Mg-

TM-RE (TM = Ni, Cu, Al and Zn) alloys contain an ABCA-type of building block, while the 15R-, 12H- and 21R-LPSO phases in Mg-Co-Y alloys include an ABC-type building block. This can be attributed to the mixing enthalpy [7].

Table 1.8: Characteristics of metal elements and LPSO polytypes in Mg-TM-RE alloys [7].

Mg-TM-RE	Atomic radius of TM (nm)	Mixing between (kJ/mol)	enthalpy Mg-TM	LPSO phases
<i>Mg-Zn-Y</i>	0.139	-4		10H, 14H, 18R, 24R
<i>Mg-Cu-Y</i>	0.128	-3		18R
<i>Mg-Ni-Y</i>	0.124	-4		18R, 14H, 10H
<i>Mg-Al-Gd</i>	0.139	-2		18R, 14H
<i>Mg-Co-Y</i>	0.126	3		15R, 12H, 21R, 18R

Generally, 18R-LPSO phase forms at the grain boundaries as a secondary phase during solidification, whereas 14H-LPSO phase precipitates during heat treatment at elevated temperatures after casting. For the original formation region of LPSO phases, a formation mechanism of LPSO in a Mg-Cu-Y alloy. It mainly contains two steps:

- 1) *Formation of an amorphous layer along the grain boundary (GB).*
- 2) *The LPSO crystal growth from the boundary up to the inside of the Mg matrix crystal.*

It indicates that the LPSO crystals evolve and grow towards the Mg matrix by consuming the amorphous layer [23]

On the atomic level, LPSO structure is referred to the introduction of a new long-period ordered lattice in the original crystal lattice period. It mainly includes two steps:

- *Introduce the SFs periodically on close-packed planes of the hcp Mg crystal.*
- *The segregation of solute atoms of Zn and Y around these SF layers.*

The former is a stacking ordered process, which requires a propagation of Shockley partial dislocations, and the segregation of solute atoms of Zn and Y around these faults induced by the local strain field around the dislocation [24].

Recently, *Mao et al.* [17] proposed in a study a model for the formation and growth of a unit LPSO phase in as-cast Mg-4.5Zn-6Y alloy. They deduced that Zn/Y elements segregated first into two adjacent closely packed layers, and then only later SFs form in response to the strain field generated by solute segregation (**Figure 1.15**). The growth of a unit LPSO building structure is accommodated by expansion of SFs. Once the SFs form, they foster further segregation of Zn/Y atoms into the faulted layers.

The growth of both 18R and 14H within the α -Mg matrix occurs via ledge mechanism, with the thickness of the particle increasing by the height of the ledge as it propagates [73].

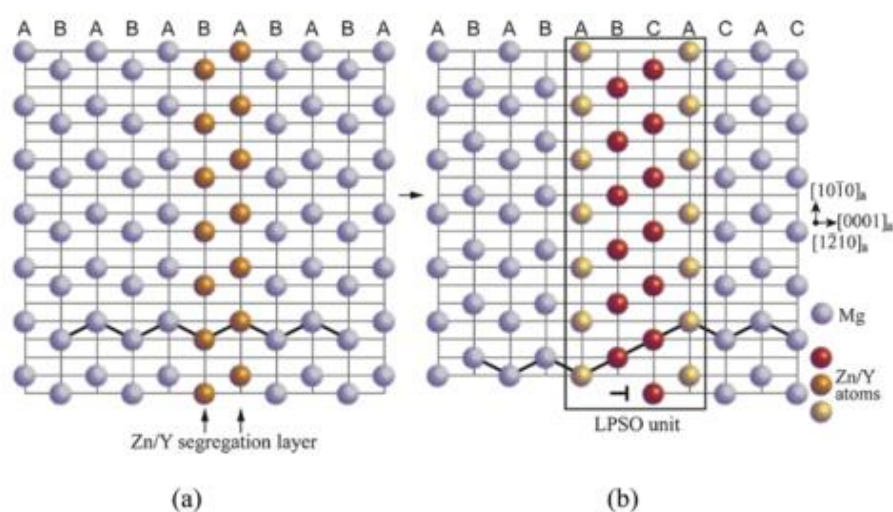


Figure 1.15: Schematic model showing formation and growth model of a unit LPSO phase (a) Segregation of Zn/Y; (b) SF formation [17].

Several observations demonstrate that the coexistence and transformation of LPSO structures may take place in numerous Mg-M-RE alloys. It has been found that four types of 18R-, 14H-, 10H- and 24R-LPSO structures can coexist in a rapid solidified $Mg_{97}Zn_1Y_2$ alloy followed by annealing at 573K for 3.6ks. These types of LPSO structures can be observed not only in the same specimen but also in the same grain. Additionally, no differences in their morphologies and formation sites can be observed. Usually, the 18R structure can be transformed into 14H structure after heat treatment at a certain temperature. The transformation from 18R to 14H occurs most readily in the regions where the 18R structure is irregular in the building block stacking and the diffusion rate of Y and Zn atoms into the segregation layers controls the phase transformation. Thus, 18R and 14H structures should be able to coexist with each other under some situations.

1.2.4. Mechanical properties

1.2.4.1. Tensile properties

Compared with the other commercial Mg-alloys, LPSO-containing Mg-alloys present better mechanical properties. The yield strength, tensile strength and elongation of a hot extruded LPSO $Mg_{97}Y_2Cu_1$, which has similar mechanical properties as $Mg_{97}Y_2Zn_1$, are shown in **Table 1.9**, as well as of pure Mg, which are lower [25].

Table 1.9: Mechanical properties of LPSO Mg-alloy and Mg [25].

Material	Yield strength, MPa	Tensile strength, MPa	Elongation, %
<i>$Mg_{97}Y_2Cu_1$ at room temperature</i>	297	377	8.1
<i>$Mg_{97}Y_2Cu_1$ at 473K</i>	273	344	16.3
<i>Pure Mg at room temperature</i>	115 - 140	180 - 220	2 - 10

Figures 1.16 and **1.17** show the yield strength, tensile strength and elongation for several Mg-based alloys at room and elevated temperatures (473K). When compared with the commercial Mg-alloys, the strengths of the hot-extruded LPSO $Mg_{97}Y_2Cu_1$ alloy at room temperature are slightly higher, but the alloy can exhibit remarkably higher strengths at elevated temperature, when compared to commercial Mg-alloys.

It has been reported that the mechanical properties of the LPSO $Mg_{97}Zn_1Y_2$ alloy were much improved by powder metallurgy processing such as the consolidation of rapidly solidified powders or chips prepared from cast ingots. The rapidly solidified powder metallurgy as $Mg_{97}Zn_1Y_2$ alloy exhibits a yield strength of 610MPa and an elongation of 5%, and the chip consolidated $Mg_{97}Zn_1Y_2$ alloy has a yield strength of 430MPa and an elongation of 3% [26].

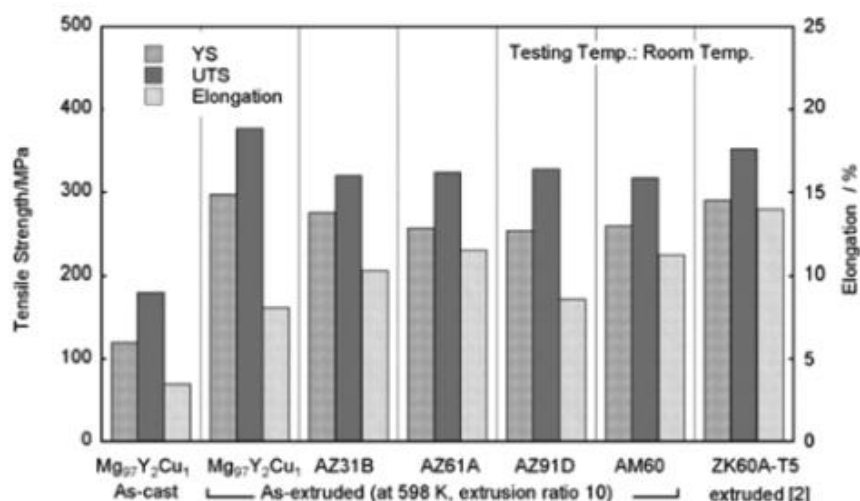


Figure 1.16: Tensile properties of Mg-based alloys at room temperature [25].

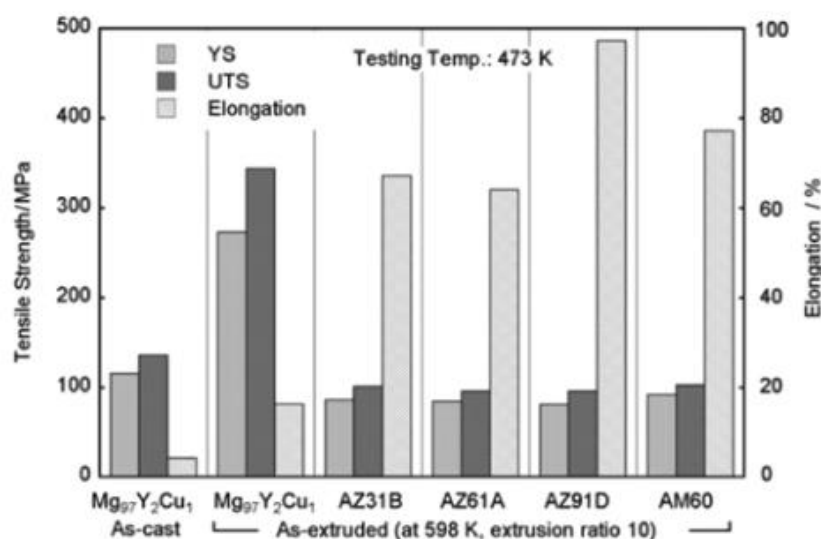


Figure 1.17: Tensile properties of Mg-based alloys at 473K [25].

1.2.4.2. Compressive properties

Besides their good tensile properties, LPSO-containing Mg-alloys present superior compressive properties. **Table 1.10** lists the main compressive properties for pure Mg, several commercial Mg-alloys and as-cast $Mg_{97}Zn_1Y_2$ alloy at 573K and strain rate of $10^{-3}s^{-1}$. It is noticeable that the as-cast $Mg_{97}Zn_1Y_2$ alloy exhibits the highest peak stress of 190MPa compared to the other materials. This can be mainly ascribed to the 3 following factors:

- Deformation kinking in LPSO phases, mechanism that will be described later, plays a key role in strengthening and toughening of Mg-alloys.
- The hardening LPSO phases have coherent interfaces with Mg matrix.
- LPSO phases inhibit the deformation twinning and delay Dynamic Recrystallisation [7].

Table 1.10: Compressive properties of Mg and Mg-alloys [7].

Mg alloy	Peak stress, MPa	Strain rate, 10^{-3}s^{-1}
<i>Pure Mg</i>	30	1.7
<i>Mg-0.035 at% Ce</i>	60	1.7
<i>AZ31</i>	42	1.0
<i>AZ91</i>	79	1.0
<i>ZK60</i>	72	2.8
<i>Mg₉₂Zn₆Y_{1.5}Zr_{0.5}</i>	90	1.0
<i>Mg₉₇Zn₁Y₂</i>	190	1.0

1.2.4.3. Effect of volume fraction of LPSO phase on the mechanical properties

The mechanical properties of three extruded $Mg_{100-3x}Zn_xY_{2x}$ alloys ($x = 0.5, 1$ and 1.5%). It has been found that the volume fraction (vol. %) of LPSO phase increased with the increasing of both Y and Z contents. The hardness variations of the alloys with the vol.% of LPSO phase are listed in **Table 1.11**, showing that the hardness of the alloys increased with the increment of the vol. % of LPSO [27].

Table 1.11: Effect of vol. % of LPSO phase on hardness [27].

Alloy	%LPSO	HV
<i>MgY₃Zn_{1.5}</i>	35	84.7 ± 0.6
<i>MgY₂Zn₁</i>	21	82.5 ± 0.7
<i>MgY₁Zn_{0.5}</i>	9	65.4 ± 0.1

Figure 1.18 shows the evolution of the yield stress (YS) and the ultimate tensile stress (UTS) as a function of the temperature. It can be observed for the three alloys that the YS and UTS gradually decreases when the testing temperature increases until 523K, where the values of YS and UTS decreases sharply. Although the mechanical strengths increase with the volume fraction of LPSO phase

when the test temperature is lower than 723K, the $MgY_1Zn_{0.5}$ alloy with the lowest volume fraction of LPSO phase has higher YS and UTS values than the two other alloys when the temperature is higher than 523K [27].

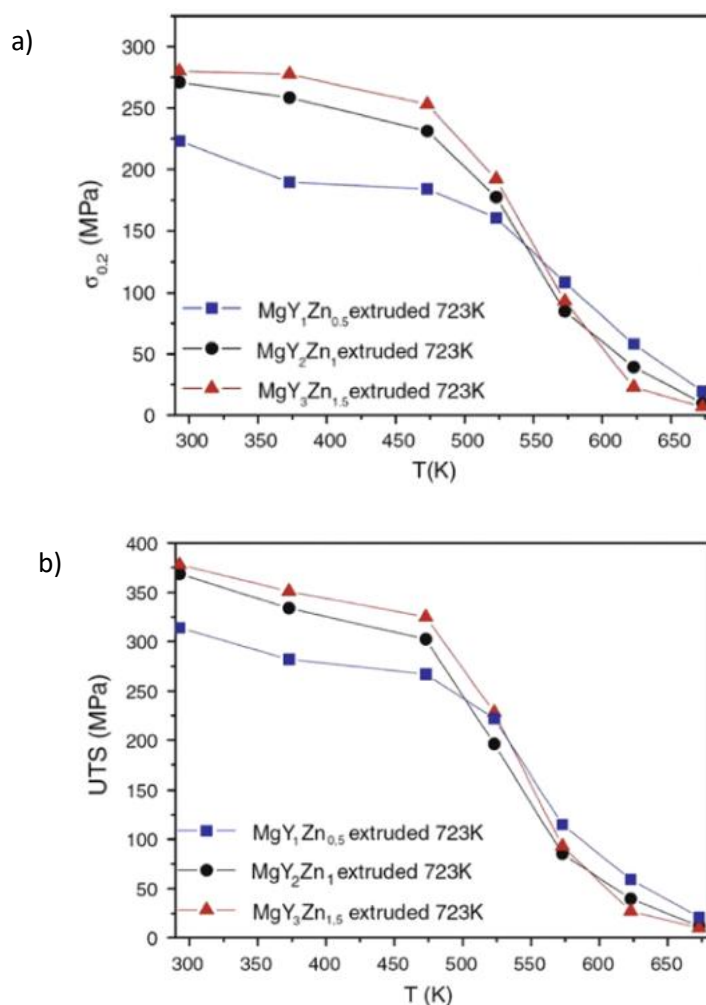


Figure 1.18: Evolution of the (a) YS and (b) UTS function of temperature for 3 LPSO-containing Mg alloys [27].

1.2.4.4. Deformation mechanism

Mg-alloys containing LPSO phases present excellent mechanical properties. Those are attributed to the LPSO phases and their unique deformation behaviours referred to as “*kink deformation*” that causes the LPSO crystals to bend sharply by generating definite interfaces. It is generally known that kink deformation may preferably occur for anisotropic crystals owing to their limited slip systems such as an hcp crystal. Kinking is generally known as a minor deformation mode in crystalline materials, but it appears to be an essential mode for the LPSO crystals, for which both the non-basal slip and twinning are strongly suppressed [8].

Micro-kinking feature were observed in the LPSO structures in a hot extruded $Mg_{97}Zn_1Y_2$ alloy. The kink boundaries were composed of multiple segmented kink-interfaces that were sequentially rotated with small angles in a definite direction. To explain this, schematic illustrations of kink deformation were proposed, as shown in **Figure 1.19**:

- Nucleation of dislocation pairs occurs within a grain interior (**Figure 1.19a**),
- dislocation walls moved apart and form sharp interfaces with a stepwise shape (**Figure 1.19b**) and
- rotational kinking results in the relevant interfaces with a same rotational direction (**Figure 1.19c**).

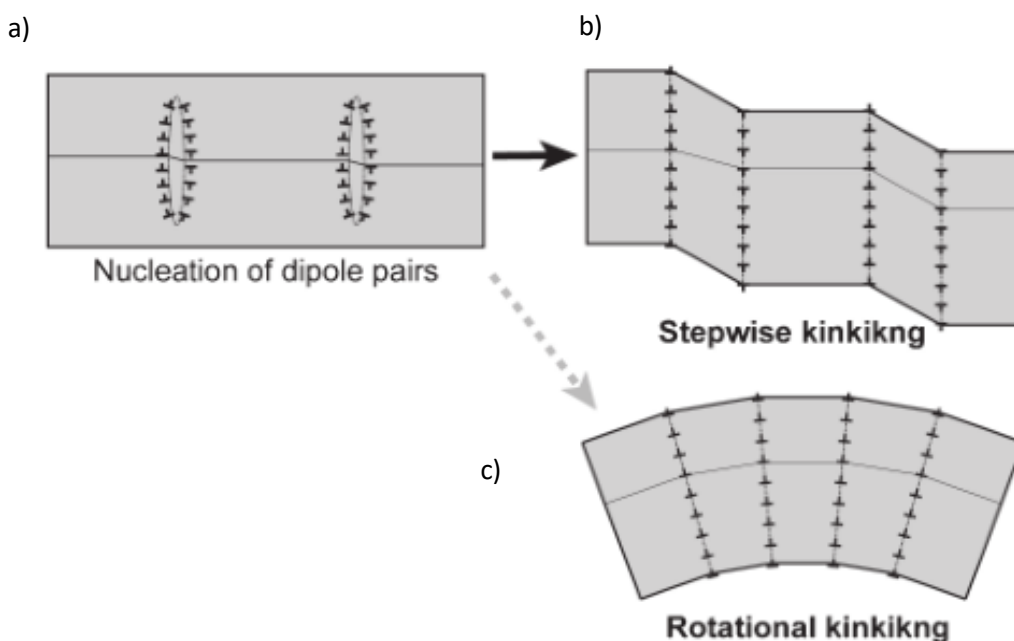


Figure 1.19: Schematic representation of kink deformation [8].

1.2.5. Corrosion behaviour

LPSO containing Mg-alloys exhibit better corrosion resistance compared with the conventional ones, such as AZ31, WE43, ZK60 and ZX60. Comparison of mechanical properties and corrosion behaviour of warm extruded LPSO containing $Mg_{96.83}Zn_1Y_2Zr_{0.17}$ alloy with those of the conventional alloys (AZ31, WE43, ZK60 and EX60) and found that the former displayed a better combination of mechanical strength and corrosion performance [7].

A study of Li *et al.* [16] investigated the effect of volume fraction of LPSO phase on corrosion properties of Mg-Zn-Y alloys. **Table 1.12** regroups the three alloys that were studied as well as their volume fraction of LPSO phase.

Table 1.12: LPSO containing Mg alloys and their volume fraction of LPSO phase [16].

Alloy	Nomenclature	Vol. % of LPSO phase
Mg – Zn _{0.9} Y _{1.6}	ZW12	3.6
Mg – Zn _{2.1} Y _{5.2}	ZW25	20.3
Mg – Zn _{3.1} Y _{7.6}	ZW38	36.2

Figure 1.20 shows the hydrogen evolution and weight loss after 24h results of ZW12, ZW25 and ZW38 alloys immersed in 0.1M NaCl. It shows that both the hydrogen evolution rate and mass loss rate increased in the order of ZW12 < ZW25 < ZW38. Therefore, it indicates that the corrosion rate of all the cast Mg-Zn-Y alloys increased in the same order.

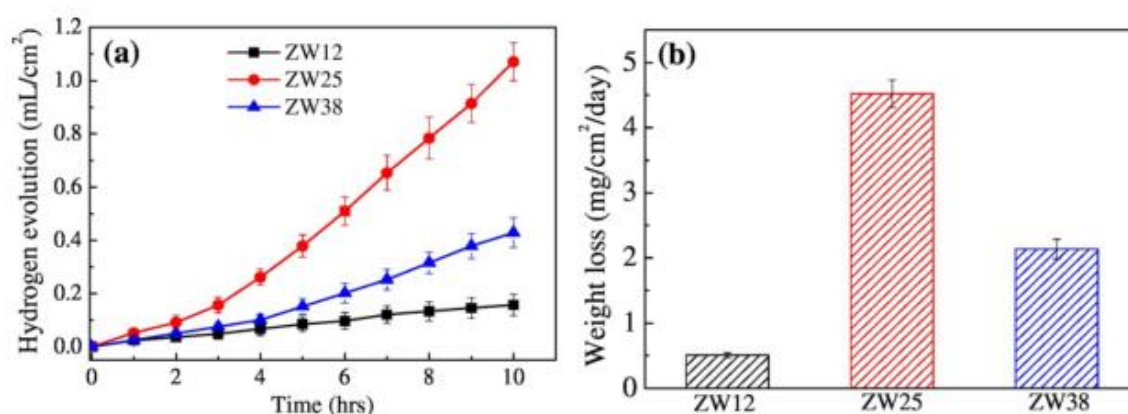


Figure 1.20: Hydrogen evolution and weight loss of the alloys immersed in 0.1M NaCl [16].

The localized potential distribution in Figure 1.21 reveals the electrochemical difference over the surface of ZW38 containing LPSO and Mg matrix. It is noticeable that the Mg matrix have a lower electropotential than the LPSO phase, indicating the presence of micro-galvanic couples (Mg and LPSO as an anode and cathode, respectively). In addition, the difference in potential was up to 250mV at the LPSO/ α -Mg interfaces according to the line-profile results. Such high voltage potential difference implied that severe micro-galvanic corrosion easily occurred at the LPSO/ α -Mg interfaces. It seems evident that the corrosion rate increases when the volume fraction of LPSO phase increases due to the galvanic couple effect, explaining why the corrosion rate of the ZW25 alloy is superior to the ZW12 alloy.

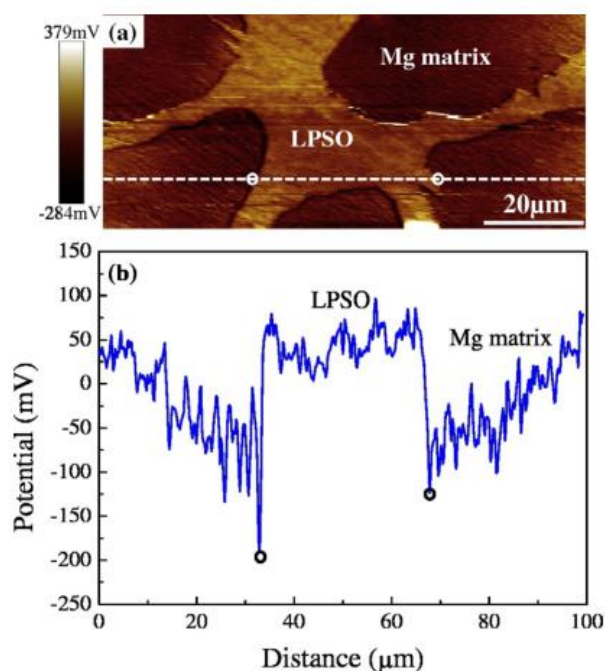


Figure 1.21: (a) Surface voltage potential map obtained by atomic force microscopy (AFM) and (b) line-profile analysis of relative voltage potential trough the LPSO phase in (a) in ZW38 alloy [16].

However, excess containing LPSO phases containing in ZW38 alloy did not result in much worse corrosion resistance than in ZW25, which can be attributed to the hindering effect of more compact and thicker LPSO phases (**Figure 1.22**) on the corrosion attack. It shows that the corrosion behaviour of Mg-Zn-Y alloys depends on not only the volume fraction of LPSO phase, but also on their morphology and throughout the grain. Net-like continuous distribution of LPSO phases is desired to perform better

corrosion resistance and a more uniform corrosion mode than a scattered distribution of LPSO phases throughout the whole grain [16].

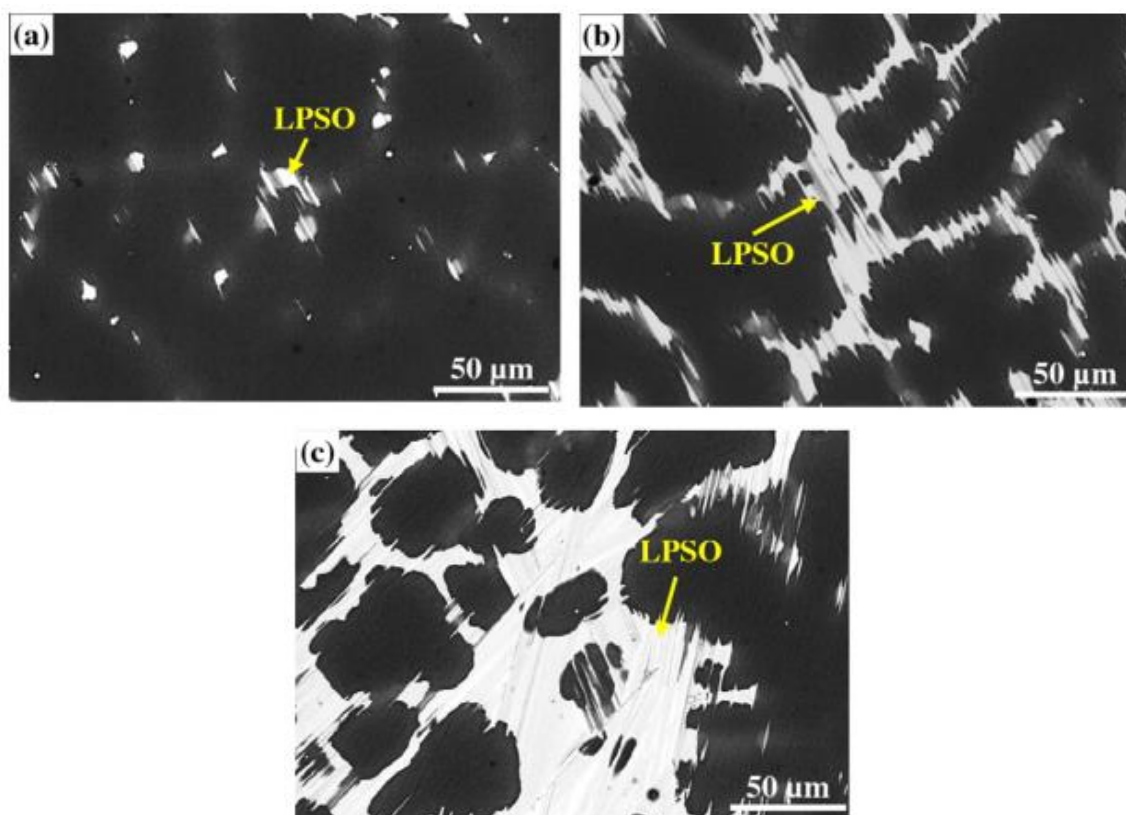


Figure 1.22: SEM micrographs of (a) ZW12, (b) ZW25 and (c) ZW38 [16].

1.2.6. Wear behaviour

Mg-based alloys have been found to display two different types of wear behaviour, namely mild wear and severe wear. The former is acceptable in engineering applications because of its steady wear state, low wear rate and slight surface damaging, while the latter is opposite. Compared to commercial Mg-alloys, LPSO-containing Mg-alloys exhibits good wear resistance. The variations in coefficient of friction and wear rate with load for both as-cast $Mg_{97}Zn_1Y_2$ and AZ91 are shown in **Figure 1.23**, using a pin-on-disc configuration. The two materials show a similar trend in the coefficient of friction with increasing load: sharply decreases at low load, gradually decreases at medium load and finally decreases to the lowest level at high load; however, $Mg_{97}Zn_1Y_2$ displays a lower coefficient of friction compared with AZ91 in the high load range. On **Figure 1.23**, it is noticeable that there is a great difference in wear rate between AZ91 and $Mg_{97}Zn_1Y_2$. The wear rate of AZ91 alloy increases gradually with increasing load before 100N, then goes up dramatically except for a sudden decrease at 140N, whereas the wear rate of $Mg_{97}Zn_1Y_2$ alloy increases gradually until 280N and then increases rapidly.

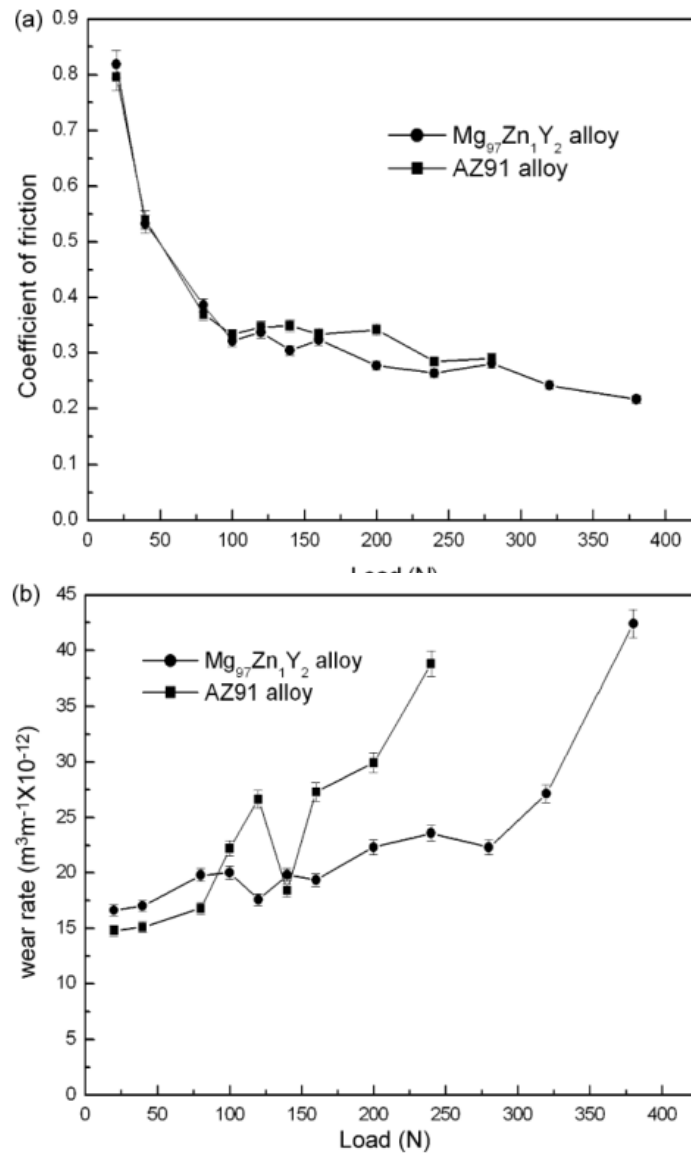


Figure 1.23: Variation in (a) coefficient of friction and (b) wear rate with load [28].

The wear behaviours were found to be abrasion, oxidation, delamination, thermal softening and melting. Under the given conditions, for the Mg₉₇Zn₁Y₂ alloy the dominant wear mechanisms in the load range of 20–200N are abrasion and delamination. In the load range of 240–280N, thermal softening is an important wear mechanism. Surface melting is the wear mechanism as the load is over 280N. The wear behaviour of the two testing magnesium alloys was controlled by change in microstructure and mechanical properties with surface temperature rise during dry sliding.

When contacting solids slide, work is done against friction. Almost all the frictional work appears as heat, generated at the surface at which the 2 solids meet. The local increase in temperature influences

both the friction and the rate of wear. The average surface temperature T_b in sliding contact can be expressed as:

$$T_b = T_0 + \frac{\alpha \mu F v l_b}{A_n K_m} \quad (1)$$

where T_0 is the temperature of the heat sink where the heat flows, μ is the coefficient of friction, F is the normal force on the pin, v is the sliding velocity, A_n is the normal contact area, α is the fraction of the heat diffusing into the pin, l_b is the mean diffusion distance and K_m is the thermal conductivity. α can be calculated from the following equation:

$$\alpha = \frac{1}{2 + \left(\frac{K_m d}{K_{mp}}\right) l_b \left(\frac{\pi v}{8 a r_0}\right)^{0.5}} \quad (2)$$

where α is the thermal diffusivity of steel and r_0 is the radius of the pin. The surface temperature as a function of applied load is shown in **Figure 1.24**. In AZ91 alloy, the main strengthening phase, β , tends to soften and coarsen with an increase in temperature due to its low melting point, while in $Mg_{97}Zn_1Y_2$ alloy, LPSO phases can provide a superior thermal stability with increase of temperature. The good tribological property in $Mg_{97}Zn_1Y_2$ alloy at high load was due to the superior thermal stability of the LPSO phase [28].

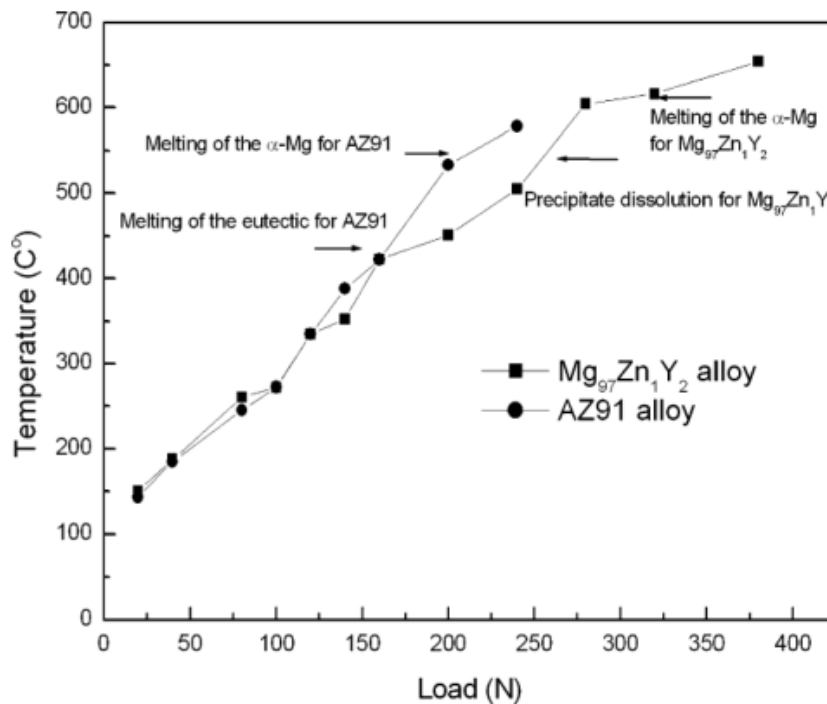


Figure 1.24: Variation in surface temperature with applied load [28].

1.3. Surface modification techniques

Friction and wear are two major concerns in various engineering applications where surface interaction exist. Surface texturing has been perceived as an efficient and widely approach to modify the interaction between surfaces for better lubrication, controlled friction, and enhanced wear resistance. In addition, surface texturing is also used to enhance mechanical properties such as hardness and fatigue resistance. Over the years, many surface texturing techniques have been developed to improve the previously presented properties.

1.3.1. Shot peening

Shot peening (SP) is a mechanical technique which consists in propulsing at high speed (10-100 m/s) spherical particles of diameter from 0.1 to 3mm made from a hard material such as steel, glass or ceramics (**Figure 1.25**). By impacting the surface, the particles induce plastic deformation generating compressive residual stresses in the near surface layer of the material, which results in the increase of the mechanical properties such as the fatigue resistance or hardness by work hardening. The main operational parameters of this process are the nature, the size, the number and the velocity of the peens, the exposure time and the processing temperature [37].

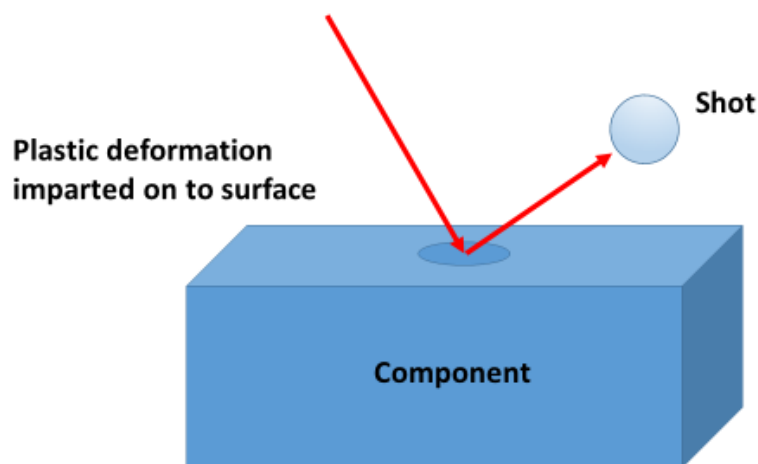


Figure 1.25 : Schematic representation of the shot peening process.

It was found that SP improved fatigue life of Mg-alloy AZ80, the fatigue strength increased from 100 to 160MPa at the optimal condition of a SP intensity of 0.15 mmN, meaning an improvement in the fatigue strength of 60%. **Figure 1.26** shows the evolution of microhardness function of the depth from the surface of shot peened wrought AZ80 alloy for different shot peening intensity. The highest hardness is found for the highest shot peening intensity of 0.4 mmN [38].

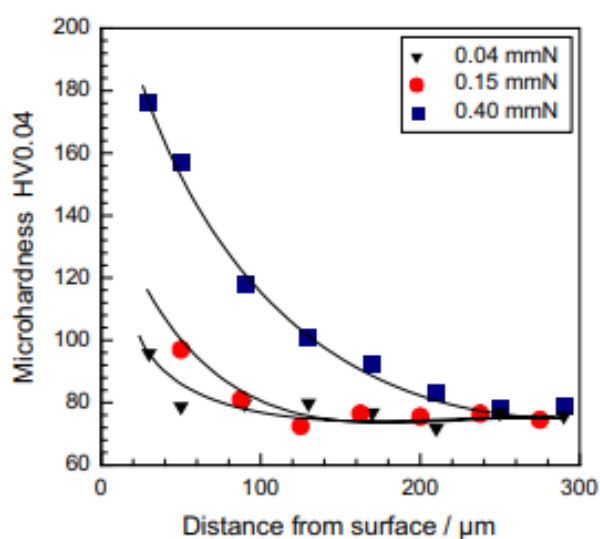


Figure 1.26: Microhardness-depth profile of SP of wrought AZ80 alloy [38].

1.3.2. Sandblasting

Sandblasting, also known as abrasive blasting, is a surface modification technique that consists in propelling a stream of abrasive material against a surface at high pressure to smooth a rough surface, roughen a smooth surface, shape a surface or remove surface contaminants. Alumina (Al_2O_3) is commonly used as abrasive due to its high hardness and low cost. **Figure 1.27** shows a typical sandblasting scheme. The direct consequence of sandblasting is the erosion of the surface which produces micro-roughness. In addition, as SP, the impact of the abrasive particle with the material creates severe plastic deformation which induces compressive residual stresses. The process of erosion involves an energy transfer between the particles and target. The kinetic energy stored by the particles is partially or totally converted into strain energy in the sandblasted material. The kinetic energy is represented in **equation 3** where V , ρ and r are the velocity, density and particle radius, respectively [40]. The repeated impacts lead to the growth of cracks and eventually the coalescence of these cracks results in the removal of the material [39].

$$Ec = \rho \cdot \left(\frac{2}{3}\right) \cdot \pi \cdot r^3 \cdot V^2 \quad (3)$$

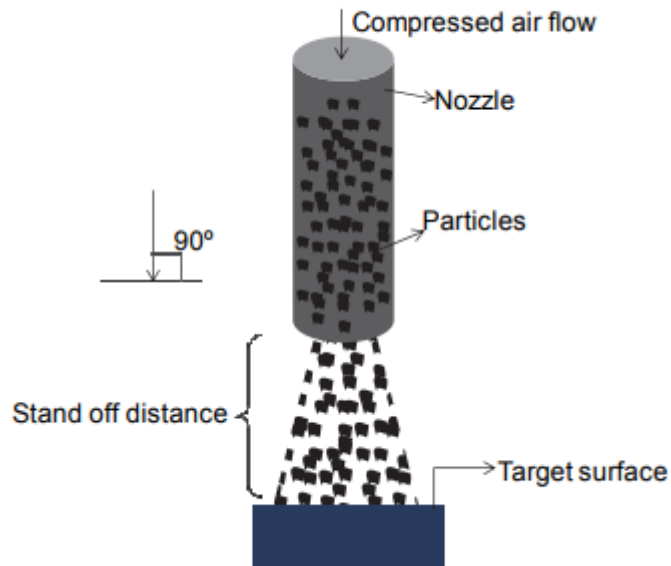


Figure 1.27: Schematic representation of sandblasting process [39].

The main parameters that influence the erosion on the target material are:

- The impact angle: depending if the material is ductile or brittle, the erosion rate will depend on the impact angle with the target material. Based on **Figure 1.28** it is clear that the erosion rate is maximum for low impact angle between 15 and 20° for ductile materials, whereas the erosion rate is maximum for an impact angle of 90° for brittle materials.
- The particle velocity: a higher velocity means a higher kinetic energy of the particle, resulting in a higher erosion rate.
- The particle size: an increase in size induces an increase of particle mass which results in an increase of kinetic energy and so an increase of erosion rate [39].

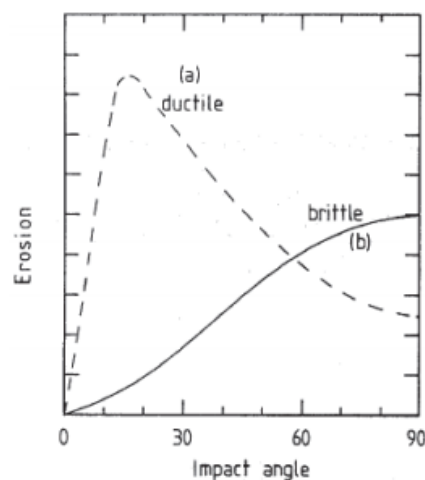


Figure 1.28: Effect of impact angle on erosion rate in ductile and brittle materials [39].

Figure 1.29 shows the high cycle fatigue performance of titanium before and after sandblasting. The runout strength of untreated titanium is about 270MPa, while for the sandblasted samples it is about 300 MPa. The sandblasting treatment enhanced the fatigue strength of titanium of around 11% [41].

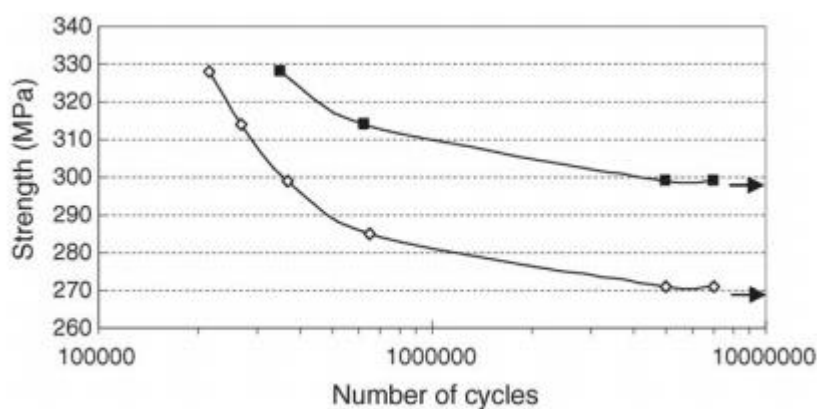


Figure 1.29: Strength-Number of cycles curves of pure titanium before and after sandblasting: white ticks for untreated samples, black ticks for sandblasted samples [41].

1.3.3. Laser surface texturing

Among the several surface modification methods, laser surface texturing (LST) has gained considerable attention due to its advantages such as: fast, high efficiency, good controllability, environmentally friendly nature, and the capacity of fabricating surface texture with high complexity and accuracy. Due to these advantages, this technique has been widely used in various applications to improve the tribological performance of engineering components with contacting surfaces including mechanical seals, thrust bearing, piston rings, and magnetic storage devices. In addition, LST has also been utilized to improve the tribological performance of a variety of material from metals to ceramics and polymers [29].

1.3.3.1. Processes design

There exist different LST techniques based on the mechanisms responsible for surface texture fabrication. The current LST techniques can be divided into three groups, including: (1) *direct material removal by means of laser-induced ablation*, (2) *material melting by laser interference*, and (3) *material shaping and patterning by laser shock induced surface plastic deformation*.

First, **laser ablation** is a process of removing materials from a solid surface by irradiating it with a laser beam. Upon the absorption of laser energy, the laser-matter interaction leads to the evaporation of surface materials, which can be further ionized to form a plasma at a high laser flux. During the laser ablation process, localized material loss is achieved, resulting in a surface texture with specific design patterns, such as micro-dimples or grooves.

Then, **direct laser interference patterning (DLIP)**, serves as another effective LST method. In this technique, the periodic pattern of features is created by means of the interference of coherent laser beams. During the laser beam interfering process, the surface material of the sample is locally melted at position of maximum interference which corresponds to the highest laser intensity. The material transfer from the interference maxima to the minima position due to the surface tension gradient caused by temperature gradient. Using DLIP, several periodic surface geometries, such as line, dot, and cross-like patterns can be fabricated.

Finally, **laser shock processing (LSP)** is an advanced laser-based surface engineering process, in which LSP is utilized to introduce compressive residual stress as well as surface hardening effect on the target surface. A schematic view LSP is shown on **Figure 1.30**. The material is covered with an opaque coating to absorb the laser energy. A transparent confinement is laid on the coating. During the LSP process, laser pulse interacts with the opaque coating instead of the target material, resulting in the formation of laser-induced plasma. The expansion of the plasma is restricted by a transparent confinement, leading to the generation of laser-induced shockwave propagating into the target material. Once the shockwave pressure exceeds the dynamic yield strength of the target material, ultrahigh strain rate plastic deformation occurs on the surface of processed samples. As a result, surface texture with micro-/nano- dimples can be created [29].

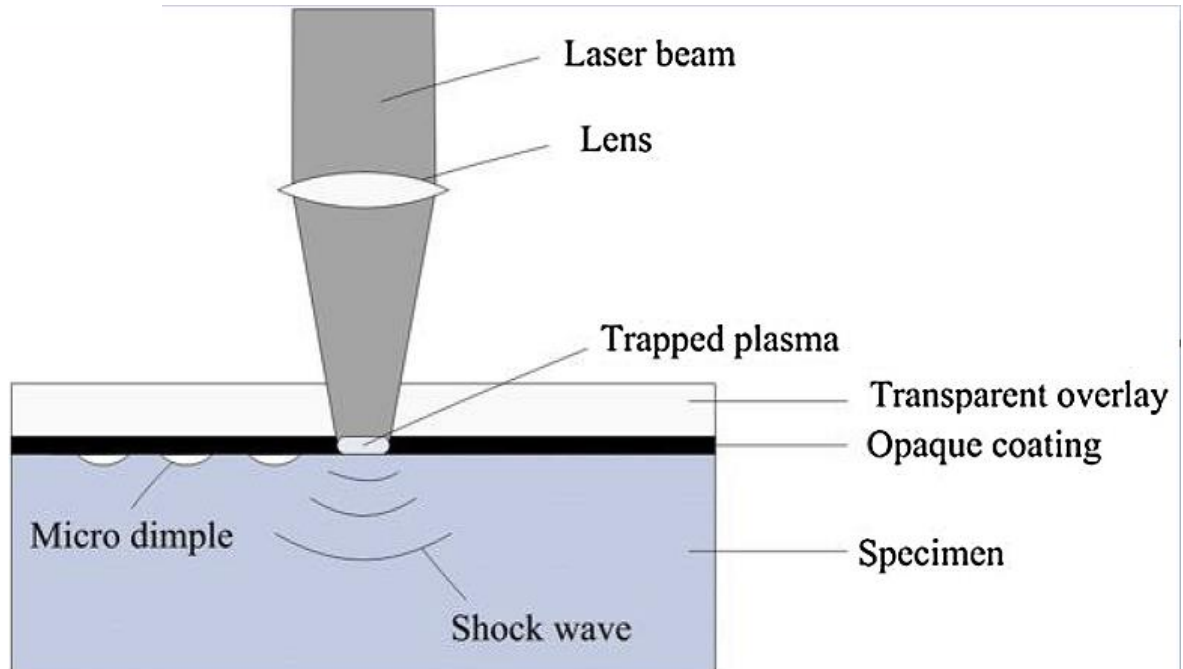


Figure 1.30: Schematic representation of LSP process [29].

A comparison of LST techniques by means of direct laser ablation, laser interference, and LSP is summarized in **table 1.13**.

Table 1.13: Comparison of LST techniques (+ denotes the degree, +++++ meaning very high and + meaning very low) [29].

Criteria	Laser ablation	DLIP	LSP
Flexibility	++++	++++	+++
Efficiency	+++	+++++	+++
Texture feature resolution limit	1 μm for titanium	0.1 μm for silicon substrate	10 μm for Al-alloy
Surface hardening effect mechanism	Heat induced phase transformation (only for some specific metals)	Heat induced phase transformation (only for some specific metals)	Surface plastic deformation for all metallic materials
Applicable materials	Metals, polymers, ceramics and composites	Metals, polymers, ceramics and composites	Metals

1.3.3.2. Effects of laser parameters on surface texturing

In the LST processes, the surface morphology and features sizes can be controlled by adjusting the laser type and the laser processing parameters, such as laser power intensity, laser spot size and number of pulses.

In the LST processes, the laser pulse duration plays a significant role in determining the process efficiency and effectiveness by affecting the thermal input in laser ablation and interference and the plastic deformation rate in LSP. The commercial pulse lasers can be distinguished by the laser pulse duration as milli-second, nano-second (ns), pico-second (ps) and femto-second (fs). The textured surfaces processed by millisecond (0.5 ms), nanosecond (40 ns) and femtosecond (120 fs) lasers on a cast iron are shown in **Figure 1.31**. The surface processed by ms laser was partially melted and the molten materials were ejected from the dimple to the high energy and long pulse duration. The ejected materials deposited around the dimple and formed a kind of bulge. On the other hand, the sample processed by fs laser showed the smoothest surface with the sharpest dimple profile as compared to those processed by ms and ns [30].

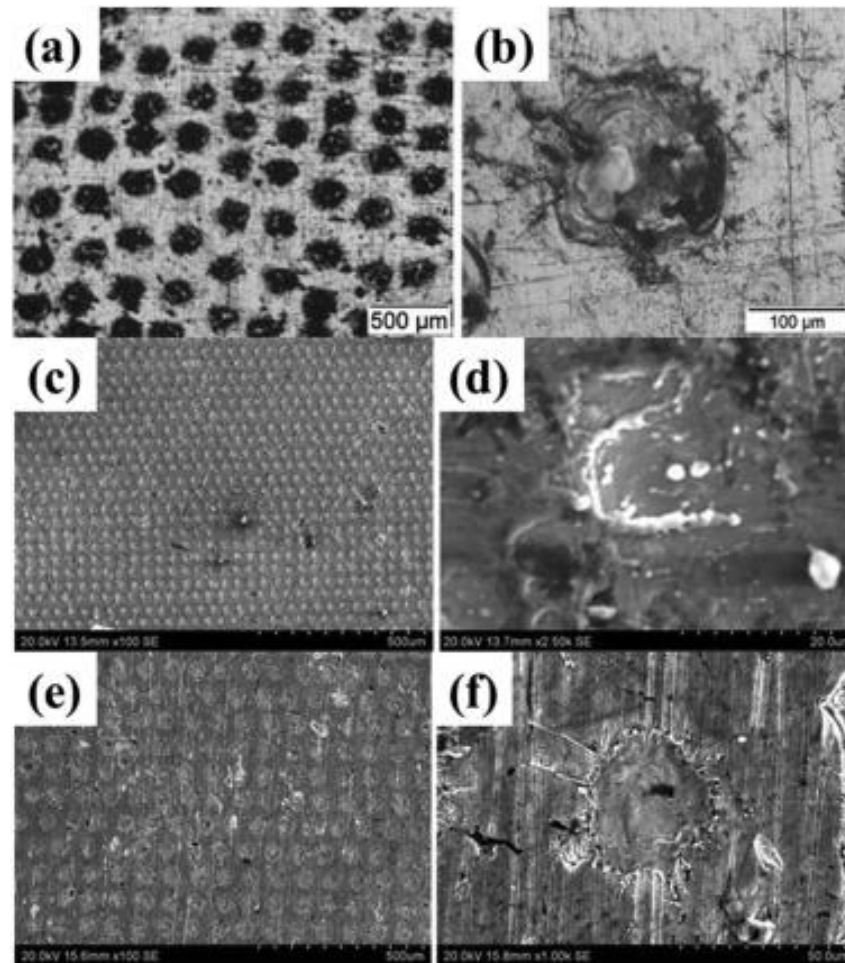


Figure 1.31: Effect of laser type on the surface morphologies of gray cast iron as processed by ablation-based LST: (a) ms laser, (c) ns laser, (e) fs laser; (b), (d), (f) correspond to the enlarged area of individual dimple in (a), (c) and (e) respectively [30].

Compared to millisecond, nanosecond and picosecond lasers, femtosecond laser holds the capacity of fabricating higher quality surface features due to the reduced heat affected zone.

Another important parameter is the laser power intensity. For ablation-based and interference-based LST processes, laser power intensity affects the amount of delivered laser energy, which determines the width, depth and shape of texture features as well as the area of heat affected zone. **Figure 1.32** shows the evolution of the ablation depth with the laser power density for three metallic alloys. It is noticeable that the ablation depth increases linearly with the laser power density for the three alloys [32].

Finally, the number of pulses plays an important role on determining the size, depth, and shape of the surface features. The effect of number of pulses on the morphology of the micro-dimples fabricated on 100Cr6 steel by laser processing was investigated. The results in **Figure 1.33** showed that the depth and height of the crater fabricated by laser ablation were strongly affected by the number of laser

pulses. Larger number of pulses resulted in deeper pore, with pore diameter being more or less independent on the number of pulses [31].

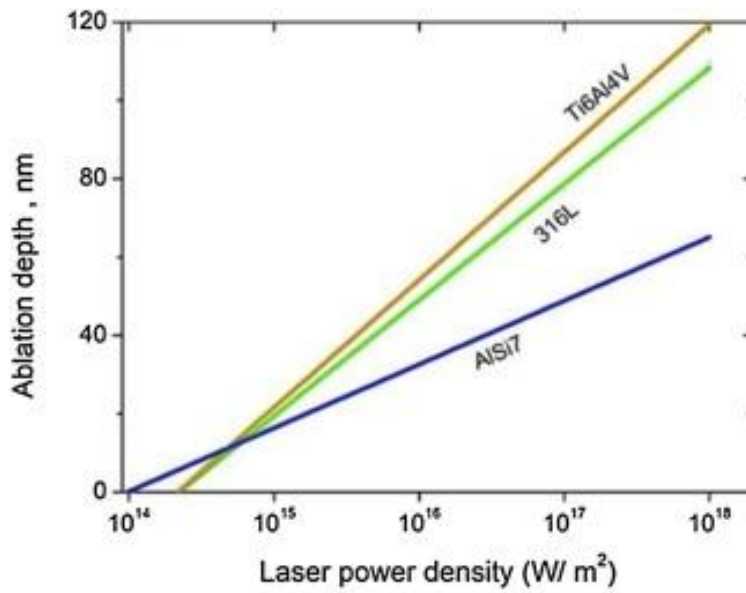


Figure 1.32: Variation of ablation depth with laser power density for AISI7, 316L steel and Ti₆Al₄V [32].

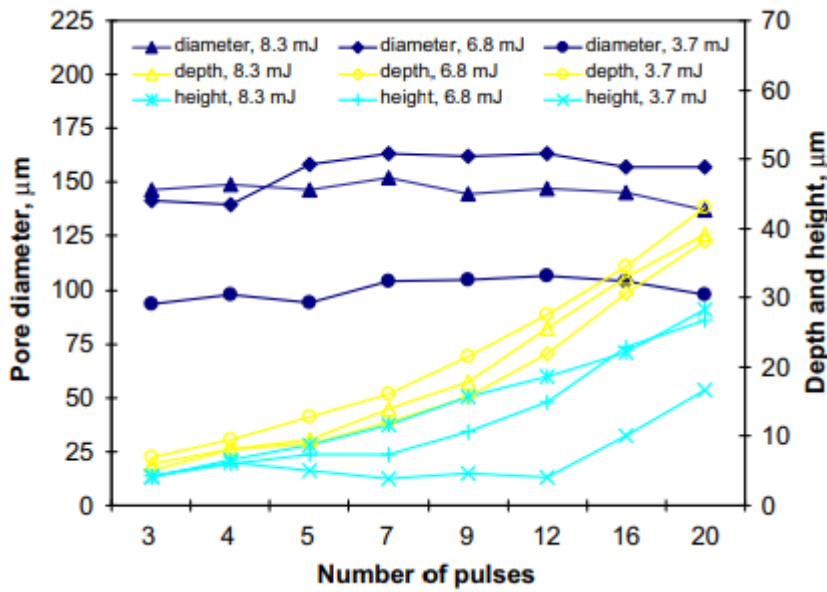


Figure 1.33: Progress of the pore inner-diameter, ablated area's depth and height of micro-pores as a function of the number of laser pulses for different pulses energy (3.7, 6.8 and 8.3 mJ) [31].

1.3.3.3. Tribological effects of laser surface texturing

One application of LST on materials is to affect their tribological properties, in particular the coefficient of friction (COF) in dry and lubricated conditions as well as the wear resistance in dry and lubricated

conditions. The COF of untextured and textured with ordered arrays of circular dimples 30NiCrMo12 were measured in dry “contact” and “single drop” of commercial lubricant configuration. In “dry contact” configuration, for a normal load of 1N, friction coefficient is reduced of about 10% from untextured to textured surface (**Figure 1.34**). In addition, SEM micrographs (**Figure 1.35**) show that debris are observed in contact region between pin and disc. In the case of textured surface, they fill the dimples and this process contributes to the improved tribological performance of these surfaces, whereas in the case of untextured surface, debris at the interface between the two contact surfaces increase friction coefficient and accelerate wear [33].

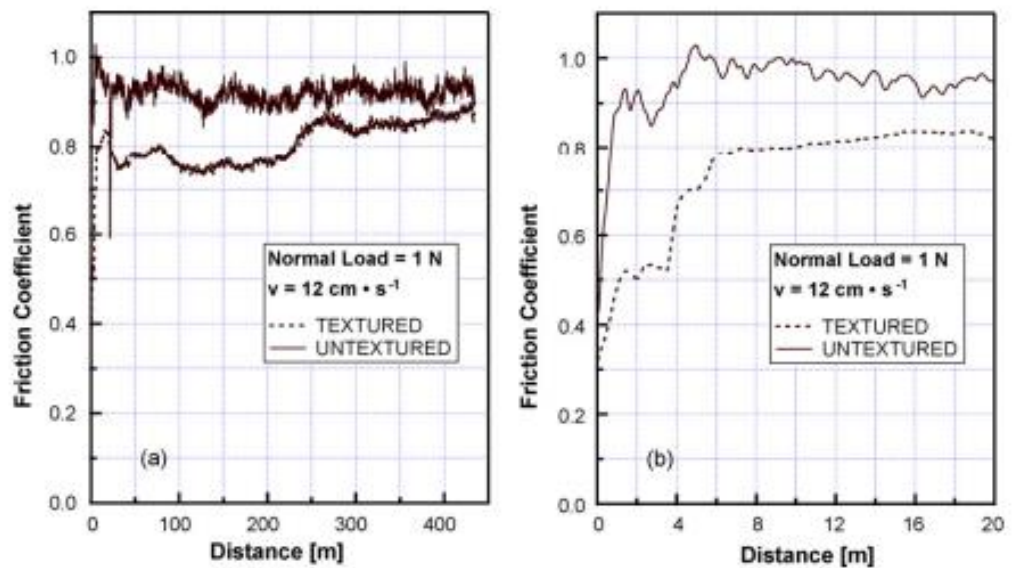


Figure 1.34: (a) COF vs. sliding distance of untextured and textured surfaces obtained in “dry contact” configuration and (b) enlarged detail [33].

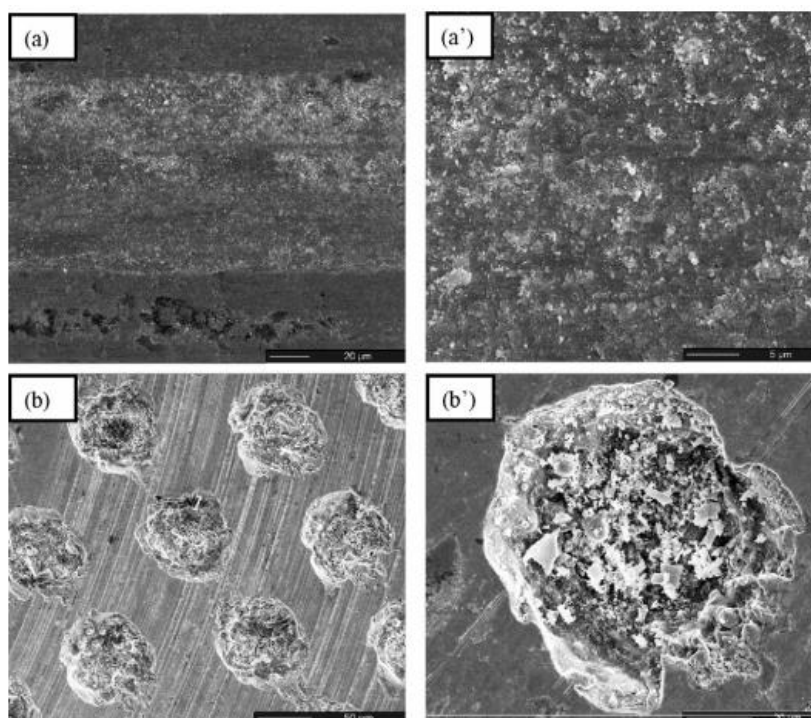


Figure 1.35: SEM micrographs of untextured (a, and its enlarged detail a') and textured (b, and an enlarged dimple b') surfaces after pin-on-disc tests performed in "dry contact" configuration [33].

On the other hand, in "single drop" configuration, for a normal load superior to 3N, the COF is reduced of about 75% from untextured to textured surface (**Figure 1.36**). In addition, long sliding condition test shows that the textured surface guarantee low and constant friction coefficient value for a long time compared to the untextured surface. SEM micrographs (**Figure 1.37**) of untextured surface exhibit evident wear track whereas those of textured surface show that lubricant and wear particles fill the dimples, which work like reservoirs of lubricant and debris, maintaining low friction COF between pin and textured surface during sliding [33].

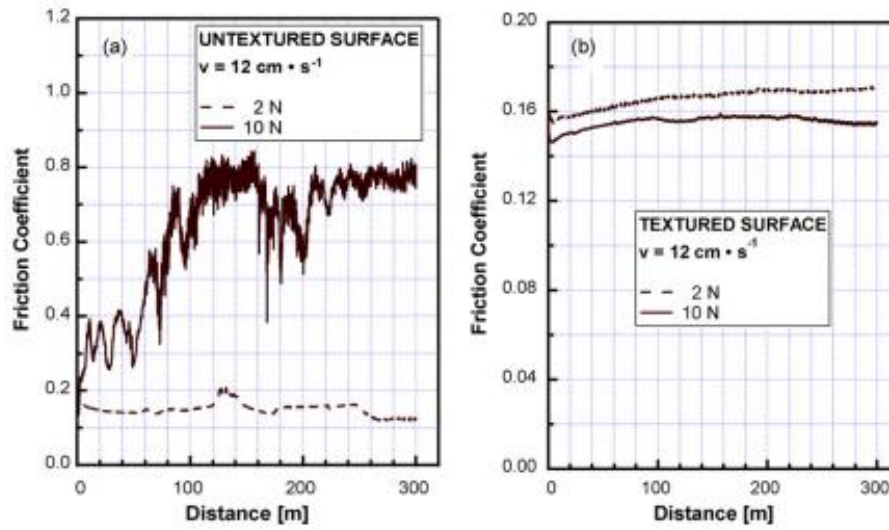


Figure 1.36: COF vs. sliding distance in "single drop" configuration, for untextured (a) and textured surface (b) [33].

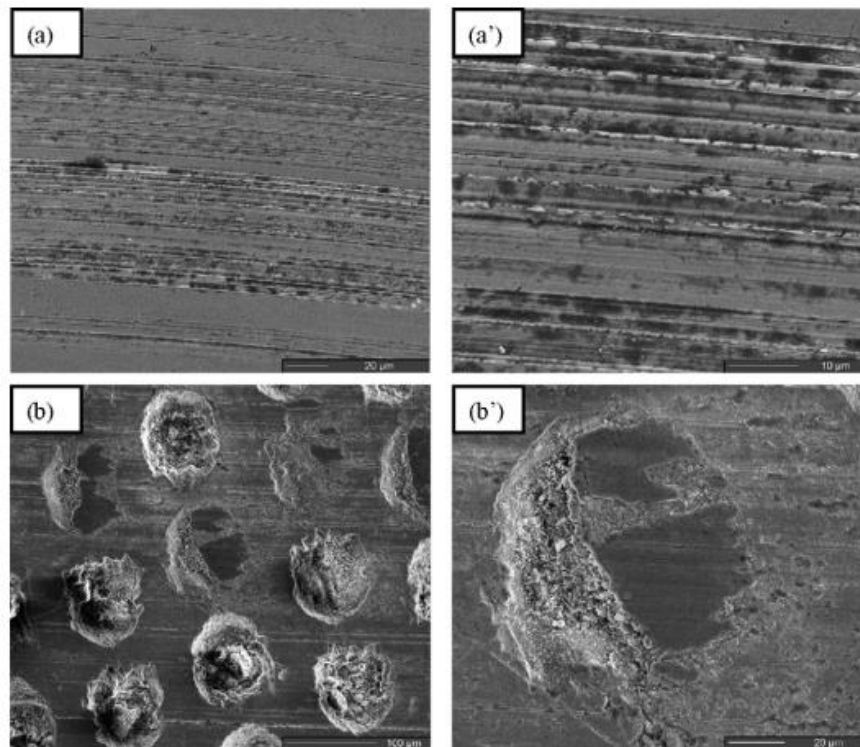


Figure 1.37: SEM micrographs of untextured (a, and its enlarged detail a') and textured (b, and enlarged dimple b') surfaces after pin-on-disc tests performed in "single drop" configuration [33].

2. State of the art

Using the data base ISI Web of Science, it is possible to analyse the number of publications concerning Mg-alloys. **Figure 2.1** shows the number of scientific papers published since 1997 using the “Mg-alloys” as the main keyword. It is noticeable that general trend is clearly upward, following an apparent polynomial trend. It translates the increasing interest in Mg-alloys and their future developments these last decades.

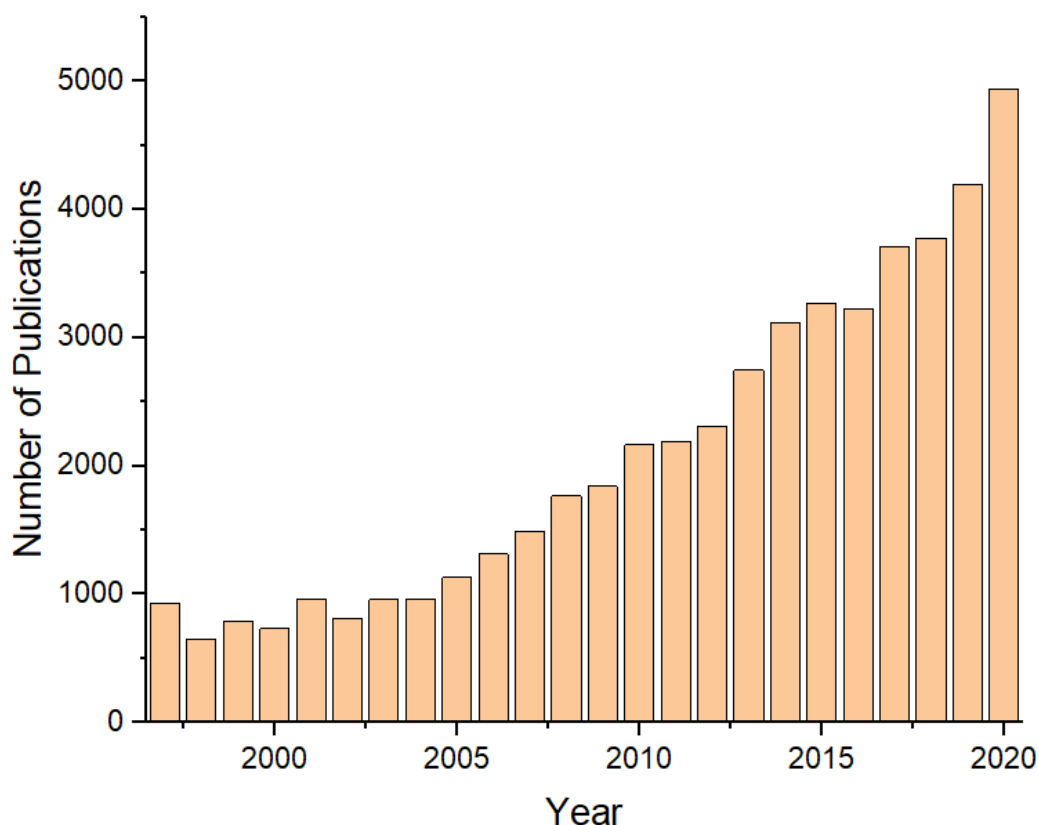


Figure 2.1: General trend of the number of publications concerning Mg-alloys (1997-2020) on ISI Web of Science database.

Figure 2.2 shows all the publications stored in ISI Web of Science database since 1997 concerning LPSO structures, LPSO-containing Mg-alloys and LPSO-containing Mg-Zn-Y alloys as main keywords of search. The general trend is upward since 2007, when the interest for LPSO structures and for the properties of LPSO phases started to blow up. It is noticeable that Mg-alloys occupy an important part of the study of LPSO phases, approximately 60% of the total publications concerning LPSO phases. Furthermore, almost 90% of the LPSO-containing Mg-alloys publications focus on the study system, Mg-Zn-Y. This is due to the superior mechanical properties and the many possible applications in different industries of

this alloy, such as the automotive, the aeronautic or the biomedical industry as briefly explained in sections 1.1.4 and 1.2.4.

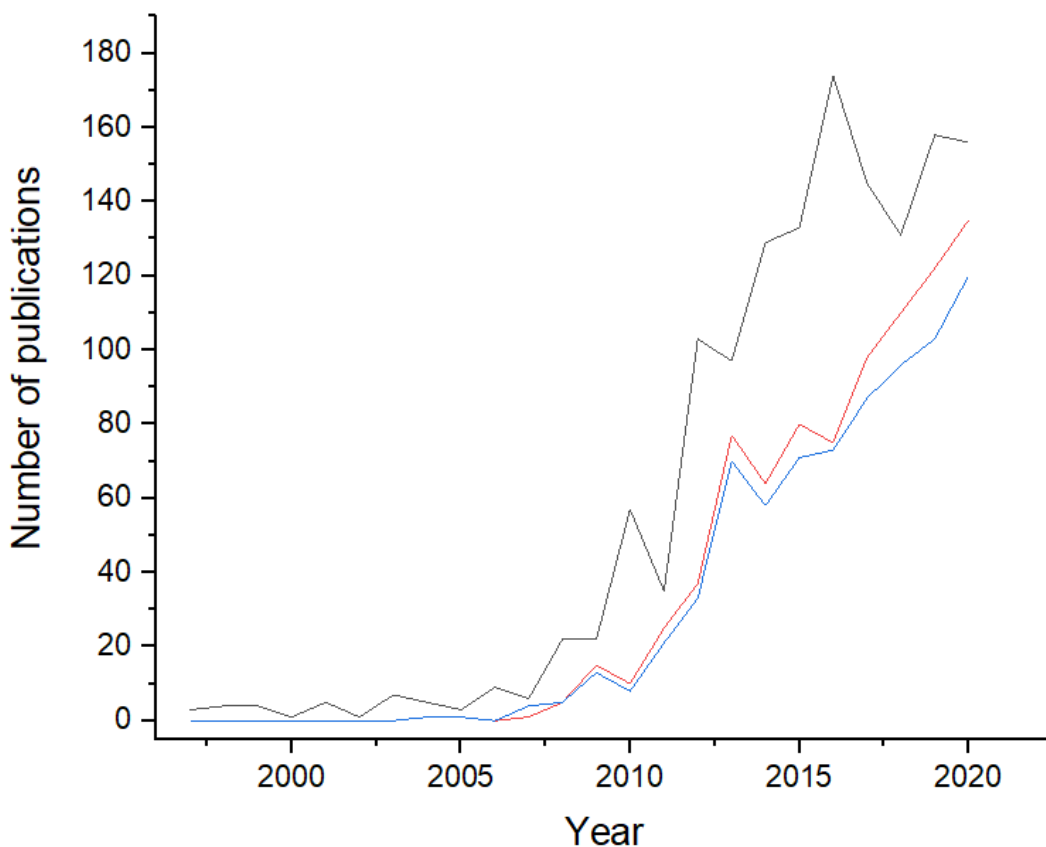


Figure 2.2: General trend of the number of publications on the database ISI Web of Science (1997-2020) using the keywords “LPSO” (black curve), “LPSO Mg-alloys” (red curve) and “LPSO Mg-Zn-Y alloys” (blue curve)

The increasing interest of Mg alloys is also noticed in the field of surface modification. **Figure 2.3** shows the publication concerning surface modifications of Mg alloys and Mg-Zn-Y alloys. The trend is clearly upward, following an apparent polynomial trend, as the previous Mg related research on the ISI Web of Science database. The proportion of publications focused on Mg-Zn-Y alloys represent ~20% of the publications related to surface modification of Mg-alloys each year.

Related to the improvement of mechanical properties of Mg-alloys by surface modification, numerous studies have been published using laser surface treatments and SP [38, 42-45]. For example, Zhang *et al.* [42] have investigated the influence of laser melting and laser texturing on the mechanical properties of Mg-Gd-Ca alloy and reported an increase of hardness and wear resistance due to microstructural modification and the creation of micro-roughness on the surface of the material.

However, no publications were found on the enhancement of mechanical properties of Mg-Zn-Y alloy by surface modification as well as publications concerning the enhancement of mechanical properties

of Mg-alloys by sandblasting, which has been used as surface modification technique during this Master's thesis.

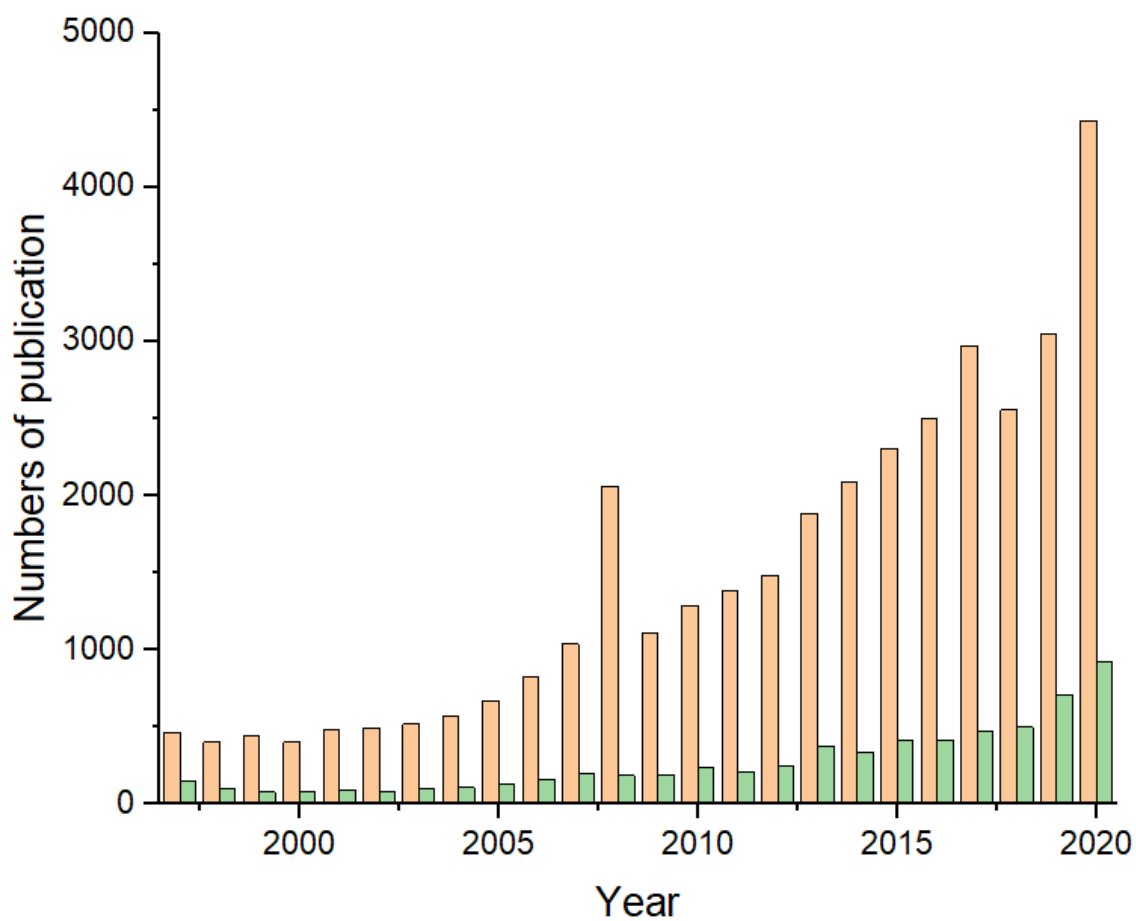


Figure 2.3 : General trend of the number of publications on the database ISI Web of Science (1997-2020) using the keywords « surface modification Mg alloys » and « Surface modification Mg-Zn-Y alloys ».

3. Objectives

The long-term goal of this Master's thesis is to investigate **the effect of sandblasting on the surface roughness and on the mechanical properties of Mg-Zn-Y alloys.**

Within this context, this Master's thesis can be divided into different sub-objectives:

- The first one is focused on the microstructural and mechanical characterization of the 3 reference alloys.
- Then study the superficial roughness as well as characterize the microstructural changes in the near surface layer produced by sandblasting.
- Finally, characterise the superficial mechanical properties of the treated samples and compare them to those of the reference alloys under different stress fields.

4. Experimental methods

4.1. Materials

The Mg-alloys studied in this Master's thesis were supplied by the Centro Nacional de Investigaciones Metalúrgicas (CENIM) of Madrid. The composition and the thermomechanical treatments of the 3 alloys are summarized in **Table 4.1** and the alloys and their denomination are shown in **Figure 4.1**.

Table 4.1: Denomination, composition and thermomechanical treatment of the studied alloys.

Denomination	Composition	Treatment
Alloy 1	MgY ₂ Zn ₁ (at%)	Cast + Extruded at 450°C
Alloy 2	MgY ₇ Zn ₅ (at%)	Cast + Extruded at 450°C
Alloy 3	MgY ₂ Zn ₁ (at%)	Cast + Extruded at 350°C



Figure 4.1: Extruded and rolled alloys.

4.2. Sample preparation

4.2.1. Polishing process

From the Mg-alloys presented in **Figure 4.1** are initially cut the specimens by using the Delta AbrasiMet abrasive cutter from Buehler (**Figure 4.2a**) in two different directions: longitudinal (L) and in the transversal (T) direction. Afterwards, the samples were embedded in bakelite (Blak-B from Metkon) holders using the LaboPress-3 machine from Struers (see **Figure 4.2b**) using the following conditions: 20kN of compression force maintained during 5 min. at 180°C and subsequently cooled for 3 min. using tape water.

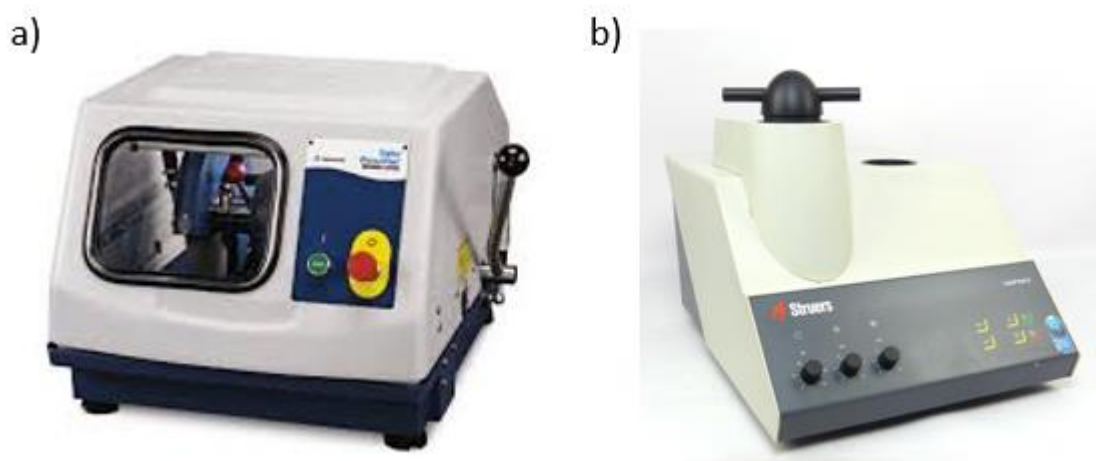


Figure 4.2: Buehler Delta AbrasiMet abrasive cutter (a) and Struers LaboPress 3 device used to form bakelite holders (b) [74,78].

After this step and prior to microstructurally and mechanically characterize each specimen, the different samples were polished until mirror-like surface in order to get a flat surface. In this sense, the polishing process is required to reduce the roughness of the samples as well as the skin created during the extruding and rolling process (i.e. mainly composed of external contaminants and oxides).

In total, 6 samples were polished (one for each direction and specimen) considered as a reference samples and 18 more samples (3 per each condition and direction) in order to get the same surface quality as the reference samples prior to conduct the sandblasting process. The different specimens were polished automatically by using a Neurtek Saphir 520 polishing machine (**Figure 4.3**). The rotation of the sample holder was in the same direction as the plate and the polishing speed was held constant and equals to 150 rpm. The force was kept constant at 25 N for each sample.



Figure 4.3: Neurtek Saphir 520 polishing machine.

The polishing protocol used in this Master's thesis is summarized in **table 4.2**.

Table 4.2: Summary of the different polishing steps.

Step	Disc	Suspension	Rotation speed	Direction	Time	Force
1	MD-Plan	Diamond (30 μm)	150 rpm	In favour	1 min water/ 5 min suspension/ 1 min water	25 N/sample
2	MD-Dac	Diamond (6 μm)	150 rpm	In favour	1 min water/ 15 min suspension/ 1 min water	25 N/sample
3	MD-Dac	Diamond (3 μm)	150 rpm	In favour	1 min water/ 20 min suspension/ 1 min water	25 N/sample

Finally, the specimens were cleaned in an ultrasonic bath for 15 min. and subsequently dried in pure air.

4.2.2. Sandblasting process

Sandblasting, also known as airborne particle abrasion, is a process of impinging a stream of particles on to a target surface with pressure, see **Figure 4.4**. The operating principle consists of particles flowing with the air speed through a nozzle and hitting the target surface from some distance. The immediate

consequence of sandblasting is the erosion of the material due to the impact of the particles (usually alumina), which produces a surface with micro-roughness. Several parameters affect the roughness on the implant surface, mostly particle size, shape, and kinetic energy [39].

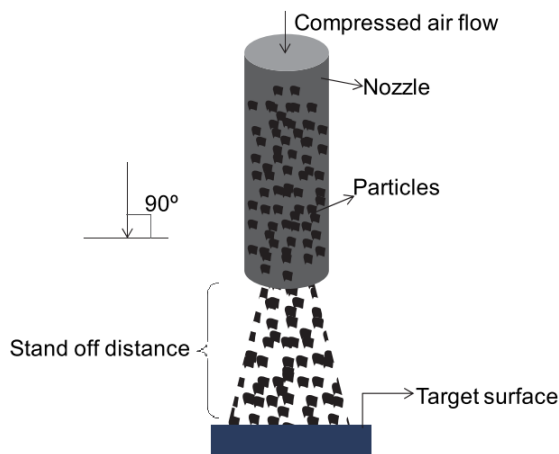


Figure 4.4: Schematic representation of the sandblasting process [39].

The **key strength** of sandblasting is the possibility of performing a homogeneous and gentle anisotropic abrasion on hard materials such as ceramics or glass. However, the **drawback** of this technique is that it could slightly alter the surface chemistry due to inevitable Al_2O_3 contamination.

In this sense, sandblasting is used to modify the surface roughness of the samples as well as to enhance the mechanical properties at the surface layer due to the generation of compressive residual stresses induced during the sandblasting process. This process consists in blasting $110\ \mu m$ alumina powder coming from a nozzle using pressurized air as shown in **Figure 4.4**. In order to produce different roughness states, 3 different air pressures were used in this Master’s thesis: 1, 3 and 5 bars, in both directions investigated here; longitudinal and transversal.

At the end of the sample preparation, 24 samples were investigated along this project. **Table 4.3** summarize the legend of the samples and their surface modifications.

Table 4.3: Summary of all the samples used along this master’s project.

	Polished	Sand blasted	Sand blasted	Sand blasted
		1 bar	3 bars	5 bars
Alloy 1 Longitudinal	S1L	S1L 1 bar	S1L 3 bars	S1L 5 bars

Table 4.3: Summary of all the samples used along this master's project. (continuation)

	Polished	Sand blasted 1 bar	Sand blasted 3 bars	Sand blasted 5 bars
Alloy 1 Transversal	S1T	S1T 1 bar	S1T 3 bars	S1T 5 bars
Alloy 2 Longitudinal	S2L	S2L 1 bar	S2L 3 bars	S2L 5 bars
Alloy 2 Transversal	S2T	S2T 1 bar	S2T 3 bars	S2T 5 bars
Alloy 3 Longitudinal	S3L	S3L 1 bar	S3L 3 bars	S3L 5 bars
Alloy 3 Transversal	S3T	S3T 1 bar	S3T 3 bars	S3T 5 bars

4.3. Characterisation techniques

4.3.1. Microstructural techniques

4.3.1.1. Optical microscope

Various optical microscopes (OM) have been used to evaluate the surface condition of the samples during the polishing process and obtain images of the quality of the sample surfaces along the polishing process until reach a mirror-like surface.

The functioning of an OM is based on the reflection of visible light and a system of lenses to magnify images of small objects. One of the microscopes used during this study is an Olympus BX53M



Figure 4.5: Optical Microscope Olympus BX53M [46].

microscope presented in **Figure 4.5**, which relies on LED illumination and allows magnifications of 5,10, 20, 50 and 100X [46].

4.3.1.2. Laser Scanning Confocal Microscope

The Laser Scanning Confocal Microscopy (LSCM) has been used to visualize the surface of the samples and observe the residual imprints after the mechanical tests conducted under different stress fields.

LSCM is a non-contact optical imaging method that allows a better lateral resolution, an ability to control the depth of field and the realisation of high-resolution 3D imaging compared to conventional OM.

The principle of LSCM, which is represented on **Figure 4.6**, lies in successive scanning of the surface in X-Y planes with the laser beam that is focused by the objective lens to nearly point-like spot. Reflected light is then focused on the detector and outputs the image to the monitor. The main component of the confocality is a pinhole placed at the position that is optically conjugated with the focusing position (confocal plane) to let through only the light coming from the focusing point. As a result, non-focused light is absorbed and thus excluded from the final image production. Besides the scanning in X-Y plane, objective lens controllably shifts in Z direction to gain data from other planes and be able to reconstruct a 3D image of the region of interest. Nevertheless, the size of a step in Z direction is manageable, which affects the vertical resolution: the smaller the size step is, the higher is the vertical resolution. Thereby, theoretically unlimited depth of field is obtained only on the Z range and number of scanned planes. Therefore, a “fully-focused” image and a 3D topographical map of analysed surface is obtained by computer processing [48].

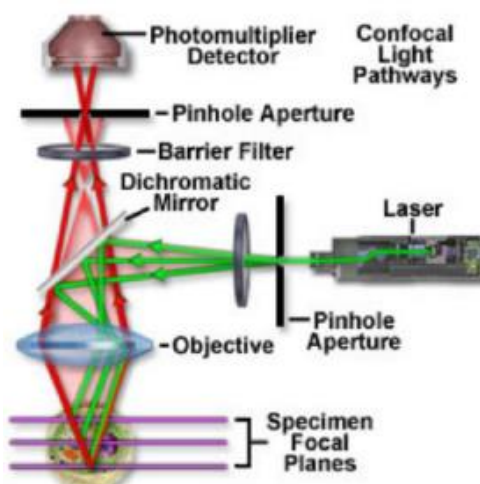


Figure 4.6 : Schematic representation of the LSCM [48]

In this Master's thesis, an Olympus LEXT OLS 3100 (**figure 4.7**) was used for obtaining surface topographic images of the different microstructures before and after the surface modification as well as to observe the residual imprints after doing the mechanical tests.



Figure 4.7: LSCM Olympus Lext OLS 3100 [47].

4.3.1.3. Topography Characterisation by Confocal Chromatic Microscopy

Confocal chromatic microscopy (CCM) is an optical profilometric technique used to 3D images of the sample surface. The main difference with LSCM is the use of white light source instead of a laser beam. The principle of this technique is schematized on **Figure 4.8**. An incident white light beam (W) passes through a chromatic objective (C) which focuses monochromatic light at a different axial position along the Z-axis. When the light encounters the surface of an object, a unique wavelength is perfectly focused on its surface (point M). The reflected light beam then passes through a pinhole which lets only pass the focused wavelength. Finally, the monochromatic light is captured by a spectrometer which calculates the height of point M based on its wavelength [64].

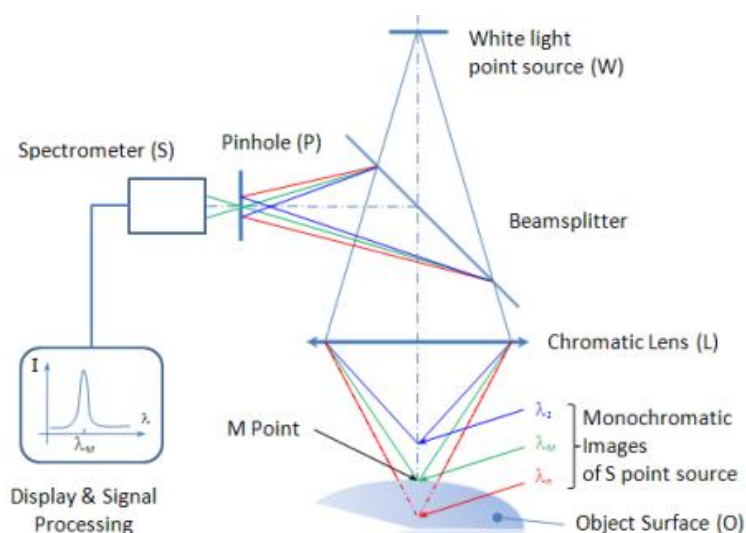


Figure 4.8: Schematic representation of CCM [64].

The machine used during this Master’s thesis is the Optical Profilometer STIL 3D Micromesure 2 (Figure 4.9). This technique has been used to obtain 500 x 500 µm 3D-topography maps of sand blasted samples as well as the main roughness parameters that are listed in Table 4.4

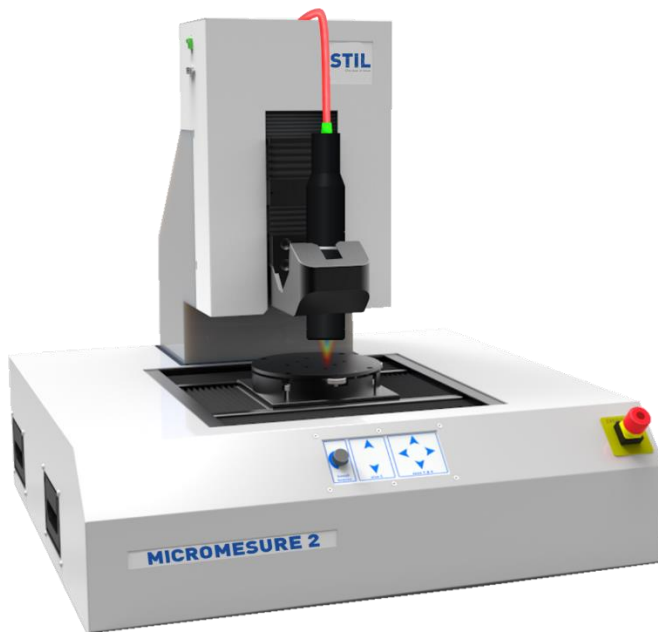


Figure 4.9: STIL 3D Micromesure 2 Optical Profilometer [65].

Table 4.4: Determined surface roughness parameters [59,60,61].

Symbol	Category	Parameter	Description
Sa	Amplitude	Average roughness	Average of height values
Sq	Amplitude	Root mean square (RMS) roughness	Standard deviation of height values
Ssk	Amplitude	Skewness	Degree of symmetry of the surface heights about the mean plane. Its sign indicates the preponderance of peaks (Ssk > 0) or valleys (Ssk < 0)
Sku	Amplitude	Kurtosis	Sharpness or flatness of the height distributions curve Sku = 3: Gaussian height distribution Sku < 3: “broad” height distribution Sku > 3: “narrow” height distribution

Table 4.4: Determined surface roughness parameters [59,60,61]. (continuation)

Symbol	Category	Parameter	Description
Sy, St, Sz	Amplitude	Maximum height difference	Height difference between the highest and the lowest point
S 10z	Amplitude	Ten points peak-peak height	Average difference between the five highest peaks and the five lowest valleys
Sdq	Hybrid	RMS gradient	RMS value of the surface slope
Sdr	Hybrid	Developed interfacial area ratio	Percentage of additional surface area contributed by the texture as compared to an ideal plane size of the measurement region
Spk	Functional	Reduced peak height	Represents the mean height of peaks above the core surface
Sk	Functional	Core height	Difference between the maximum height and the minimum height of the core surface
Svk	Functional	Reduced valley height	Represents the mean height of valleys below the core surface
Smr1	Functional	Peak material portion	Represents the areal material ratio that divides the reduced peaks from the core surface
Smr2	Functional	Valley material portion	Represents the areal material ratio that divides the reduced valleys from the core surface
Std	Spatial	Texture direction	Represents the lay of the surface
Str20	Spatial	Texture aspect ratio	Ratio of the fastest to slowest decay to correlation 20% of the autocorrelation function. Its value is between 0 and 1. For a surface with dominant lay, the parameters will tend towards 0.00 whereas a spatially isotropic texture will result in a value of 1.00

Table 4.4: Determined surface roughness parameters [59,60,61]. (continuation)

Symbol	Category	Parameter	Description
Str37	Spatial	Texture aspect ratio	Ratio of the fastest to slowest decay to correlation 37% of the autocorrelation function. Its value is between 0 and 1. For a surface with dominant lay, the parameters will tend towards 0.00 whereas a spatially isotropic texture will result in a value of 1.00

4.3.1.4. Scanning Electron Microscope

Scanning Electron Microscopy (SEM) is a technique to realize high-resolution images of the surface of a sample using the principle of electron-matter interactions. In this technique, the primary electron beam is traditionally produced by a tungsten wire heated at 2700°C. Then it passes through several magnetic lenses allowing to focalize it, as well as deflection coils to scan the surface of the sample [50]. At this point, the electrons from the primary beam interacts with the atoms of the sample in different ways (Figure 4.10):

- When the primary beam strikes the sample surface causing the ionization of the specimen atoms, loosely bound electrons may be emitted, and these are referred to as secondary electrons (SE). As they have low energy (3 - 5eV), they can only escape from the shallow surface (a few nanometers deep). As a result, SE are used principally for topographic contrast in the SEM.
- A backscattered electron (BSE) is defined as an electron which has undergone a single or multiple scattering events, and which escapes from the surface with an energy greater than 50eV. The elastic collision between an electron and the specimen atomic nucleus causes the electron to bounce back with wide-angle directional change. Elements with higher atomic numbers have more positive charges on the nucleus, and, as a result, more electrons are backscattered, causing the resulting backscattered signal to be higher. Thus, the backscattered yield, defined as the percentage of incident electrons that are reemitted by the sample, is dependent upon the atomic number of the sample, providing atomic number contrast in the SEM images.
- Another type of signal produced by the interaction of primary electrons and the sample is characteristic x-rays. When an inner shell electron is displaced by collision with a primary electron, an outer shell electron may fall into the inner shell to re-establish the proper charge balance in its orbitals following an ionization event. Hence, by the emission of an x-ray photon, the ionized atom returns to ground state. These X-rays are characteristic of

the chemical nature of the atom. Thus, the characteristic X-rays are used for elemental analysis when the SEM is coupled to an Energy Dispersive Spectrometer (EDS) [51].

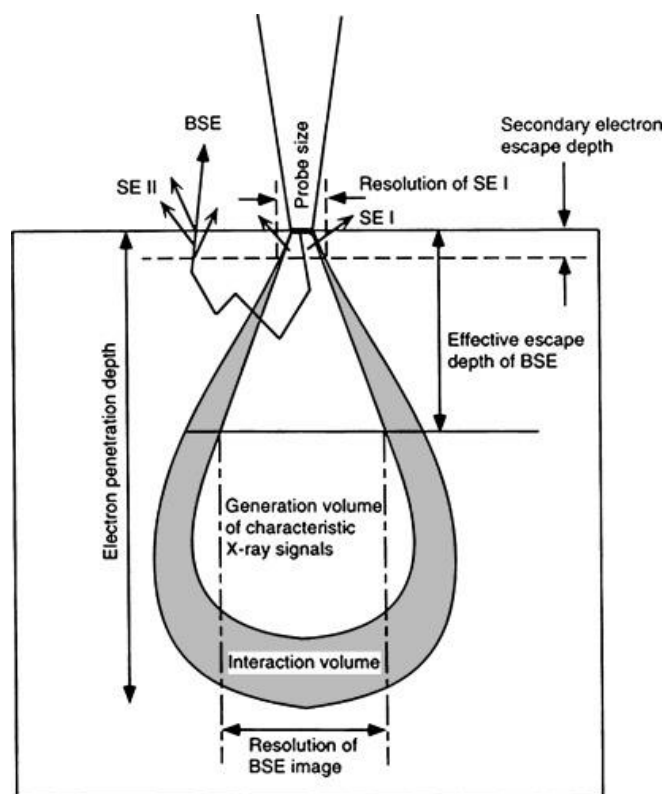


Figure 4.10 : Schematic representation of the electron-matter interactions during SEM [77]



Figure 4.11: SEM Phenom XL [49].

In this research project, SEM Phenom XL (**Figure 4.11**) was used for microstructure characterisation such as grain size and proportion, and elemental analysis. In addition, it was also used to acquire images of the residual imprints conducted under different stress fields; Vickers imprints as well as spherical imprints of monotonical contact fatigue tests.

4.3.1.5. Field Emission Scanning Electron Microscope

The Field Emission Scanning Electron Microscope (FESEM) is a device that realizes high-resolution images of the surface of a sample. Like the SEM, its principle is based on the sputtering of electrons on the sample surface that will interact with the matter. However, the main distinction with the SEM is the way the electron beam is created. While the SEM uses a heated tungsten wire to produce primary electrons, in the FESEM the electrons are liberated by an electrostatic field. Compared to conventional SEM, the FESEM produces clearer, less electrostatically distorted images with a higher resolution [52,53].

During this Master's thesis, the Zeiss Neon 40 FESEM (**Figure 4.12**) was used for imaging residual indentation imprints done under different stress fields. On one hand, it was used to measure the spherical imprints and on the other hand, it was used to observe the superficial damages induced by the indentations.



Figure 4.12: FESEM Zeiss Neon 40.

4.3.1.6. Focused Ion Beam

The Focused Ion Beam (FIB) operates with the same principle of the SEM (see **section 4.3.1.4**), in that a beam of charged particles is directed towards the surface of a specimen. The main difference is that the particles used in this technique are ions, typically gallium ions Ga^+ , which are emitted by a Liquid-Metal Ion Sources (LMIS). The principle (shown in **Figure 4.13**) is based on the heating of gallium (Ga) by a tungsten needle until the Ga wets the needle. Then, thanks to a strong electric field, the Ga atoms

are ionized and directed towards the surface of the targeted sample, creating an ion beam. It is focalized thanks to a system of magnetic lenses and deflectors [76].

When energetic ions hit the surface of a solid sample, different physical effects are visible:

- *Sputtering of neutral ionized and excited surface atoms,*
- *electron emission,*
- *displacement of atoms in the solid,*
- *photon emission and*
- *chemical reactions including the breaking of chemical bonds.*

Based on these phenomena, FIB processing can be used for different applications including: milling, deposition, implantation and imaging. These applications are schematized on **Figure 4.14** [75].

During this Master's thesis, the Neon 40 from Zeiss (shown in **Figure 4.12**) has been used to perform FIB milling and be able to observe and compare the induced damage after sandblasting surface modification with the reference sample.

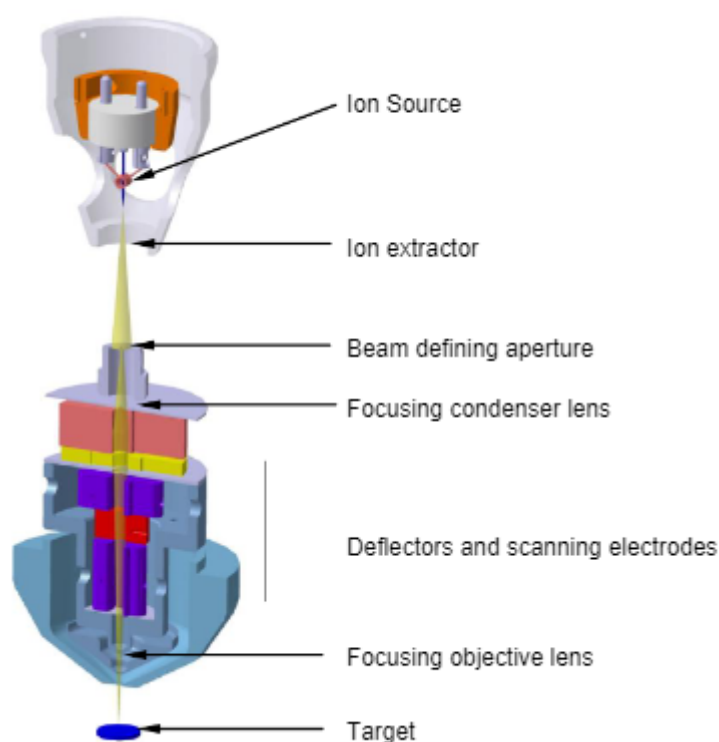


Figure 4.13: Schematic representation of FIB column [76].

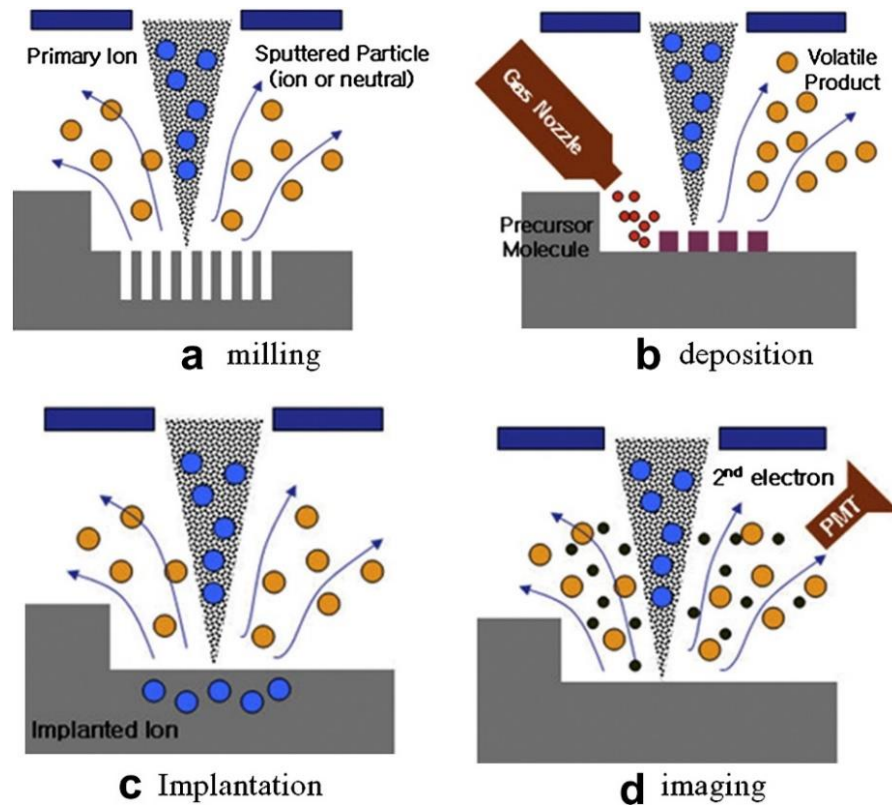


Figure 4.14: Schematic representation of FIB processing: Milling (a), Deposition (b), Implantation (c) and Imaging (d) [75].

4.3.2. Mechanical characterization

4.3.2.1. Vickers hardness test

The Vickers hardness test is the most common method used to measure the hardness of the material. It is one of the easiest tests since the formula that is used for the hardness calculation is independent of the geometrical properties of the indenter. This method is applicable to almost any type of material, but the samples must be completely flat and polished to enable measuring the size of the residual imprints.

This consist of penetrating a square base pyramid diamond indenter with an angle of 136° between faces, as shown in **Figure 4.15**. The indenter by penetrating the surface plastically deforms it, letting a

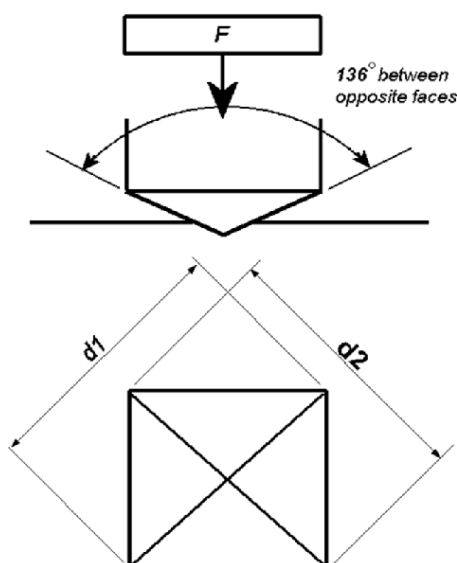


Figure 4.15: Schematic representation of Vickers indenter (top) and Vickers indentation imprint (bottom) [54].

remaining imprint. Then, the geometrical properties of the surface are used to calculate the hardness of the material.

Vickers Hardness (HV) of the material is given by **equation 4**, where F is the applied load (kgf) and d is the average length of the diagonal left by the indenter in millimetres:

$$HV = \frac{2F \cdot \sin(136^\circ/2)}{d^2} \approx \frac{1.8544F}{d^2} \quad (4)$$

In other words, the knowledge of the applied force and the measure of the imprint diagonals allows to calculate the Vickers hardness [55].

In the present work, the indentator Durascan from emcoTest (**Figure 4.16**) was used to determine the Vickers hardness as a function of the applied load. The tests were done for a large range of load from 0.01 to 5 kgf on the polished samples. Between five to ten indentations were done for each load in order to get statistical signification.

On the other hand, this equipment was used to determine the hardness at the micrometric length scale of the sandblasted samples. In this particular case, the tests were conducted at 3 different loads: 0.05, 0.2 and 0.5 kgf. These loads were chosen in order to be able to confine the plastic flow induced inside the modified layer and be able to reduce the influence of the bulk unmodified material and get the Vickers hardness of the modified layer. In this case, due to the induced roughness, ten indentations were performed for each load.



Figure 4.16: EmcoTest Durascan .

4.3.2.2. Hertzian tests: spherical indentation

In addition to the Vickers indentation, spherical indentation tests also known as Hertzian contact tests were performed on all the samples. Similarly to Vickers hardness test, spherical indentation consist of penetrating an indenter on the surface of the sample with a certain load, making an imprint on its surface. However, the indenter here is a sphere (Figure 4.17) [56].

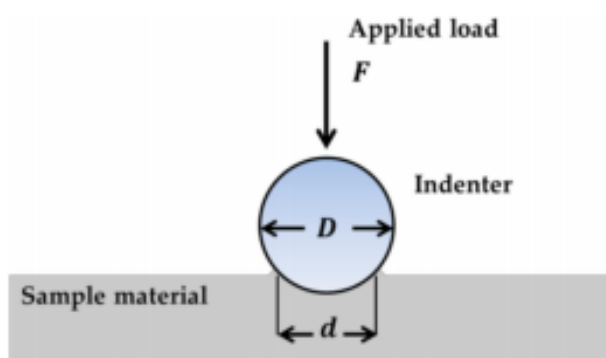


Figure 4.17: Schematic representation of spherical indentation [11].

Through this test, it is possible to calculate the mean contact pressure (p_m in MPa) applied by the indenter using the **equation 5**, where F is the applied load (N) and a is the contact point of the residual imprint (mm) [57]:

$$P_m = \frac{F}{\pi a^2} \quad (5)$$

In this Master's thesis, the KIP Instron 8511 testing machine (**Figure 4.18**) was used to perform this test. The spherical indenter used has a radius of 2.5mm. The test was performed at different loads: 100, 200, 300, 400 and 500N for all the samples, with a load increase to the desired load of 25N/s, a holding time of 10 sec and a load decrease to the initial load of 25N/s.



Figure 4.18: KIP Instron 8511 testing machine.

5. Results and discussion

5.1. Microstructure analysis of reference alloys

The microstructure of the three reference Mg-alloys has been studied in two different directions (longitudinal and transversal) as depicted in the SEM micrographs presented in **Figure 5.1**.

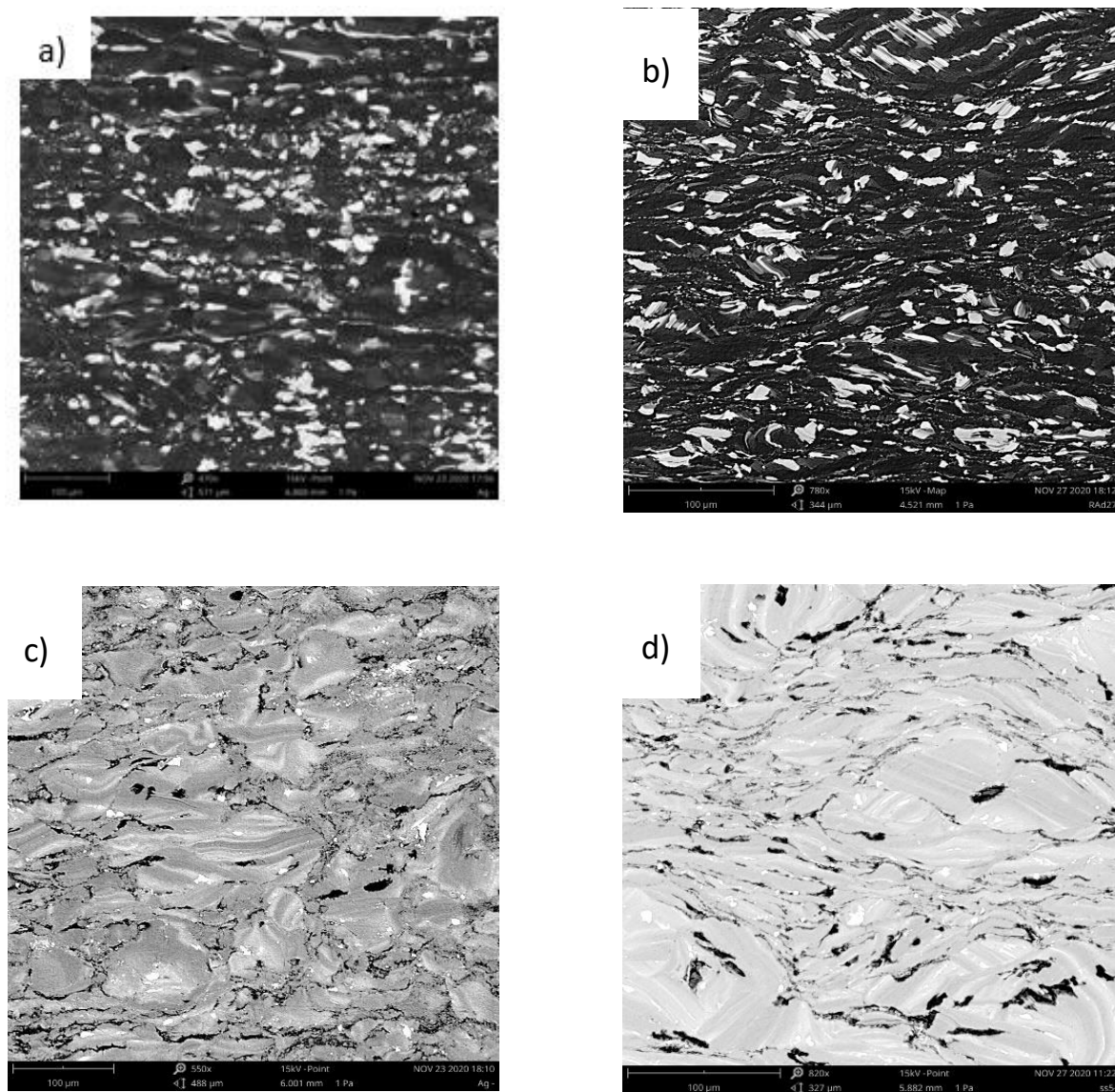


Figure 5.1 : Low magnification SEM micrographs of S1L (a), S1T (b), S2L (c), S2T(d), S3L(e), S3T (f)

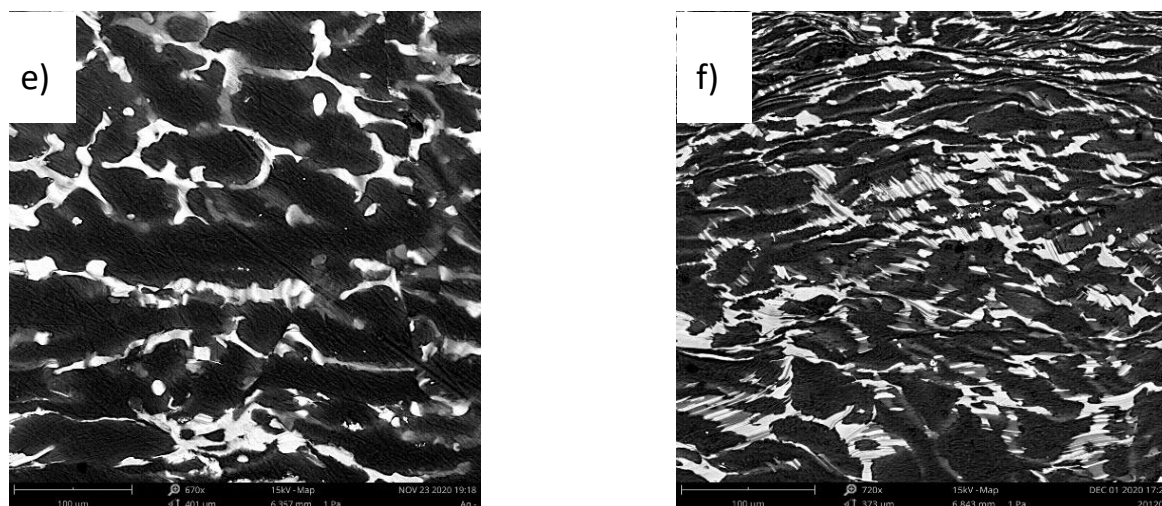


Figure 5.1: Low magnification SEM micrographs of S1L (a), S1T (b), S2L (c), S2T(d), S3L(e), S3T (f) (continuation)

It is noticeable that alloy 1 (**Figures 5.1a** and **5.1b**) and 3 (**Figure 5.1e** and **5.1f**) have an overall similar microstructure which is compound of a matrix appearing in dark and a secondary phase in white, similar to LPSO containing $MgYZn_2$ alloys. On the other hand, alloy 2 (**figures 5.1c** and **5.1 d**) appears much brighter with sparse white and dark phases.

In order to better understand the different constitutive phases present in each Mg-alloy investigated in this Master's thesis, EDS mapping allows to have a better idea of the alloying elements repartition heterogeneously in the microstructure. **Figure 5.2** shows the EDS maps for alloy 1 in the longitudinal direction. By combining the EDS maps with the SEM micrograph (Top part in **Figure 5.2**), it is noticeable that the dark matrix is rich in Mg whereas the white grains are rich in Zn and Y. The same results were obtained in the transversal direction and for the alloy 3 (more information about this alloy is available in **Annex A1**).

On the other hand, the EDS maps of alloy 2 (**Figure 5.3**) shows that the main constitutive alloying elements; magnesium, zinc and yttrium are heterogeneously present in the matrix and that the white particles are rich in yttrium and in zinc. Furthermore, the dark areas present in the SEM micrograph, seems at first to correspond to residual porosity distributed along the specimen, which can be seen more precisely on **Figure 5.4a**. In order to clearly visualize if these dark regions are related to this supposition, a FIB cross section was done on this region and directly observe, as it is depicted in **Figure 5.4b**. From this observation, it is possible to highlight, that this phenomenon is related to a secondary phase. However, since no data was found on this alloy, this phase has not been identified. Further investigation needs to be performed to find its nature.

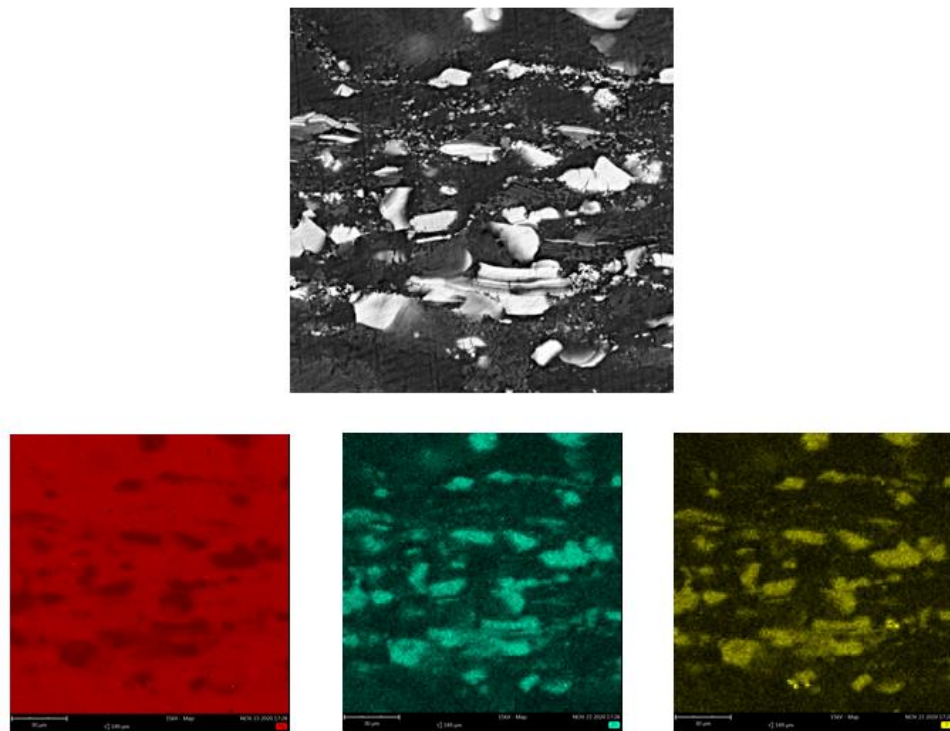


Figure 5.2 : (top) SEM micrograph showing the region of observation and (bottom) EDS maps of the region investigated for the alloy 1 in longitudinal direction Mg in red, Y in yellow, ZN in blue.

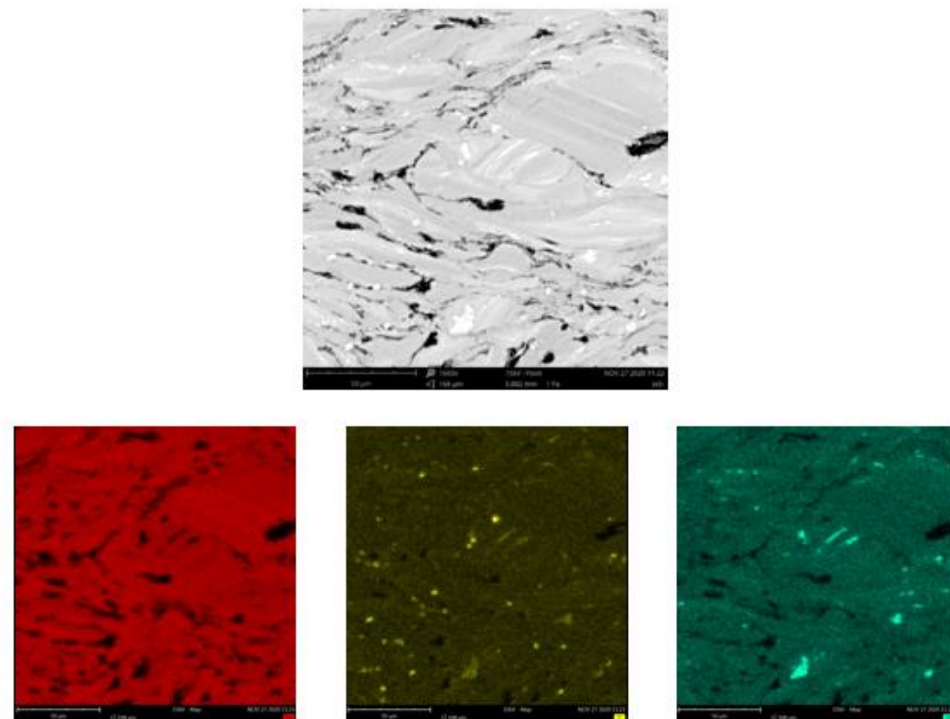


Figure 5.3: (top) SEM micrograph showing the region of observation and (bottom) EDS maps of the region investigated for the alloy 2 in longitudinal direction Mg in red, Y in yellow, ZN in blue.

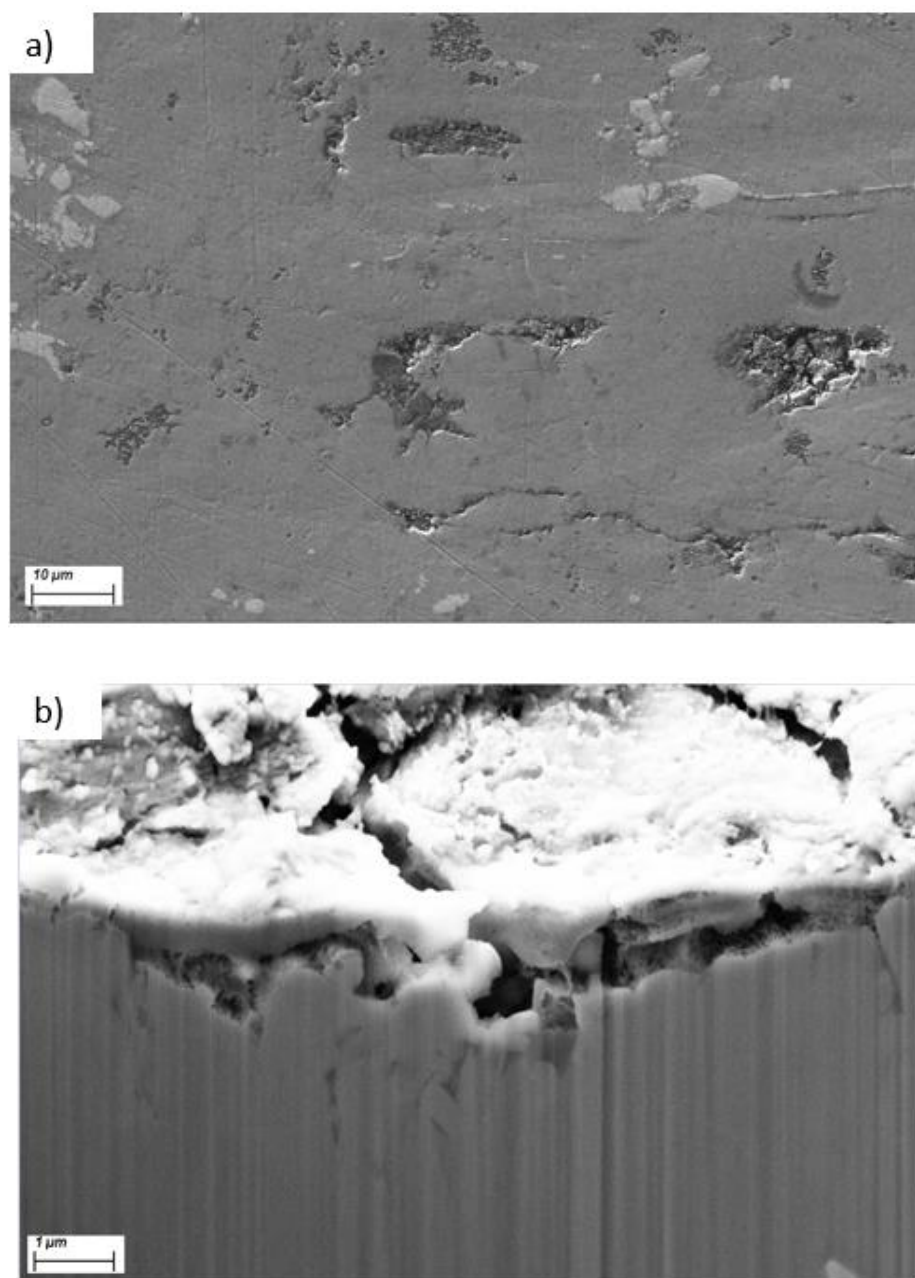


Figure 5.4 : Micrographs of undefined dark phase in alloy 2: FESEM micrograph (a) and FIB cross section micrograph (b)

Figure 5.5 shows the microstructure of alloy 1 in the longitudinal on which a point elemental composition analysis has been performed. The proportion in atomic percentage (at.%) of element of each point is showed in **Table 5.1**. The results show that the dark matrix is composed of 100 at.% of Mg (Point 1 in **Figure 5.5**). The composition of point 2, located on what is supposed to be LPSO phase presents the following chemical composition: 89.6 at.% Mg - 5.9 at.% Y - 4.5 at. % Zn. This composition is in fair agreement with the LPSO phase (90.0 at.% Mg – 6 at.% Y – 4 at. % Zn) as found in [62]. Thus, this phase will be assumed to be LPSO phase. Point 3 is located on a micrometre sized particle and show a high proportion of Y and low amount of Zn. This particle can be spotted where the yellow

appears much brighter on the EDS map of Y as depicted in **Figure 5.2**. This particle is present in low quantity in the microstructure and is assumed to be a precipitate. Finally, the grey contrast (point 4) between the Mg matrix and the LPSO phase shows a low content of Y and Zn. It can be assumed that Y and Zn are present as a solid solution in Mg matrix. Similar results have been found in the transversal direction and in alloy 3 and can be found in **Annex A2**.

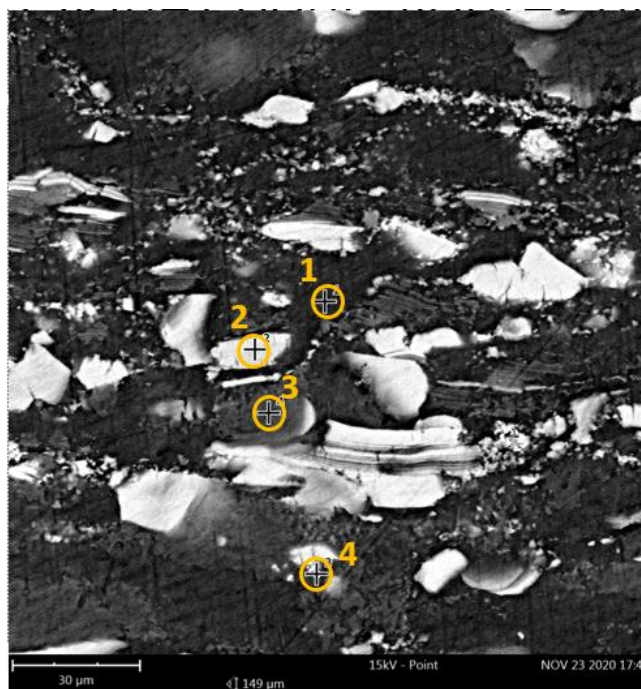


Figure 5.5: SEM microstructure and point localization for elemental point composition of alloy 1 in the longitudinal direction.

Table 5.1: Summary for each of the four different points where the elemental composition is present for S1L.

Element	Point 1	Point 2	Point 3	Point 4
Mg	100	89.6	80.4	98.9
Y	-	5.9	18.6	0.8
Zn	-	4.5	1.1	0.3

Figure 5.6a shows the microstructure of alloy 2 in the longitudinal direction on which an elemental point composition analysis has been also performed. The proportion in at. % of constitutive element for each investigated point is showed in **Table 5.2**. As it is evident in this table, points 1 and 2 presents the following chemical composition: 88.4 at.% Mg - 6.5 at. % Y - 5.1 at.% Zn and 83.9 at. % Mg - 8.7 at. % Y - 7.4 at.% Zn allows to conclude that the grey matrix is in fact LPSO phase. On the other hand, points 3, 4 and 5, located on bright white particles, present a similar composition to that of W phase $Mg_3Y_2Zn_3$ which is reported to be 39.3 at.% Mg - 22.4 at.% Y - 38.2 at.% Zn [63]. Thus, this phase is assumed to be W phase. The W phase corresponds to the bright blue particles on the EDS maps (**Figure 5.3**). Finally, the composition of the dark phase (point 6) is found to be 100 at.% Mg. The composition of alloy 2 in the transversal direction (**Figure 5.6b** and the EDS results are summarized in **Table 5.3**) presents similar results to the one in longitudinal direction except here is found the presence of Y rich particles (points 3 and 5) that appears bright yellow on the EDS maps (**Figure 5.3**).

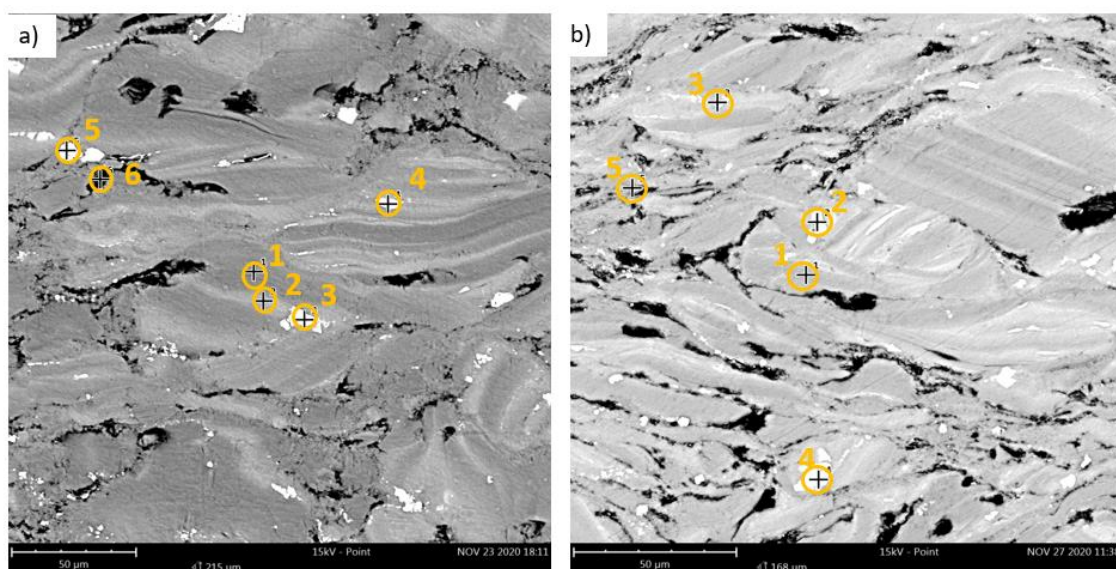


Figure 5.6: SEM micrograph and point localization for elemental point composition of S2L (a) and S2T (b).

Table 5.2: Elemental EDS composition of S2L.

Element	Point 1	Point 2	Point 3	Point 4	Point 5	Point 6
Mg	88,4	83,9	32,8	34,3	37,1	100
Y	6,5	8,7	25,8	25,9	24,3	-
Zn	5,1	7,4	41,5	39,8	38,6	-

Table 5.3: Elemental EDS composition of S2T.

Element	Point 1	Point 2	Point 3	Point 4	Point 5
Mg	88.2	42.0	60.9	37.6	44.8
Y	6.7	24.4	33.6	25.8	52.4
Zn	5.2	33.7	5.5	36.6	2.8

The EDS technique does not provide precise results. To have an exact idea of the present phases, more advanced characterization techniques such as X-ray diffraction need to be performed or even micro probe analysis.

Table 5.4 summarizes the main microstructural parameters for the different specimens investigated in this Master’s thesis. In this sense, in this table the different phase volume fraction and their average size based on the high magnification SEM micrographs shown on **figure 5.7**. The alloys 1 and 3 have the similar LPSO phase volume fraction of ~20% whereas alloy 2 present higher LPSO phase volume fraction of ~90% which is due to the composition of the alloys. In this sense, alloys 1 and 3 are $Mg_{97}Zn_1Y_2$ while the alloy 2 corresponds to $Mg_{88}Zn_5Y_7$ alloy. A higher content of Zn and Y, while keeping the Zn/Y ratio near 0.5 leads to a higher volume fraction of LPSO phase. In addition, the Zn/Y ratio of alloy 2 of ~0.71 is higher than 0.5 leading to the formation of sparse micrometre sized W phase.

The LPSO grains in alloy 1 are smaller than the ones in alloy 3. The higher extrusion temperature leads to reduce the LPSO grains. This may be due to the enhancement of dynamic recrystallization at higher temperature leading to the formation of finer grain microstructure.

Finally, the grain size of LPSO phase/W phase differs whether the sample is observed in the longitudinal direction or in the transversal direction. In fact, the grains are thinner in the transversal direction due to extrusion process.

Table 5.4: Summary of the main microstructural characteristics of the different alloys investigated in this Master’s thesis.

Sample	LPSO phase volume fraction	α –Mg phase volume fraction	W phase volume fraction	LPSO phase average grain size (μm)	W phase average grain size (μm)
Alloy 1 L	17%	83%	-	9.2 ± 1.1	-
Alloy 1 T	20%	80%	-	6.8 ± 0.8	-

Table 5.4: Summary of the main microstructural characteristics of the different alloys investigated in this Master's thesis. (continuation)

Sample	LPSO phase volume fraction	α –Mg phase volume fraction	W phase volume fraction	LPSO phase average grain size (μm)	W phase average grain size (μm)
Alloy 2 L	90%	9%	1%	Matrix	4.0 ± 0.5
Alloy 2 T	91%	7%	2%	Matrix	3.0 ± 0.4
Alloy 3 L	19%	83%	-	18.4 ± 2.9	-
Alloy 3 T	25%	80%	-	14.0 ± 2.1	-

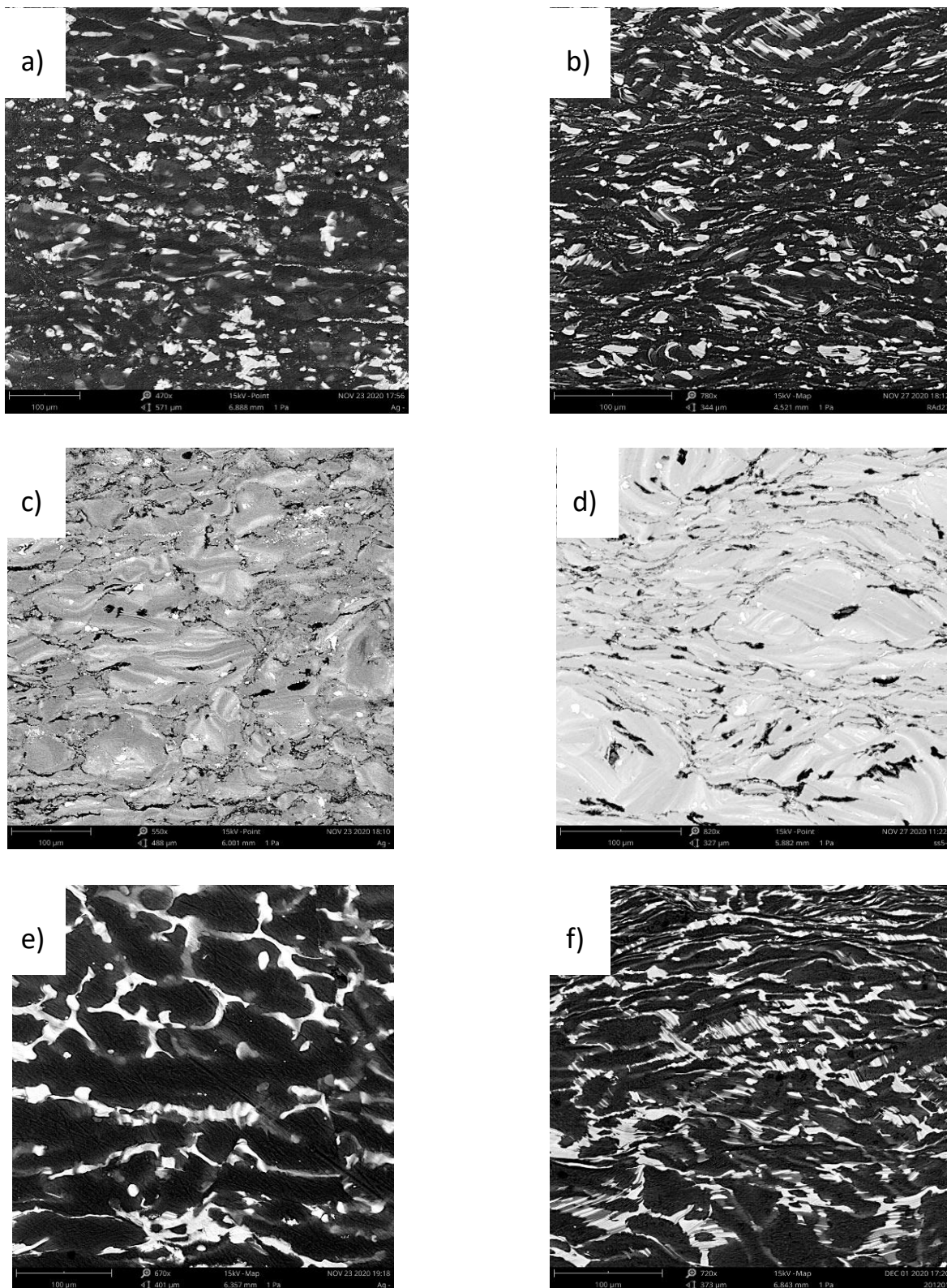


Figure 5.7: High magnification SEM micrographs of the alloys: S1L (a), S1T (b), S2L (c), S2T (d), S3L (e) and S3T (f).

5.2. Surface characterization of the sandblasted samples

The sandblasting process created micro-roughness on the surface of the samples which has been characterised by CCM. **Figure 5.8** shows a 3D surface tomography image obtained of a sample sandblasted at 5 bars of pressure, where some hills and valleys are clearly visible with a maximum difference on height of around $50\ \mu\text{m}$. Furthermore, some white areas are present on this image, which corresponds to regions where the difference on height is higher than the maximum Z-resolution of the CCM equipment.

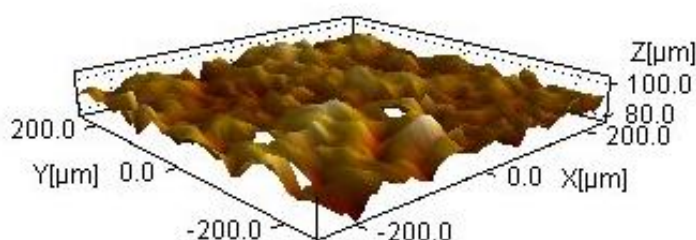


Figure 5.8: 3D tomography image of S1L 5 bars.

Figure 5.9 shows SEM micrographs of the surface of S1L 5 bars. It is visible on this image that the sandblasting created micro-roughness composed of holes, valleys, peaks, scratches, material removal and cracks on the surface of the sample. In other words, this treatment induces some microstructural changes and as a consequence due to this process the compressive residual stresses induced during this process, enhances the micromechanical properties. This result is a consequence of the abrasive erosion caused by this technique. In addition, alumina (Al_2O_3) particles have been identified on the surface of the sample, in white on **Figure 5.9d**. This has been found using point EDS, the result being 71.4 at.% O - 28.6 at.% Al.

Figure 5.10 shows the cross section of a polished and sandblasted sample of alloy 2 (sandblasted at 3 bars of pressure) obtained by FIB milling. It is visible that the sandblasting process has deformed the microstructure of the near surface of the sample. It is clearly evident that the Mg-alloy grains follow the hills and valleys produced during the sandblasted process as it is marked in **Figure 5.10** by a white dash line. Besides, the presence of broken particles was observed on the surface due to the interaction Al_2O_3 particles/material.

The roughness parameters have been determined by CCM. In this Master's thesis, the main amplitude parameters S_a , S_q , S_z , S_{10z} and S_{sk} as well as the hybrid parameter S_{dq} have been retained as descriptive of the surface state. **Figure 5.11** shows the evolution of these parameters in function of the

blasting pressure. On **Figure 5.11e**, some points are not represented because their Sdq values were around 10,000; which seems to be incoherent. Overall, Sa , Sq , $S10z$ and Sdr increase with the sputtering pressure. In fact, an increase of the sandblasted pressure an increase in velocity of the abrasive particles and consequently an increase of their kinetic energy. Thus, the erosion rate increases leading to greater height differences between the peaks and the valleys. Furthermore, the overall skewness of the modified surfaces is negative meaning that there is a predominance of valleys, which is due to the removal of material from an originally flat surface. It is also noticed that Sz seems to be maximum for a pressure of 3 bars, and Ssk seems to be minimum for the same pressure.

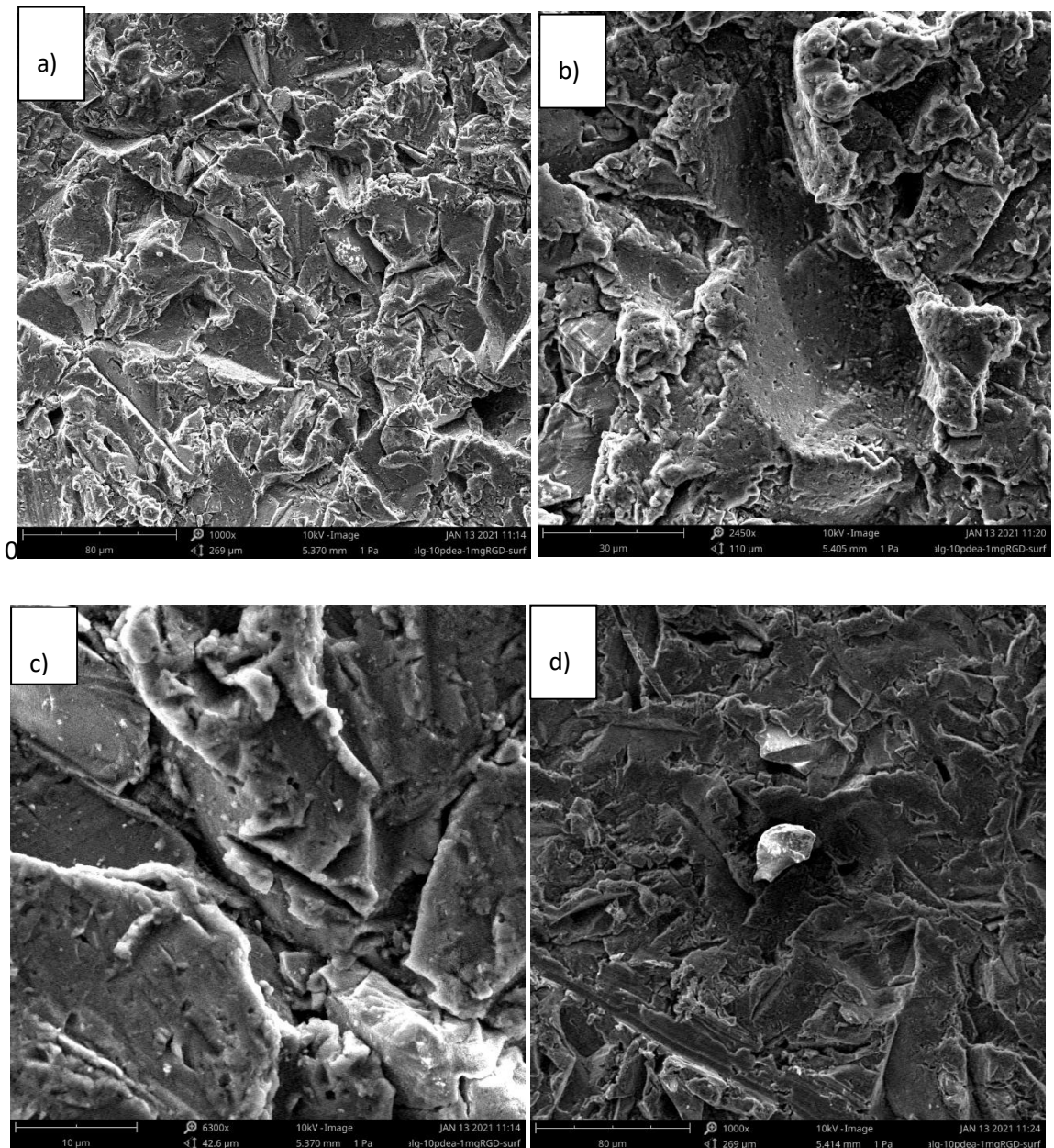


Figure 5.9: SEM micrograph of S1L 5 bars : at low magnification (a), material removal (b), crack (c) and remaining alumina particle (d).

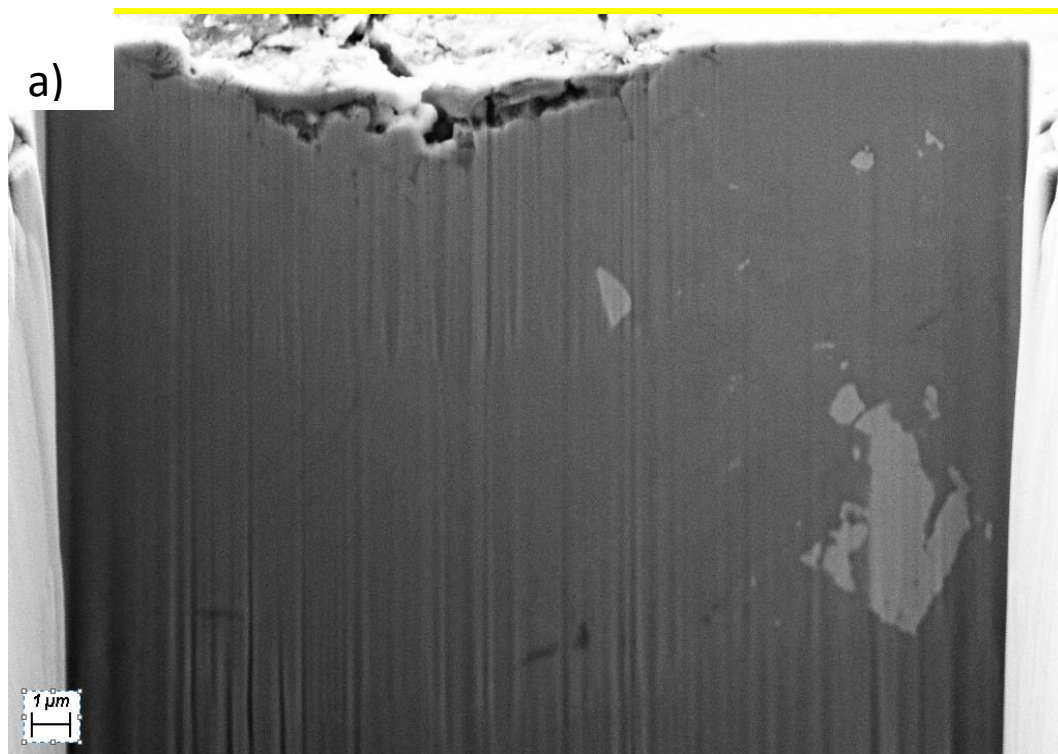


Figure 5.10 : Cross-section micrographs made by FIB of S2L (a) and S2L 3 bars (b).

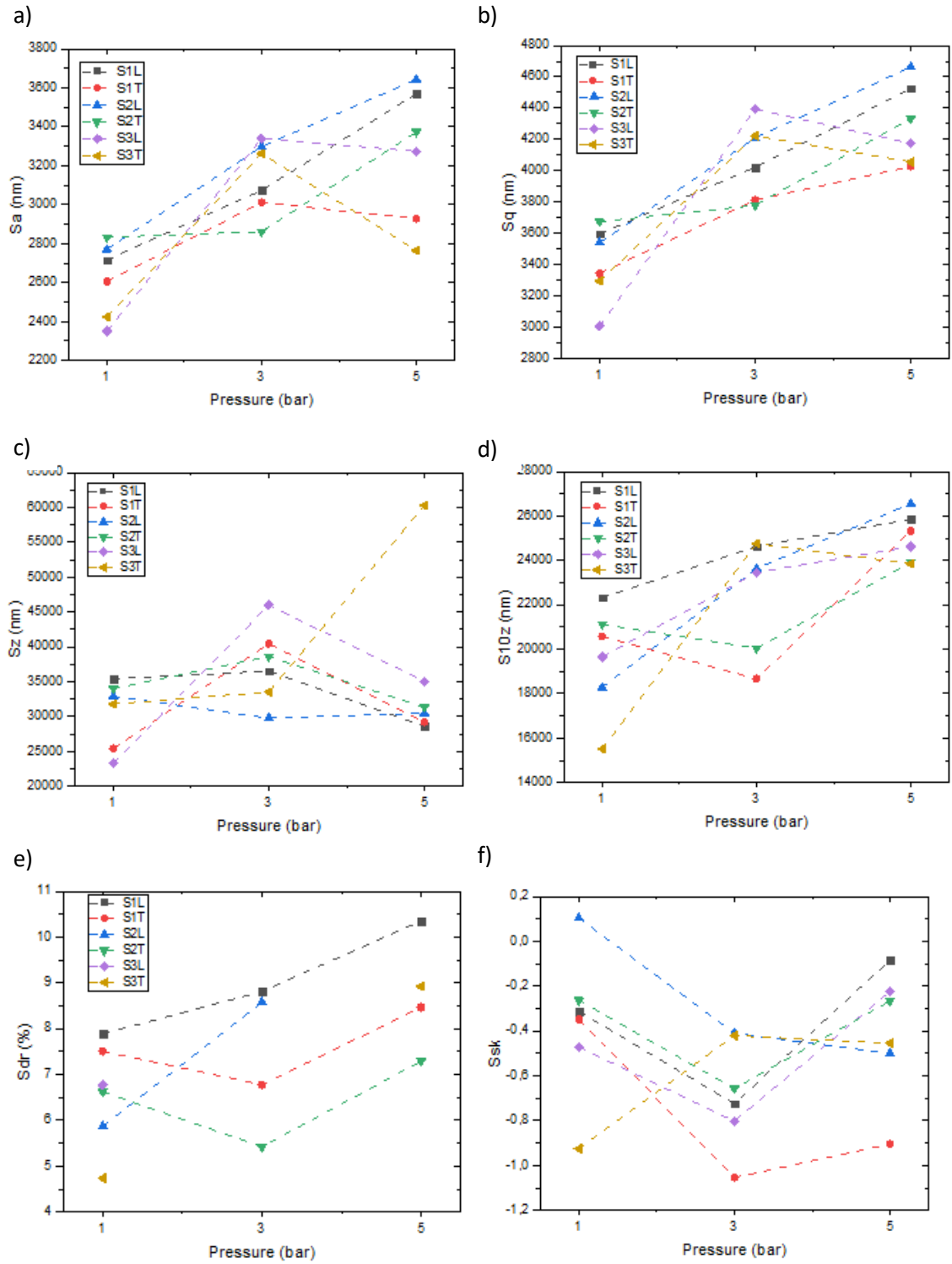


Figure 5.11: Main roughness parameter versus applied pressure for Sa (a), Sq (b), Sz (c), S10z (d), Sdr (e) and Ssk (f)

5.3. Mechanical properties

5.3.1. Vickers Hardness

Vickers hardness has been measured for both, the non-modified samples as well as for the modified samples. As it is shown in **Figure 5.12**, it is noticeable alloy 2 has the highest hardness out of them, which is due to its microstructure. In fact, it presents more vol. % phase fraction of around 90% of LPSO phase than the 2 other alloys, leading to a higher hardness as previously reported in [27]. In addition, alloy 3 has higher hardness values than alloy 1. This is a consequence of the temperature of extrusion, alloy 3 was extruded at 350°C, while alloy 1 it was extruded 100°C higher than alloy 3. On the other hand, the plastic deformations induced by extrusion creates more strain hardening at lower temperature, leading to increase the resulting hardness of the material.

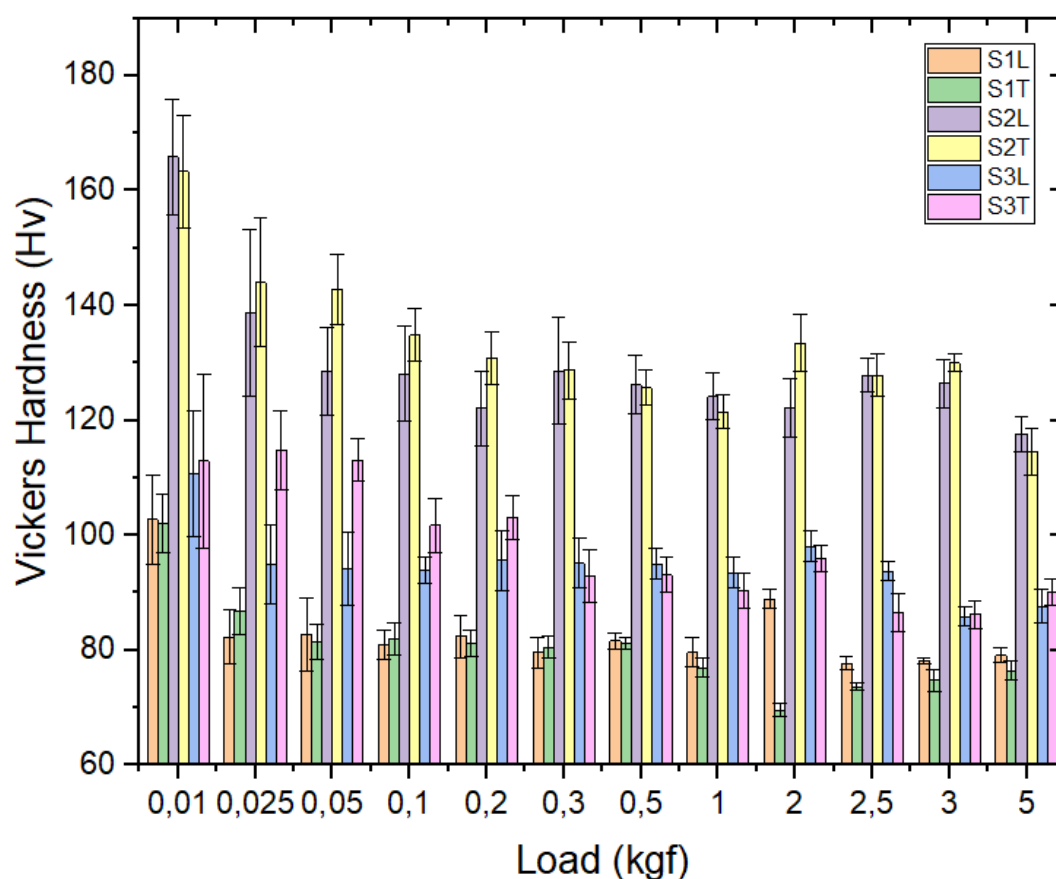


Figure 5.12: Vickers hardness of the polished alloy samples as a function of the maximum applied load.

In addition, as it is clearly evident in **Figure 5.12**, the Vickers hardness decreases when the indentation load increases. This phenomenon is called Indentation Size Effect (ISE). In fact, smaller indents have

higher strain gradients relative to the size of the plastic zone and hence, have a higher hardness value. Nix and Gao [66] have developed a model linking the hardness to indentation depth as described in **equation 6** as follows:

$$\frac{H}{H_0} = \sqrt{1 + \frac{h^*}{h}} \quad (6)$$

where H is the measured hardness (in HV), h is the penetration depth of the measured hardness (in mm), H_0 is the hardness in the limit infinite depth (in HV), and h^* is a characteristic length (in mm) that depends on the shape of the indenter, shear modulus and H_0 . H_0 is an interesting value because it leads to get the hardness of the material independent of the size of the indentation. **Figures 5.13, 5.14** and **5.15** represents the evolution of Vickers hardness as a function of the indentation depth for the different alloys investigated here. The depth of the indentations were calculated from the hardness values using **equation 7**, [67] as they were not measured.

$$h = \frac{1}{7} \cdot d = \frac{1}{7} \cdot \sqrt{\frac{F}{HV}} \quad (7)$$

where h is the indentation depth (in mm), d is the diagonal length (mm), F the applied load (kgf) and HV the Vickers hardness. The parameters obtained through the fitting (H_0 , h) of the different experimental values are reported in **Table 5.5**. As it is evident in this table, the hardness values in the longitudinal direction are higher than in the transversal direction for all the investigated alloys. This result is due to work hardening at the surface of the material due to the extrusion process.

Then the microhardness has been measured for the sandblasted samples and are also represented on **Figures 5.13, 5.14** and **5.15**. The Vickers hardness versus the indentation depth curves of the sandblasted samples also have been fitted using the Nix and Gao model and compared to the polished samples (**Table 5.5**). It is clearly noticeable that the microhardness of the sandblasted samples ranges between 15 to 50% superior to the polished samples because of the residual compressive stresses induced during this superficial treatment process done by sandblasting. However, at the micrometric length scale there is no apparent difference in hardness between the 3 sandblasting pressures investigated along this master's thesis.

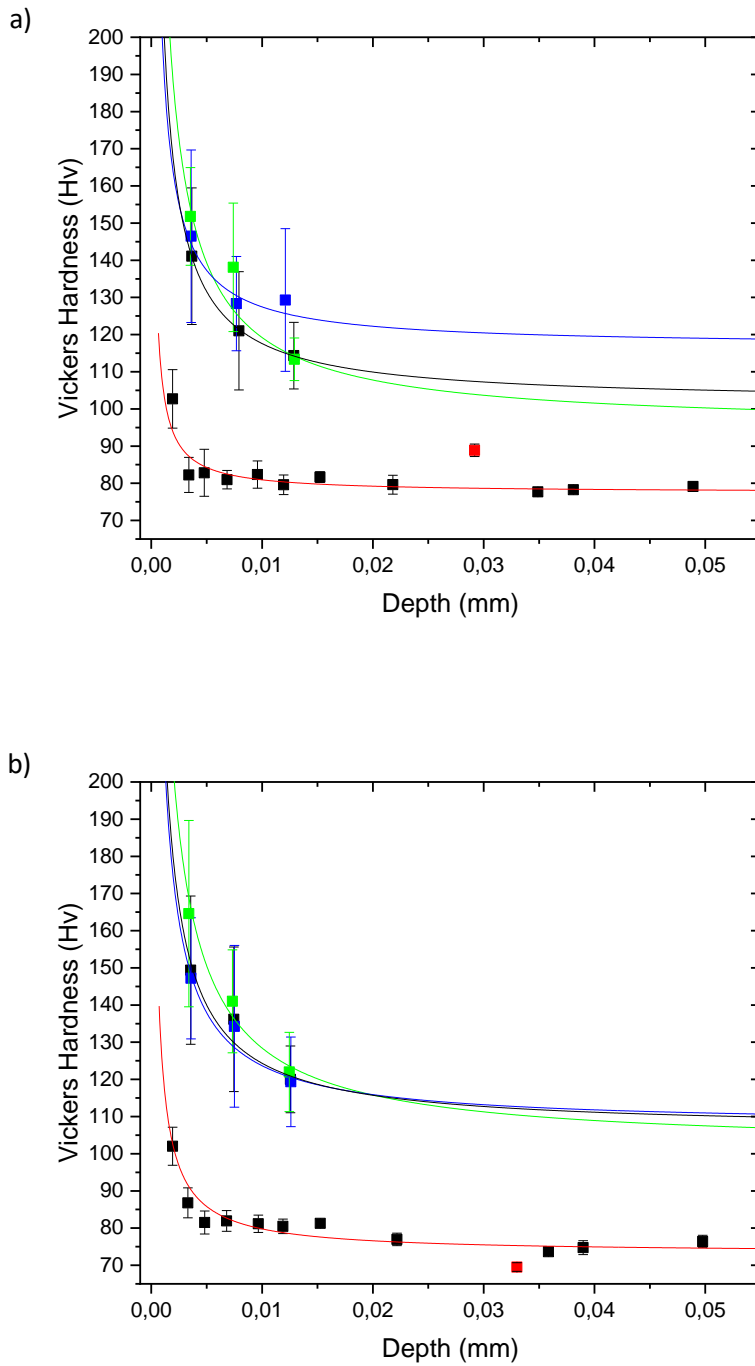


Figure 5.13: Hardness versus indentation depth curves for polished (red) as well as for the sandblasted samples for the alloy 1 (SB 1 bar (black), SB 3 bars (blue) and SB 5 bars (green) S1L (a) and S1T (b))

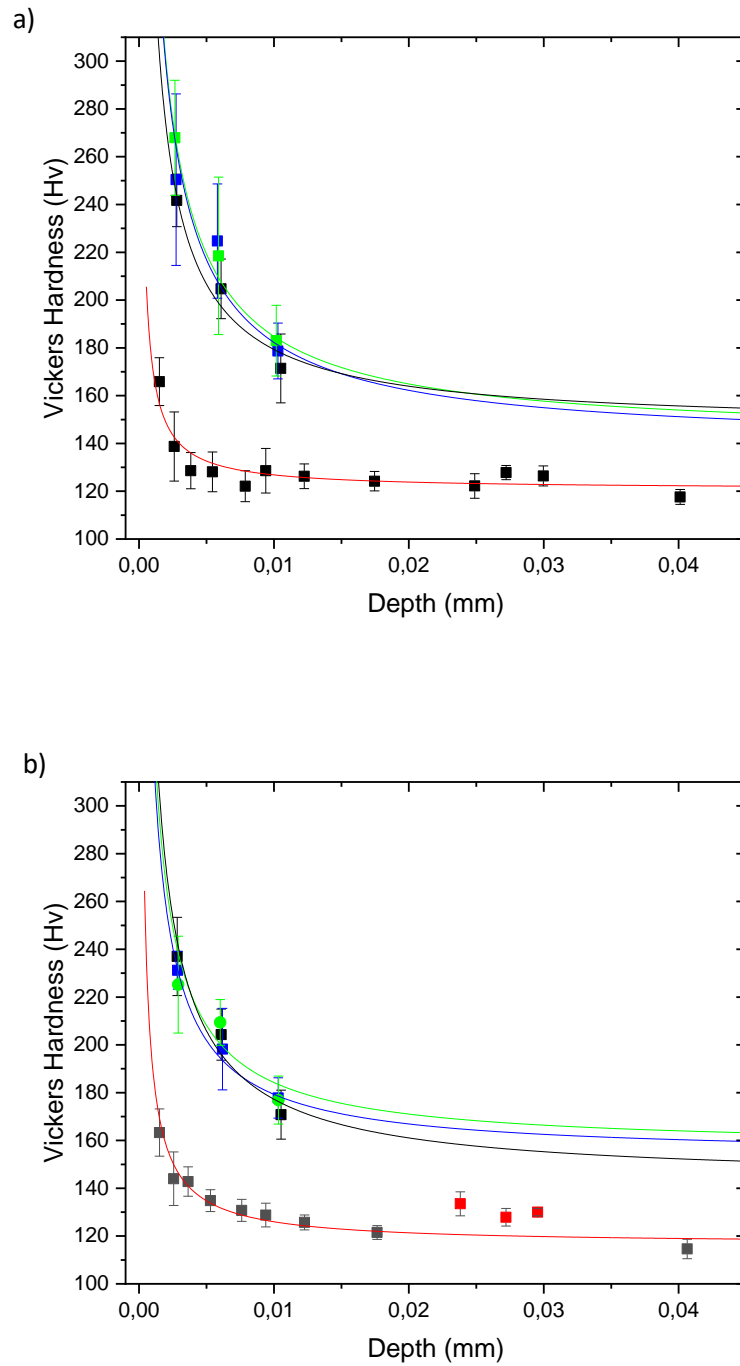


Figure 5.14: Hardness versus the indentation depth curves for polished (red) and sandblasted specimens for the alloy 2 (SB 1 bar (black), SB 3 bars (blue) and SB 5 bars (green) S2L (a) and S2T (b))

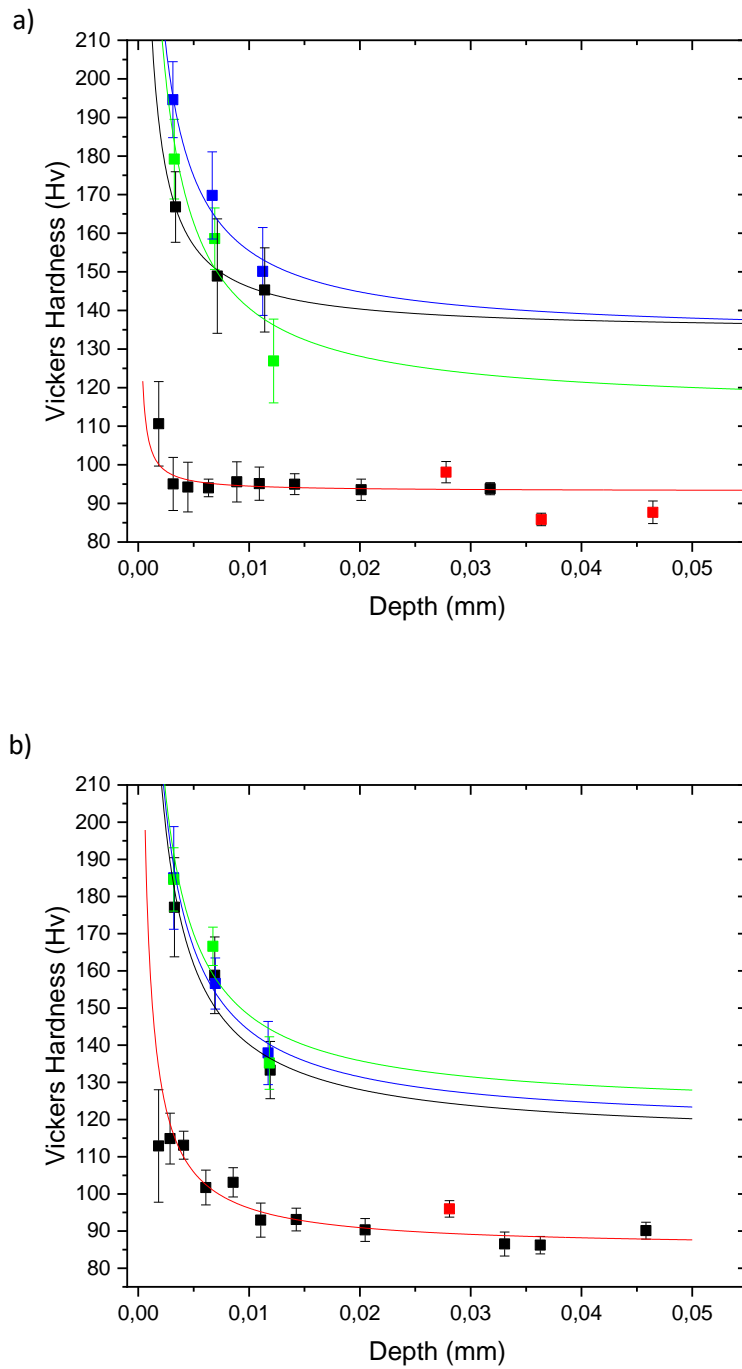


Figure 5.15: Hardness versus the indentation depth curves for polished (red) and sandblasted specimens for alloy 3 (SB 1 bar (black), SB 3 bars (blue) and SB 5 bars (green) S3L (a) and S3T (b))

Table 5.5: Summary of the fitting parameters by using the Nix and Gao model.

Parameters	S1L	S1T	S2L	S2T	S3L	S3T
H0 (HV)	77.5 ± 0.4	73.3 ± 1.1	120.8 ± 1.7	116.7 ± 1.4	93.2 ± 0.7	85.4 ± 1.4
h* (10 ⁻⁴ mm)	9.1 ± 2.3	18.6 ± 4.5	10.3 ± 2.8	16.8 ± 2.1	2.9 ± 1.4	26.9 ± 4.1
R ²	0.68	0.72	0.66	0.94	0.38	0.89

Parameters	S1L 1 bar	S1T 1 bar	S2L 1 bar	S2T 1 bar	S3L 1 bar	S3T 1 bar
H0 (HV)	101.7 ± 0.5	106.4 ± 6.4	147.0 ± 16.1	143.1 ± 19.2	134.4 ± 2.0	114.7 ± 14.6
h* (10 ⁻⁴ mm)	33.7 ± 1.2	36.5 ± 13.8	48.8 ± 0.002	53.5 ± 29.5	18.1 ± 1.9	49.5 ± 29.3
R ²	0.99	0.94	0.96	0.93	0.99	0.90

Parameters	S1L 3 bar	S1T 3 bar	S2L 3 bar	S2T 3 bar	S3L 3 bar	S3T 3 bar
H0 (HV)	116.8 ± 7.2	107.6 ± 5.8	139.3 ± 26.2	153.5 ± 4.0	133.3 ± 8.2	117.7 ± 8.1
h* (10 ⁻⁴ mm)	19.1 ± 10.4	32.2 ± 10.2	71.2 ± 54.1	36.5 ± 4.1	36.0 ± 10.1	49.8 ± 15.9
R ²	0.85	0.96	0.88	0.99	0.97	0.97

Table 5.5: Summary of the fitting parameters by using the Nix and Gao model.

Parameter	S1L 5 bar	S1T 5 bar	S2L 5 bar	S2T 5 bar	S3L 5 bar	S3T 5 bar
HO (HV)	95.0 ± 8.7	101.6 ± 8.8	142.2 ± 8.9	156.7 ± 26.6	114.3 ± 22.0	122.4 ± 24.1
h* (10⁻⁴ mm)	57.6 ± 25.5	59.8 ± 24.3	68.8 ± 15.2	38.2 ± 33.7	51.3 ± 40.6	46.4 ± 41.3
R²	0.94	0.95	0.99	0.77	0.85	0.80

5.3.2. Hertzian contact: spherical indentation

Figure 5.16a shows FESEM micrographs of the spherical indentation performed on S2L. No pile-up phenomenon was observed on the edges of the indentations as presented in **Figure 5.16b**. In addition, the presence of micro-cracks has been spotted near the centre of the indentation, see **Figure 5.16c**.



Figure 5.16: FESEM micrograph of spherical indentation on S2L (a) with a close-up at the edge (b) and in the centre (c) of the indentation.

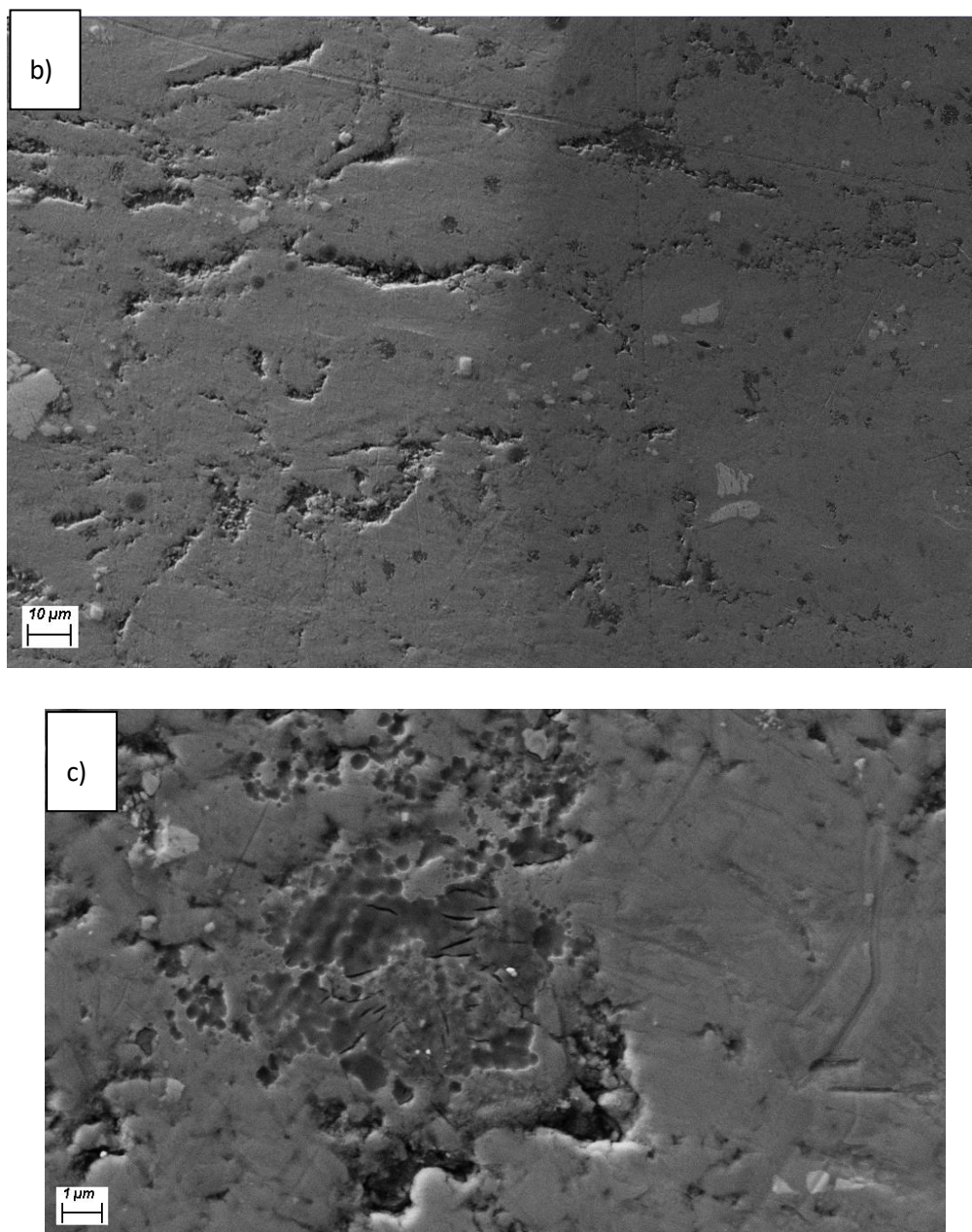


Figure 5.16: FESEM micrograph of spherical indentation on S2L (a) with a close-up at the edge (b) and in the centre (c) of the indentation (continuation).

In addition, the FESEM micrographs revealed a contamination of the surfaces on several samples, especially on S1T (**Figure 5.17**). An EDS analysis has been performed to determine the nature of the contaminants obtaining the following chemical composition: 66.8 at.% O – 30.5 at.% Mg – 2.7at.% C. Which means the contamination is in fact magnesium oxides, surely resulting from the corrosion of the sample after the polishing process.



Figure 5.17: FESEM micrograph of S1T, where the contamination is evident.

Figure 5.18 shows a residual imprint on the alloy 3 sandblasted at 5 bars of pressure. As it is evident, no pile-up and/or cracks are evident. However, the deformation induced during the indentation process is mainly accommodated by the roughness asperities generated during the sandblasting process.

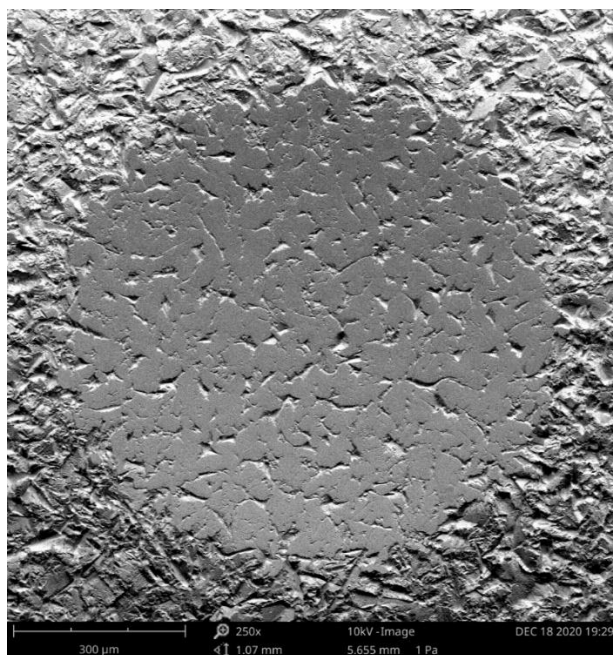


Figure 5.18: SEM micrograph of spherical imprint on S3L 5 bars.

Figure 5.19 shows the evolution of the mean contact pressure determined by using **equation 5** as a function of the applied load for both directions of the polished samples. The mean contact pressure is increasing with the load for S1L and S2L. It increases until reaching 300N and afterwards slightly decreases until it reaches a plateau of around 900 MPa of mean contact pressure for S3L and S3T. On the other hand, it starts to decrease for a load of 200N for S1T. It is also noticeable that the overall mean contact pressure area is higher for alloy 2, then followed by alloy 3 and finally by alloy 1. This result is in concordance with the Vickers Hardness results presented in **section 5.3.1**.

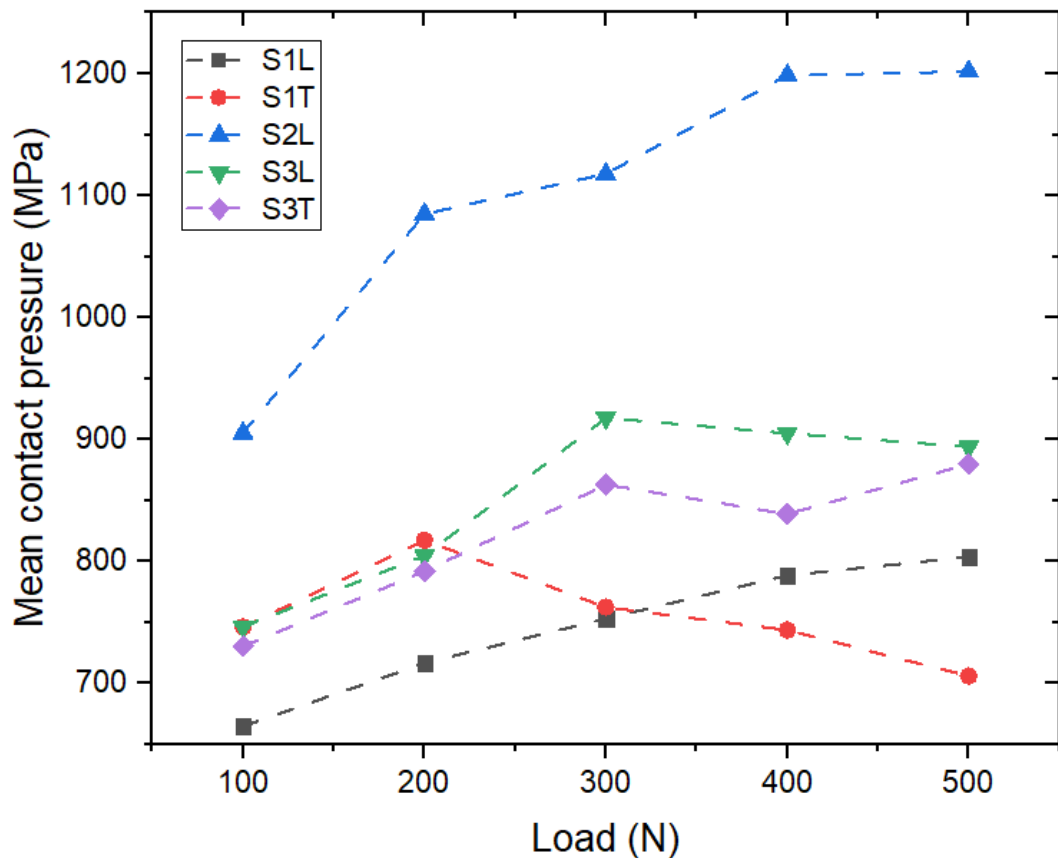


Figure 5.19: Mean Pressure versus applied load trend for the polished samples.

The mean contact pressure of polished and sandblasted samples has been compared, see **Figure 5.20**. However, overall, no clear trend is visible due to the induced roughness generated during sandblasted process mask the real contact point.

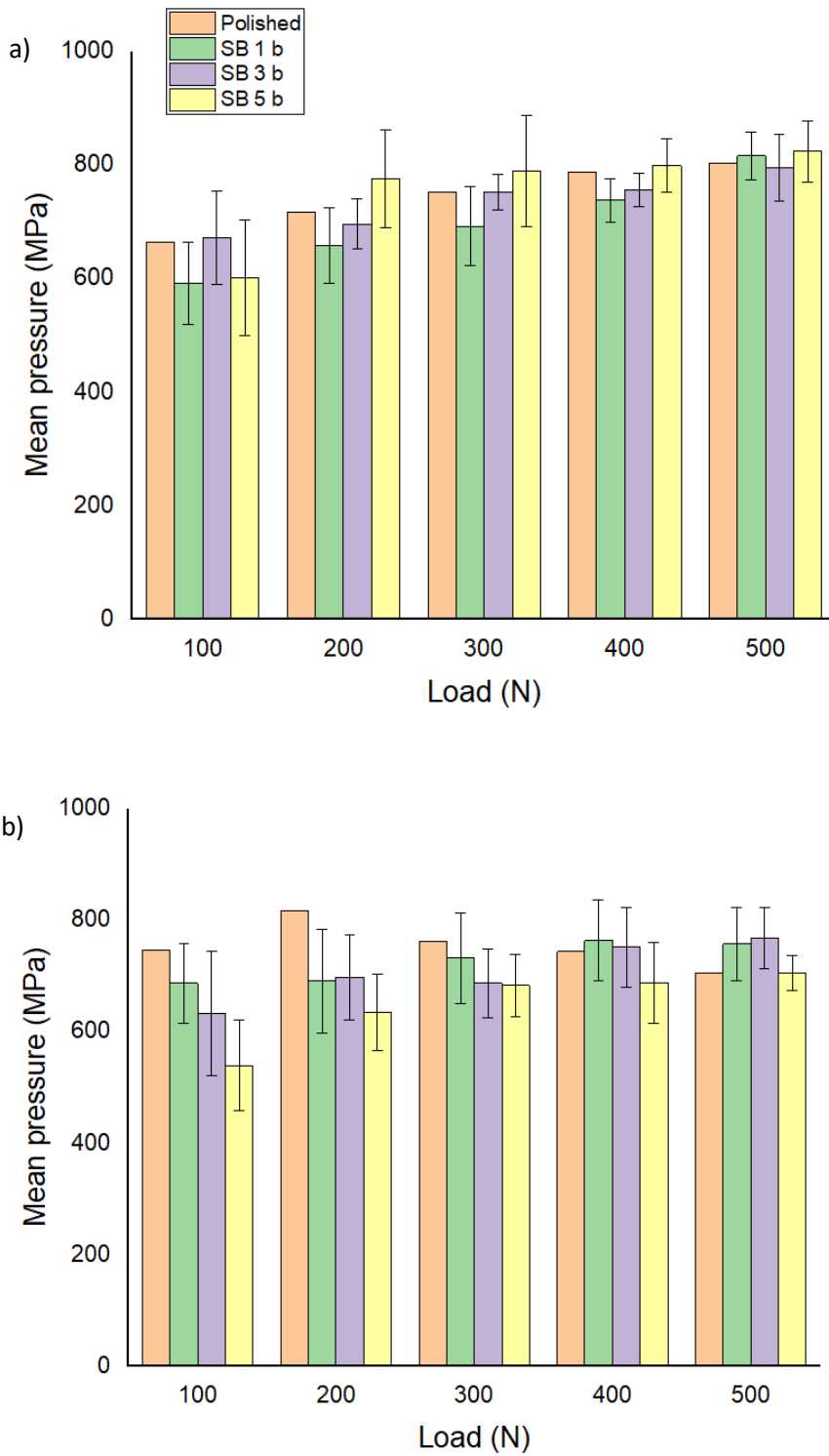


Figure 5.20: Comparison of the mean contact pressure between polished and sandblasted samples; S1L (a), S1T (b), S2L (c), S3L (d) and S3T (e).

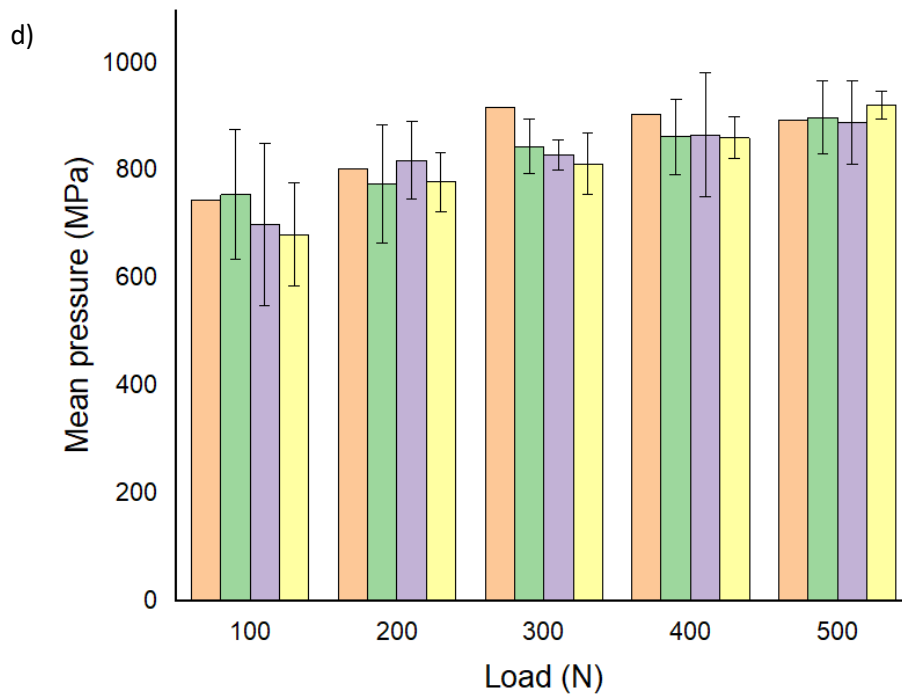
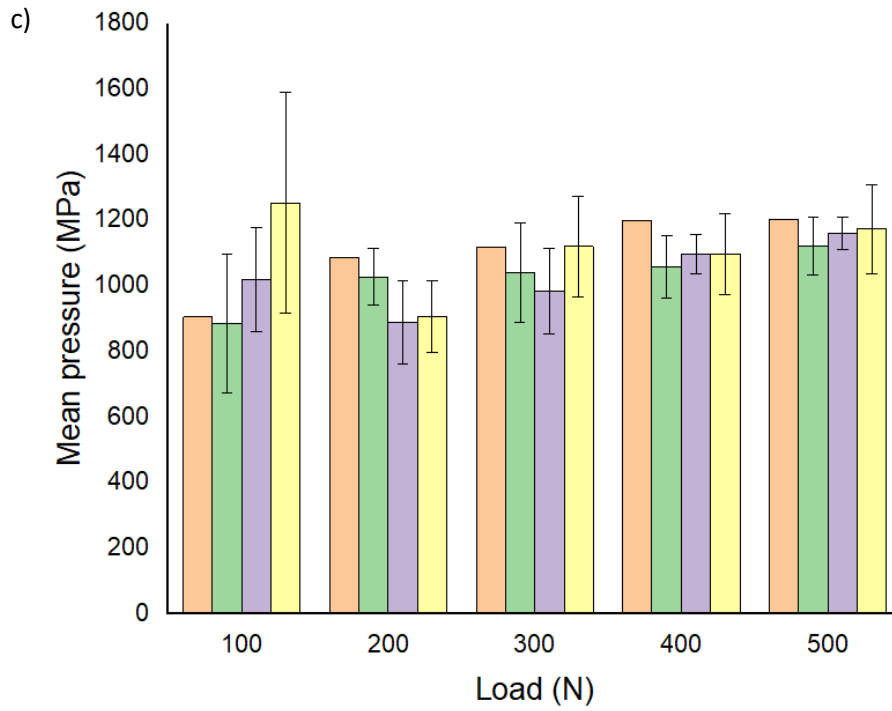


Figure 5.20: Comparison of the mean contact pressure between polished and sandblasted samples; S1L (a), S1T (b), S2L (c), S3L (d) and S3T (e). (continuation)

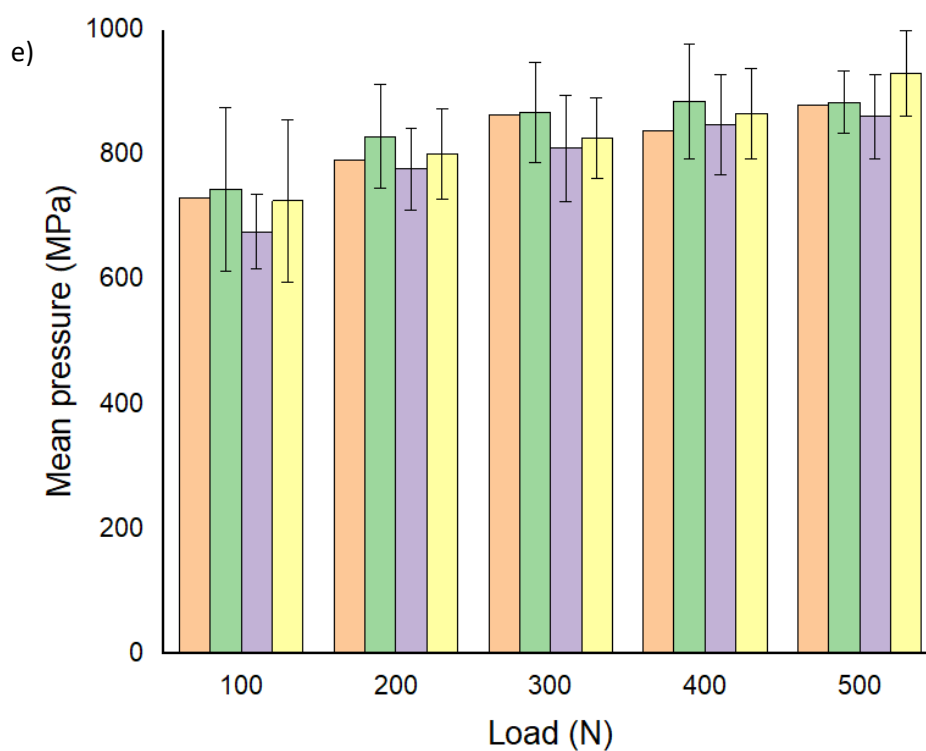


Figure 5.20: Comparison of the mean contact pressure between polished and sandblasted samples; S1L (a), S1T (b), S2L (c), S3L (d) and S3T (e). (continuation)

Environmental impact analysis

During this Master's thesis, the environmental impact is first related to the use of water and chemicals agents employed during sample preparation. In fact, the polishing process, which requires the use of water and polishing suspensions (diamond, colloidal silica and colloidal alumina), took a long time to obtain smooth scratch free surfaces. To reduce the loss of products, the suspensions were used with parsimony.

Regarding the machine used along this project (grinding machine, SEM, heating press to produce bakelite holders, indentation devices, etc), they consumed electrical energy which induces the emission of CO_2 .

Conclusions

In this Master's project, the effect of surface modification by sandblasting on the surface topography and the mechanical properties of 3 different Mg-Zn-Y alloys has been investigated.

The conclusions of this work are listed below:

- The microstructure of the Mg-alloys depends on the chemical composition as well as on the extrusion temperature of the alloys. First, $Mg_{88}Zn_5Y_7$ was found to have the highest volume fraction of LPSO phase ($\sim 90\%$) compared to $Mg_{97}Zn_1Y_2$ ($\sim 20\%$) because of its higher content of alloying elements. As a consequence, the measured Vickers hardness of $Mg_{88}Zn_5Y_7$ is higher than for $Mg_{97}Zn_1Y_2$.
- $Mg_{97}Zn_1Y_2$ alloy extruded at 450°C has finer grains than the one extruded at 350°C . The work hardening effect being higher at lower temperature, the Vickers hardness of the $Mg_{97}Zn_1Y_2$ alloy extruded at 350°C was found to be higher.
- Because of the extrusion process, anisotropy in terms of microstructure and Vickers Hardness was observed between the longitudinal and the transversal direction. In fact, the grains were thinner in the transversal direction while the Vickers Hardness was higher in the longitudinal direction.
- An Indentation Size Effect was observed for low indentation loads and the characteristic parameters were obtained by using the Nix and Gao method.
- The sandblasting process allowed to modify the roughness of the alloys. The roughness amplitude parameters S_a , S_q and S_{10z} increased with the sputtering pressure.
- The surface modification by sandblasting allowed to increase the superficial Vickers Hardness of the material from 15 % to 50 % because of the residual compressive stresses induced by the sandblasting process. Furthermore, this is a consequence of the grain refinement generated during the surface modification process.

Future works

Even though many properties have been studied, other areas to which future works can be directed are remaining. Following is proposed ideas for future works:

- Characterise with more details the microstructure of the samples using XRD to obtain precise phase compositions, and electron backscattered diffraction to observe the effect of extrusion on the texture and the enhancement of dynamic recrystallisation.
- Realize contact fatigue, wear and starch tests to compare the mechanical and tribological response of the material between the polished and the sandblasted samples.
- Extract a transmission electron microscopy for the different sandblasted specimens to characterize the resulting microstructure in terms of plastic deformation mechanisms (i.e. dislocations, twinning, etc.).
- Perform surface modification using other techniques such as shot peening or micro-laser patterning and evaluate the resulting microstructure and mechanical properties.

References

- [1] G. KHELIFATI, L. KIRSCHNER, *Magnésium et Alliages de Magnésium* (2008) p.1-15.
- [2] M. GUPTA, N. M. L. SHARON, *Magnesium, Magnesium Alloys, and Magnesium Composites* (2011) p.1-11.
- [3] L. A. DOBRZANSKI, G. E. TOTTEN, Menachem BAMBERGER, *Magnesium and Its Alloys: Technology and Applications* (2019) p.1-16.
- [4] B. MORDIKE, T. EBERT, Magnesium: Properties-Applications-Potential, *Material Science and Engineering A302* (2001) p.37-45
- [5] M. K. KULEKEI, Magnesium and its alloys applications in automotive industry, *The International Journal of Advanced Manufacturing Technology* (2007) p.851-865.
- [6] K. KISHIDA, K. NAGAI, A. MATSUMOTO, A. YASUHARA, H. INUI, Crystal structures of highly-ordered long-period stacking-ordered phases with 18R, 14H and 10H-type stacking sequences in the Mg–Zn–Y system, *Acta materialia*, 99 (2015) p.228-239.
- [7] Daokui XU, En-hou HAN, Yongbo XU, Effect of long-period stacking ordered phase on microstructure, mechanical property and corrosion resistance of Mg alloys: A review, *Progress in Natural Science: Materials International*, 26 (2016) p.117-128.
- [8] D. EGUSA, M. YAMASAKI, E. ABE, Micro-Kinking of the Long-Period Stacking/Order (LPSO) phase in a hot-extruded Mg97Zn1Y2 alloy, *Materials Transactions*, 54 (2013) p.698-702.
- [9] E. ABE, A. ONO, T. ITOI, M. YAMSAKI, Y. KAWAMURA. Polytypes of long-period stacking structures synchronized with chemical order in a dilute Mg–Zn–Y alloy, *Philosophical Magazine Letters*, 91 (2011).
- [10] H. ZHANG, C.Q. LIU, Y.M ZHU, H.W. CHEN, L. BOURGEOIS, J.F. NIE, Revisiting building block ordering of long-period stacking ordered structures in Mg–Y–Al alloys, *Acta Materialia*, 152 (2018) p.96-106.
- [11] S.C. SANCHEZ, *Diseño y Caracterización de Aleaciones Pulvimetalúrgicas Mg-TR-Zn con Fases Ordenadas de Periodo Largo (LPSO)*, 2014 Universidad Complutense de Madrid.
- [12] J.E. Saal, C. Wolverton, Thermodynamic stability of Mg-based ternary long-period stacking ordered structures, *Acta Materialia*, 68 (2013) p.325-338.

- [13] Q. LUO, Y. GUO, B. LIU, Y. FENG, J. ZHANG, Q. LI, K. CHOU, Thermodynamics and kinetics of phase transformation in rare earth–magnesium alloys: A critical review, *Journal of materials Science & Technology*, 44 (2020) p.171-190.
- [14] X. ZHAO, L.L. SHI, J. XU, Mg–Zn–Y alloys with long-period stacking ordered structure: In vitro assessments of biodegradation behavior, *Material Science and Engineering C*, 33 (2013) p.3627-3637.
- [15] J. ZHANG, J. XU, W. CHENG, C. CHEN, J. KANG, Corrosion Behavior of Mg–Zn–Y Alloy with Long-period Stacking Ordered Structures, *Journal of Materials Science & Technology*, 28 (2012) p.1157-1162.
- [16] C.Q LI, D.K. XU, Z.R. ZENG, B.J. WANG, L.Y. SHENG, X.B. CHEN, E.H. HAN, Effect of volume fraction of LPSO phases on corrosion and mechanical properties of Mg–Zn–Y alloys, *Materials and Design*, 121 (2017) p.430-441.
- [17] P.MAO, Y. XI, K. HAN, Z. LIU, Z. YANG, Formation of long-period stacking-ordered (LPSO) structures and microhardness of as-cast Mg-4.5Zn–6Y alloy, *Material Science & Engineering A*, 777 (2020)
- [18] ASTM, B. Standard practice for codification of certain nonferrous metals and alloys, cast and wrought. *Annual Book of ASTM Standards. Philadelphia, Pennsylvania, USA: American Society for Testing and Materials* (1990)
- [19] A. DZIUBINSKA, A. GONTARZ, M. DZIUBINSKI, M. BARSZCZ. The forming of magnesium alloy forgings for aircraft and automotive applications. *Advances in Science and Technology Research Journal*, 10 (2016) p.158-168.
- [20] J.Y. YANG, W.J. KIM, Effect of I(Mg₃YZn₆)-, W(Mg₃Y₂Zn₃)- and LPSO(Mg₁₂ZnY)-phases on tensile work-hardening and fracture behaviors of rolled Mg–Y–Zn alloys, *Journal of materials research and Technology*, 8 (2019) p.2316-2325.
- [21] D. EGUSA, E. ABE, The structure of long period stacking/order Mg-Zn-RE phases with extended non-stoichiometry ranges, *Acta Materialia*, 60 (2012) p.166-178.
- [22] Y. KAWAMURA, M. YAMASKI, Formation and Mechanical Properties of Mg₉₇Zn₁RE₂ Alloys with Long-Period Stacking Ordered Structure, *Materials Transactions*, 48 (2007) p.2986-2992.
- [23] M. MATSUURA, K. KONNO, M. YOSHIDA, M. NISHIJIMA, K. HIRAGA, Precipitates with Peculiar Morphology Consisting of a Disk-Shaped Amorphous Core Sandwiched between 14H-Typed Long Period Stacking Order Crystals in a Melt-Quenched Mg₉₈Cu₁Y₁ Alloy, *Materials Transactions*, 47 (2006) p.1264-1267.

- [24] E. ABE, Y. KAWAMURA, K. HAYASHI, A. INOUE, Long-period ordered structure in a high-strength nanocrystalline Mg-Zn₁Y₂ alloy studied by atomic-resolution Z-contrast STEM, *Acta Materialia*, 50 (2002)
- [25] Y. KAWAMURA, T. KASAHARA, S. IZUMI, M. YAMASAKI, Elevated temperature Mg₉₇Y₂Cu₁ alloy with long period ordered structure, *Scripta Materialia*, 55 (2006) p.453-456.
- [26] A. INOUE, Y. KAWAMURA, M. MATSUSHITA, K. HAYASHI, J. KOIKE, Novel hexagonal structure and ultrahigh strength of magnesium solid solution in the Mg-Zn-Y system, *Journal of Materials Research*, 16 (2001), p.1894-1900.
- [27] E. OÑORBE, G. GARCES, P. PEREZ, P. ADEVA, Effect of the LPSO volume fraction on the microstructure and mechanical properties of Mg-Zn_{2x}-Zn_x alloys, *Journal of Materials Science*, 47 (2012) p.1085-1093.
- [28] J. AN, R.G. LI, Y. LU, C.M. CHEN, Y. XU, X. CHEN, L.M. WANG, Dry sliding wear behavior of magnesium alloys, *Wear*, 265 (2008) p.97-104.
- [29] B. MAO, A. SIDDAIAH, Y. LIAO, P.L. MENZES, Laser surface texturing and related techniques for enhancing tribological performance of engineering materials: A review, *Journal of Manufacturing Processes*, 53 (2020) p.153-173.
- [30] R.N. BATHE, P. GADHE, S. NIKUMB, Laser surface texturing of gray cast iron for improving tribological behavior, *Applied Physics A*, 117 (2014) p.117-123.
- [31] L.M. VILHENA, M. SEDLACEK, B. POGORNIK, J. VIZINTIN, A. BABNIK, J. MOZINA, Surface texturing by pulsed Nd:YAG laser, *Tribology International*, 42 (2009) p.1496-1504.
- [32] A. GRABOWSKI, M. SOZANSKA, M. ADAMIAK, M. KEPINSKA, T. FLORIAN, Laser surface texturing of Ti6Al4V alloy, stainless steel and aluminium silicon alloy, *Applied Surface Science*, 461 (2018) p.117-123.
- [33] A. BORGHI, E. GUALTIERI, D. MARCHETTO, L. MORETTI, S. VALERI, Tribological effects of surface texturing on nitriding steel for high-performance engine applications, *Wear*, 265 (2008) p.1046-1051.
- [34] J. AN, Y.X. TIAN, C.Q. FENG, Correlation between test temperature, applied load and wear transition of Mg₉₇Zn₁Y₂ alloy, *Journal of Magnesium and Alloys* (2020)
- [35] M. M. AVEDESIAN, H. BAKER, *ASM Speciality Handbook: Magnesium and Magnesium Alloys* (1999) p.3-7.

- [36] R. BIBER, J. PAUSER, M GEßLEIN, H.J. BAIL, Magnesium-Based Absorbable Metal Screws for Intra-Articular Fracture Fixation, *Case Reports in Orthopedics*, 3 (2016) p.1-4.
- [37] J. LU, Traitements de surface mécaniques – Principes, *Matériaux | Traitements des métaux* (2006)
- [38] P. ZHANG, J. LINDEMANN, Influence of shot peening on high cycle fatigue properties of the high-strength wrought magnesium alloy AZ80, *Scripta Materialia*, 52 (2005) p.485-490.
- [39] R.K. CHINTAPALLI, *Influence of sandblasting on zirconia in restorative dentistry*, Universitat Politècnica de Catalunya (2012).
- [40] J.C. BALZA, D. ZUJUR, L. GIL, R. SUBERO, E. DOMINIQUE, P. DELVASTO, J. ALVAREZ, Sandblasting as a surface modification technique on titanium alloys for biomedical applications: abrasive particle behaviour, *Materials Science and Engineering*, 45 (2012).
- [41] X.P. JIANG, X.Y. WANG, J.X. LI, D.Y. LI, C.-S. MAN, M.J. SHEPARD, T. ZHAI, Enhancement of fatigue and corrosion properties of pure Ti by sandblasting, *Materials Science and Engineering A*, 429 (2006) p.30-35.
- [42] J. ZHANG, Y. GUAN, W. LIN, X. GU, Enhanced mechanical properties and biocompatibility of Mg-Gd-Ca alloy by laser surface processing, *Surface and Coatings Technology*, 362 (2019) p.176-184.
- [43] N. PULIDO-GONZALEZ, B. TORRES, M.L. ZHELUDKEVICH, J. RAMS, High Power Diode Laser (HPDL) surface treatments to improve the mechanical properties and the corrosion behaviour of Mg-Zn-Ca alloys for biodegradable implants, *Surface and Coatings Technology*, 402 (2020)
- [44] X. YAO, J. TANG, Y. ZHOU, A. ATRENS, M. S. DARGUSCH, B. WIESE, T. EBEL, M. YAN, Surface modification of biomedical Mg-Ca and Mg-Zn-Ca alloys using selective laser melting: Corrosion behaviour, microhardness and biocompatibility, *Journal of Magnesium and Alloys* (2020)
- [45] S.X. WU, S.R. WANG, G.Q. WANG, X.C YU, W.T. LIU, Z.Q. CHANG, D.S. WEN, Microstructure, mechanical and corrosion properties of magnesium alloy bone plate treated by high-energy shot peening, *Transactions of Nonferrous Metals Society of China*, 29 (2019)
- [46] Industrial Microscopes BX53M, Olympus, <https://www.olympus-ims.com/en/microscope/bx53m/>, assessed 20/01/2021.
- [47] Olympus Confocal Microscope LEXT OLS3100, Tel Aviv University Center for Nanoscience and Nanotechnologies, <https://nano.tau.ac.il/old/index.php/labs/9-equipment/microscopes/14-olympus-confocal-microscope-lext-ols3100>, assessed 20/01/2021.

- [48] J. TOMASTIK, H. SEBESTOVA, R. CTVRTLÍK, P. SCHOVANEK, *Laser scanning confocal microscopy in materials engineering*, Conference paper in Proceedings of SPIE- The International Society for Optical Engineering · December 2012
- [49] Phenom XL Specifications, Emit, <https://www.emitllc.com/sem-specs.html>, assessed 20/01/2021.
- [50] M. KANNAN, *Scanning Electron Microscopy: Principle, Components and Applications, A textbook on Fundamentals and Applications of Nanotechnology*, (2018)
- [51] Scanning Electron Microscopy A to Z, JEOL, https://www.jeol.co.jp/en/applications/pdf/sm/sem_atoz_all.pdf, assessed 20/01/2021.
- [52] Field Emission Scanning Electron Microscopy (FESEM), PhotoMetrics, <https://photometrics.net/field-emission-scanning-electron-microscopy-fesem/>, assessed 20/01/2021.
- [53] D. SEMNANI, Geometrical Characterization of electrospun nanofibers, *Electrospun Nanofibers*, (2017) p.151-180.
- [54] Vickers Hardness Test, Gordon England, <https://www.gordonengland.co.uk/hardness/vickers.htm>, assessed 20/01/2020.
- [55] Les essais des aciers, Construction et Travaux publics | Techniques du bâtiment : l'enveloppe du bâtiment, (2004)
- [56] G. M. MAHMOUD, R. S. HEGAZY, Comparison of GUM and Monte Carlo methods for the uncertainty estimation in hardness measurements, *International Journal of Metrology and Quality Engineering*, (2017) p.8-14.
- [57] V. KRÁLIK, J. NEMEČEK, Spherical nanoindentation applied to Aluminium foam, *International Conference – Engineering Mechanics*, (2013) p.323-329.
- [58] S. CHA, P. C. LIN, L. ZHU, E. L. BOTVINICK, P. SUN, Y. FAINMAN, 3D profilometry using a dynamically configurable microscope, *Three-dimensional image capture and applications II*, (1999)
- [59] Q. FLAMANT, F. G. MARRO, J. J. ROA ROVIRA, M. ANGLADA, Hydrofluoric acid etching of dental zirconia. Part 1: etching mechanism and surface characterization, *Journal of the European Ceramic Society*, 36 (2016) p.121-134.
- [60] Area Roughness Parameters, Keyence, <https://www.keyence.com/ss/products/microscope/roughness/surface/parameters.jsp>, assessed 20/01/2021.

- [61] SPIP Classic Roughness Parameters for Images, SPIP Reference Guide, http://www.imagemet.com/WebHelp6/Default.htm#RoughnessParameters/Roughness_Parameters.htm, assessed 20/01/2021.
- [62] T. ITOI, T. SEIMIYA, Y. KAWAMURA, M. HIROHASHI, Long period stacking structures observed in Mg₉₇Zn₁Y₂ alloy, *Scripta Materialia*, 51 (2004) p.107-111.
- [63] J. HAO, J. ZHANG, B. LI, R. XIE, Effects of 14H LPSO phase on the dynamic recrystallization and work hardening behaviors of an extruded Mg-Zn-Y-Mn alloy, *Materials Science and Engineering: A* (2020)
- [64] D. CIOBOATA, D. STANCIU, Equipments for High Precision Measurement of free form surfaces micro and macro geometry, *Mecahitech'11*, 3 (2011) p.297-303.
- [65] Station micromesure, STIL, <http://micromesure.stil-sensors.com/?lang=FR>, assessed 20/01/2021.
- [66] W. D. NIX, H. GAO, Indentation size effect in crystalline materials: a law for strain gradient plasticity, *Journal of the Mechanics and Physics of Solids*, 46 (1997) p.411-425.
- [67] E. BROITMAN, Indentation hardness measurements at macro-, micro-, and nanoscale: A critical review, *Tribology letters*, 65 (2017)
- [68] K.U. KAINER, *Magnesium Alloys and Technology* (2003) p.1.
- [69] Primary magnesium production worldwide from 2010 to 2019, Statista, <https://www.statista.com/statistics/569515/primary-magnesium-production-worldwide/>, assessed 20/01/2021.
- [70] U.S. Geological Survey, (2020)
- [71] Road.cc, <https://road.cc/content/tech-news/248587-allite-launches-super-magnesium-alloy-lighter-and-stiffer-aluminium-and>, assessed 20/01/2021.
- [72] Rare Earths, Minbos, minbos.com, assessed 20/01/2021.
- [73] Y.M. ZHU, A.J. MORTON, J.F. NIE, Growth and transformation mechanisms of 18R and 14H in Mg-Y-Zn alloys, *Acta Materialia*, 60 (2012) p.6562-6572.
- [74] Spectrographic, Struers LaboPress -3, <https://spectrographic.co.uk/products/struers-labopress-3>, assessed 20/01/2021.
- [75] C. S. KIM, S. H. AHN, D. Y. JANG, Review: Developments in micro/nanoscale fabrication by focused ion beams, *Vacuum*, 86 (2012) p.1014-1035.

[76] J. GIERAK, Focused Ion Beam nano-patterning from traditional applications to single ion implantation, *Nanofabrication*, 1 (2014) p.35-52.

[77] Z.L. WANG, J.L. LEE, *Developments in Surface Contamination and Cleaning*, 1 (2007) p.395-443

[78] Buehler, Manual abrasive Cutter, <http://www.horizonindia.in/buehler/abrasive-cutters/brochure-3.pdf>, assessed 20/01/2021

Annex

A1. EDS maps of the alloys

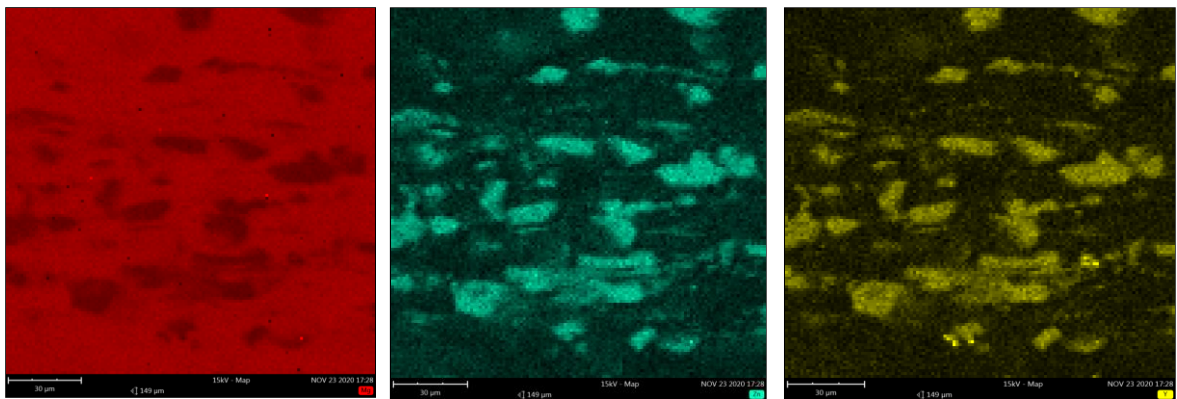


Figure A.1: EDS maps of S1L, Mg in red, Y in yellow, Zn in blue

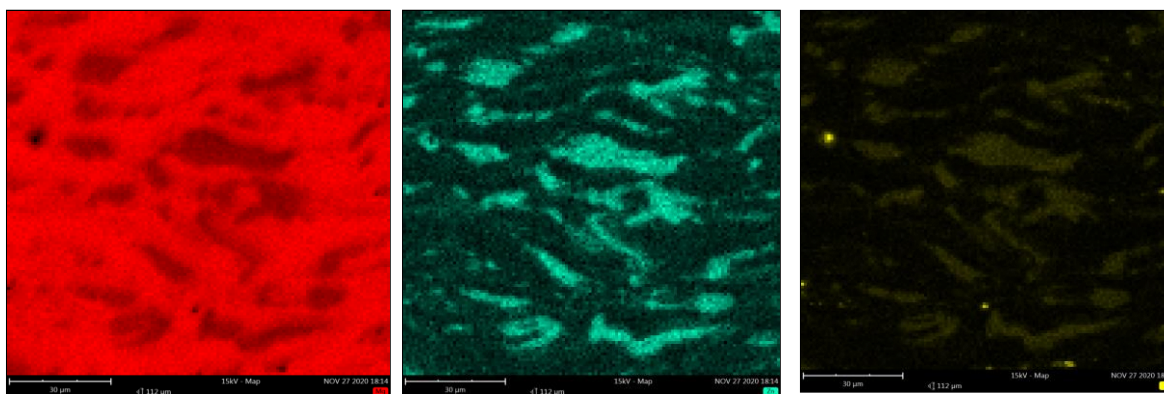
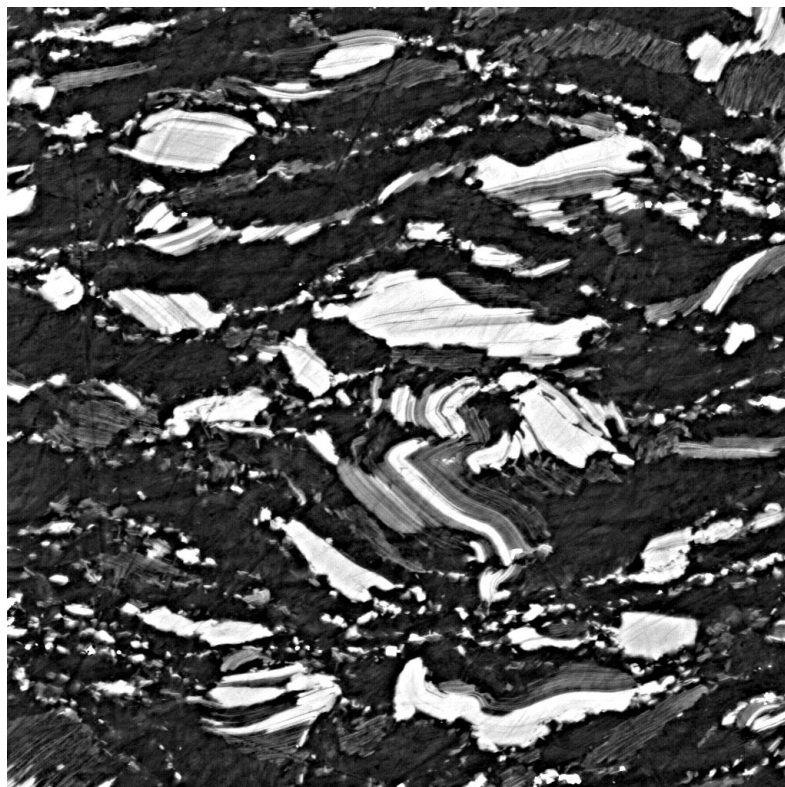


Figure A 2: EDS maps of S1T, Mg in red, Y in yellow, Zn in blue

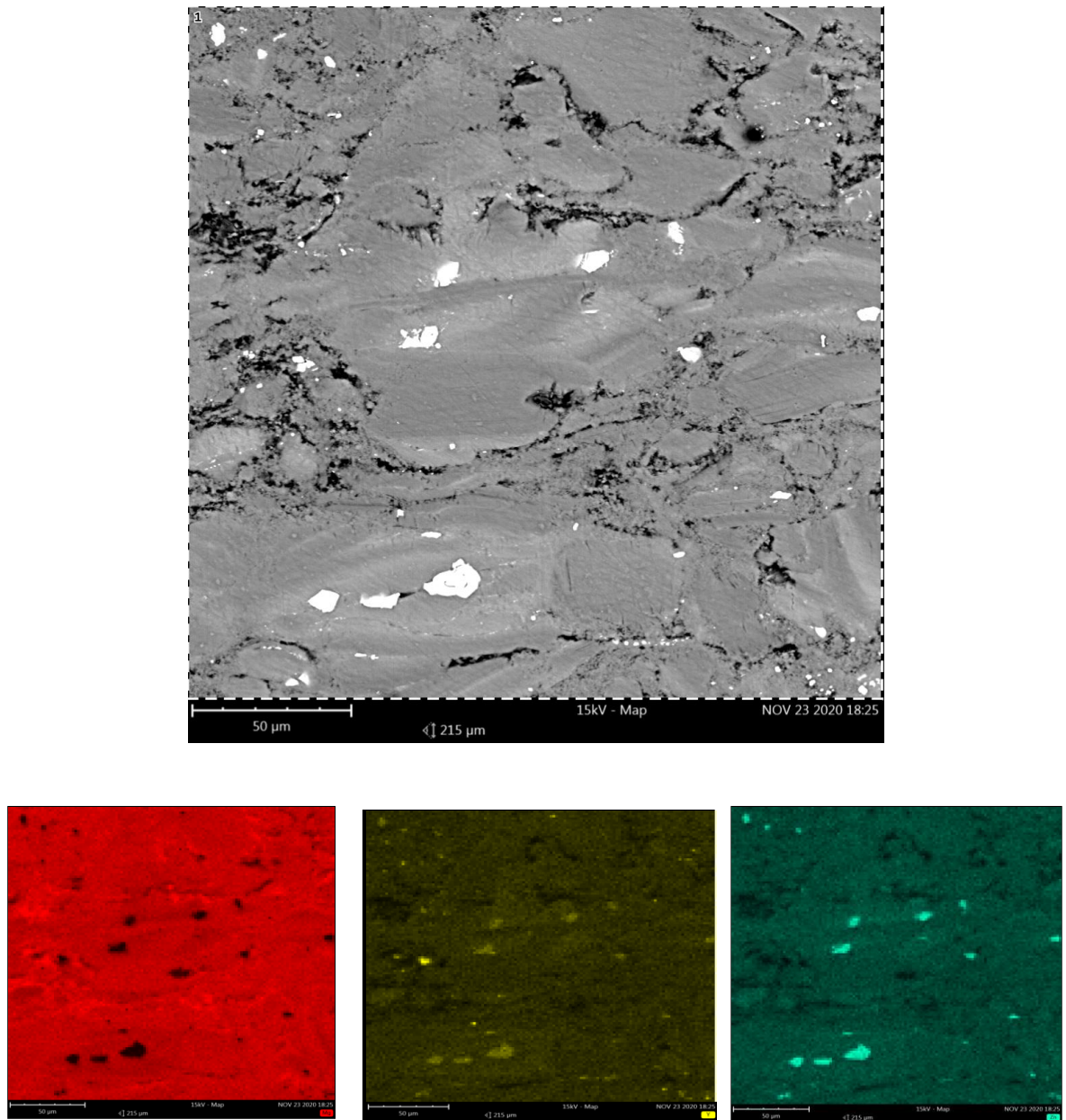


Figure A.3: EDS maps of S2L, Mg in red, Y in yellow, Zn in blue.

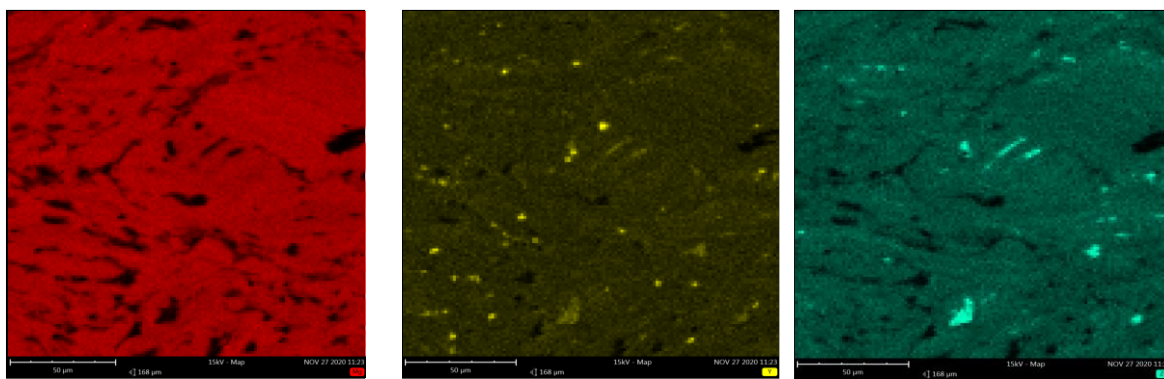
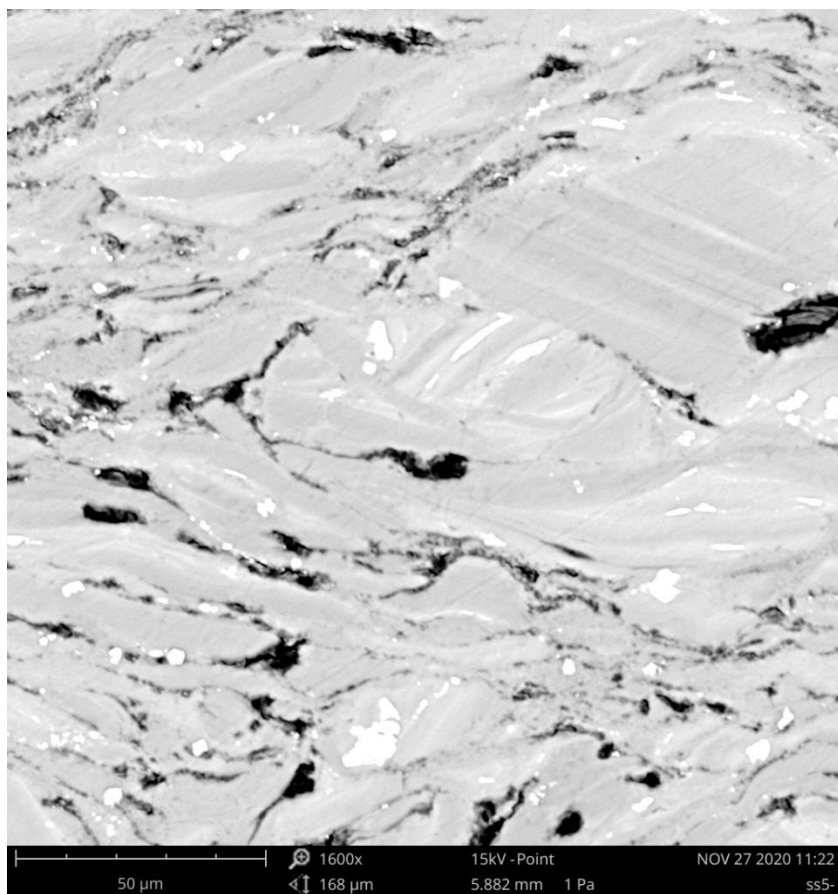


Figure A.4: EDS maps of S2T, Mg in red, Y in yellow, Zn in blue.

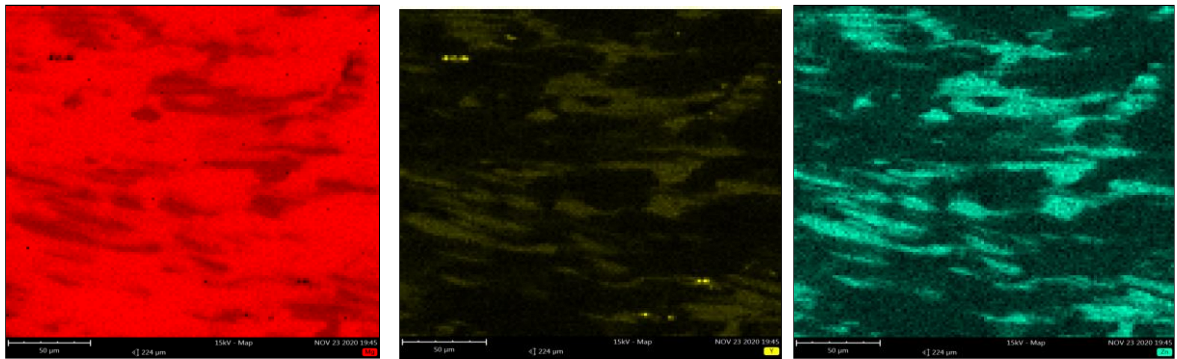


Figure A.5: EDS maps of S3L, Mg in red, Y in yellow, Zn in blue

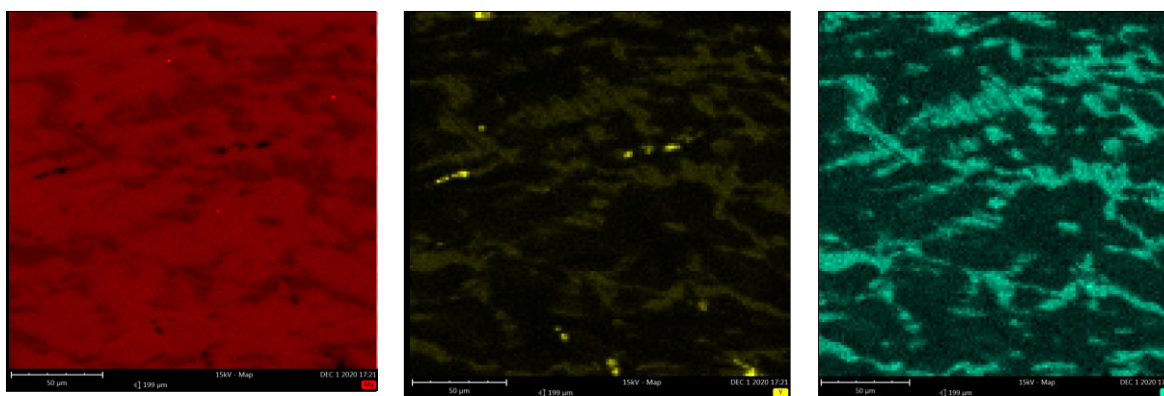
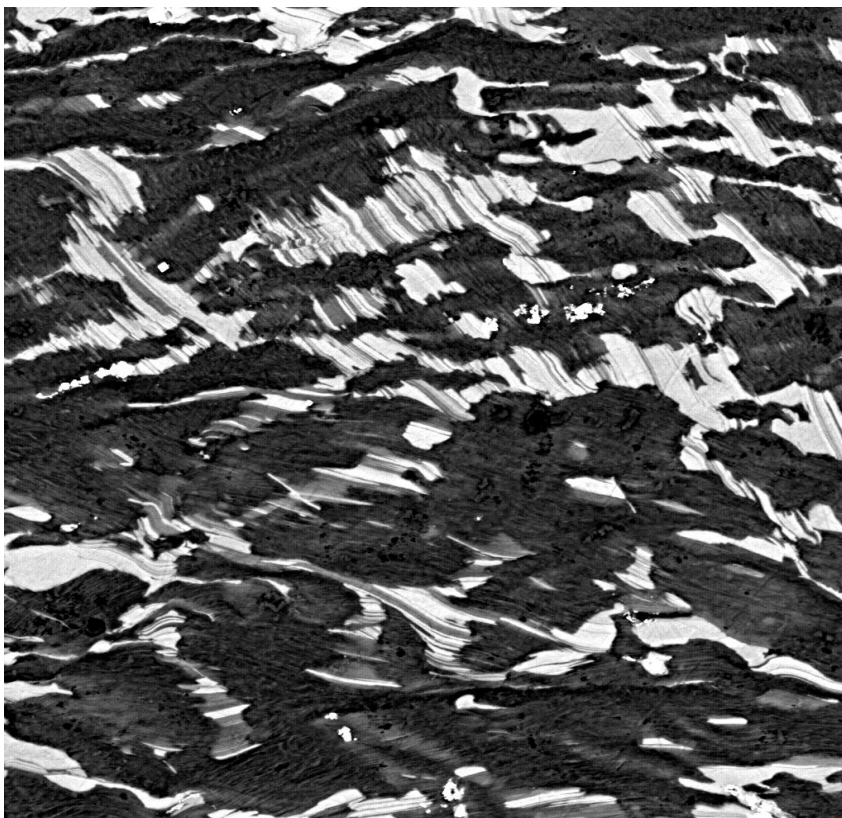


Figure A.6: EDS maps of S3T, Mg in red, Y in yellow, Zn in blue

A2. EDS point composition of the alloys

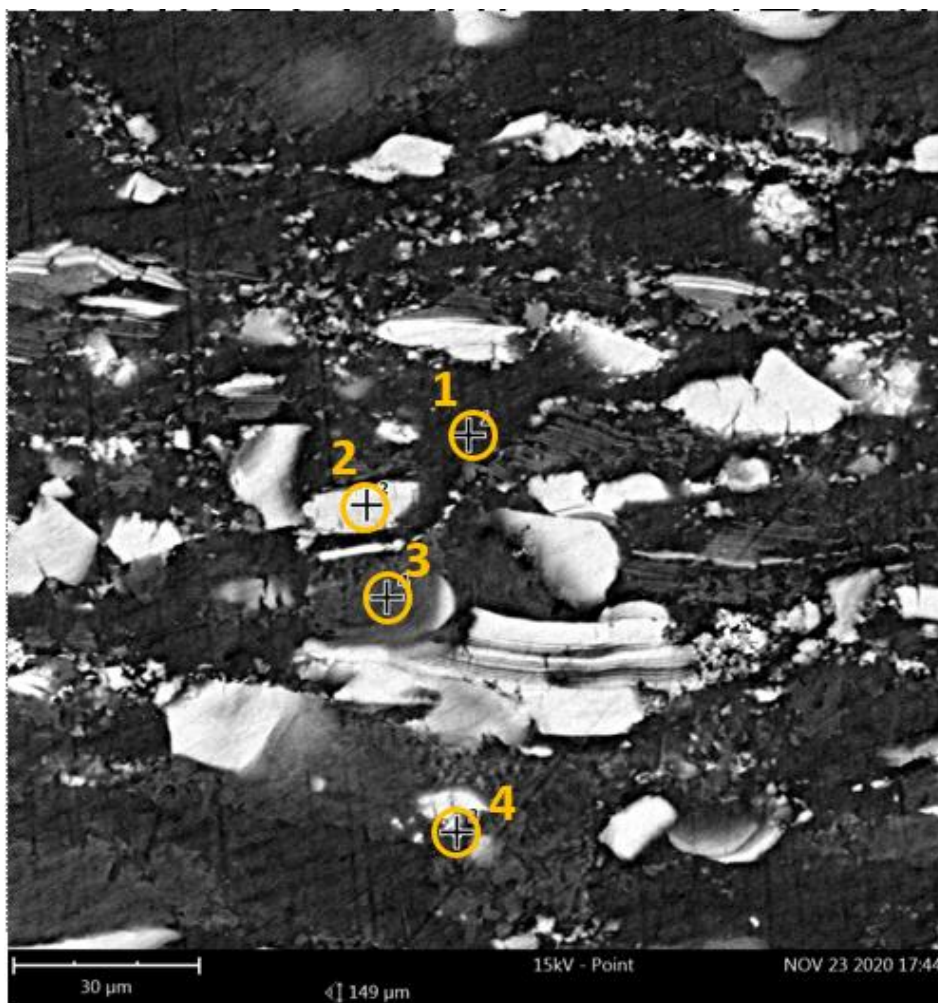


Figure A.7 : Point localization for EDS analysis on S1L.

Table A.1 : Elemental EDS composition of S1L

Element	Point 1	Point 2	Point 3	Point 4
Mg	100	89,59	80,35	98,89
Y	-	5,94	18,59	0,84
Zn	-	4,46	1,06	0,27

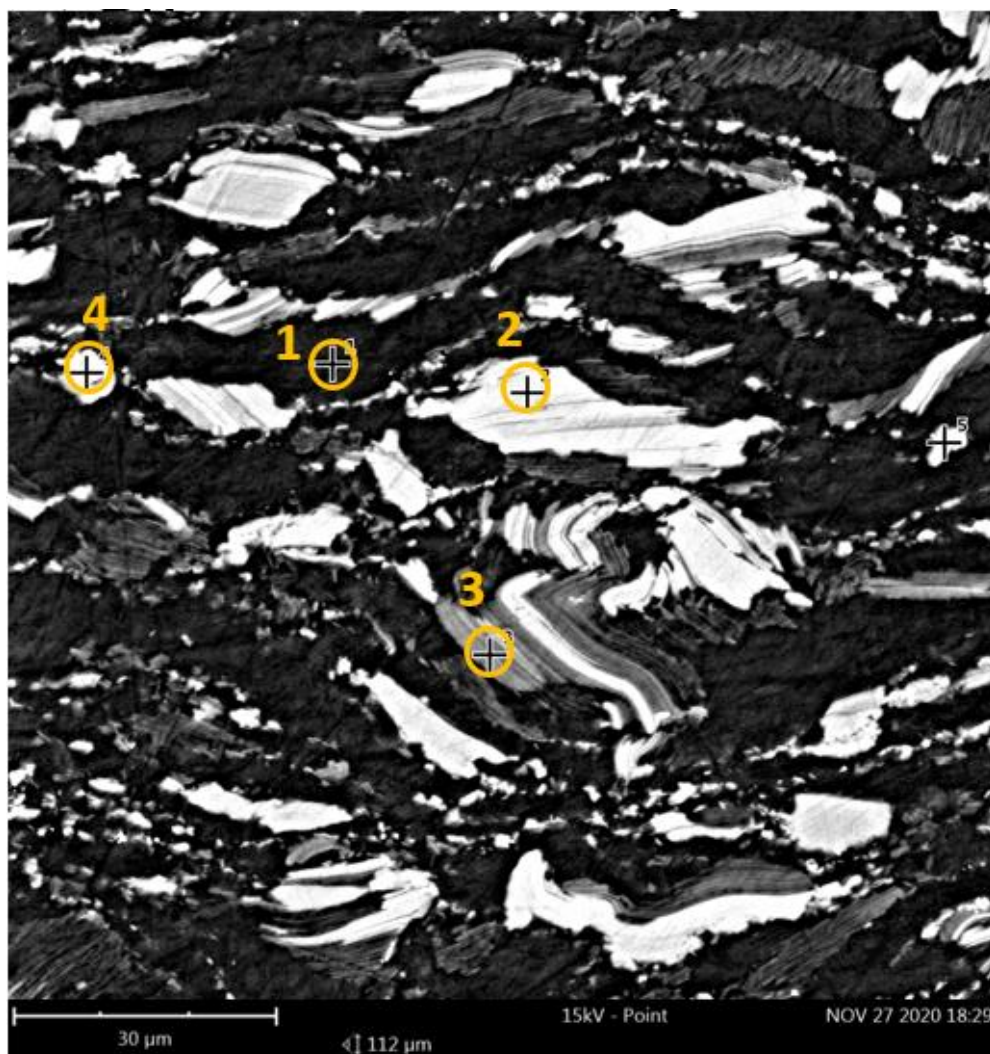


Figure A.8 : Point localization for EDS analysis on S1T

Table A.2 : Elemental EDS composition of S1T

Element	Point 1	Point 2	Point 3	Point 4	Point 5
Mg	100	87,46	95,44	50,41	89,78
Y	-	7,23	2,69	47,02	5,76
Zn	-	5,31	1,87	2,57	4,46

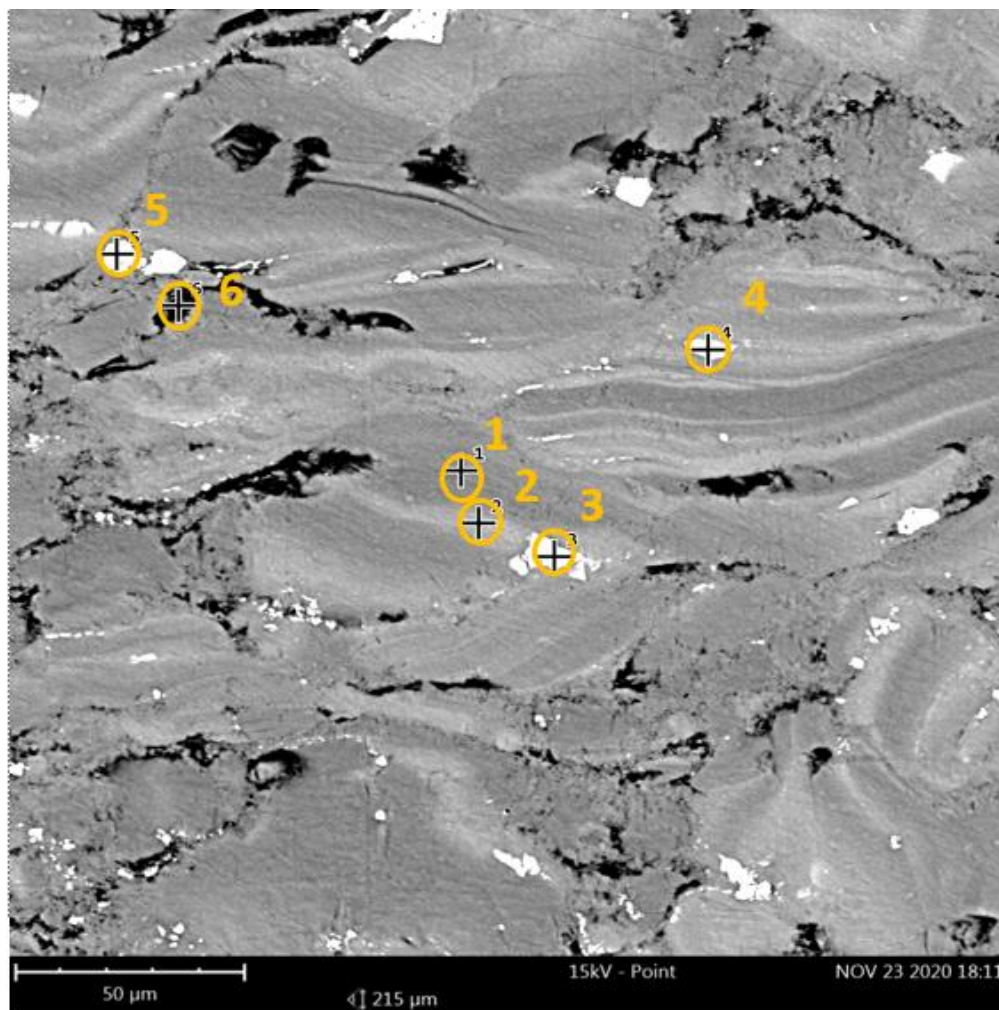


Figure A.9 : Point localization for EDS analysis on S2L

Table A.3 : Elemental EDS composition of S2L

Element	Point 1	Point 2	Point 3	Point 4	Point 5	Point 6
Mg	88,44	83,90	32,76	34,28	37,05	100
Y	6,45	8,67	25,76	25,88	24,34	-
Zn	5,11	7,43	41,51	39,84	38,60	-

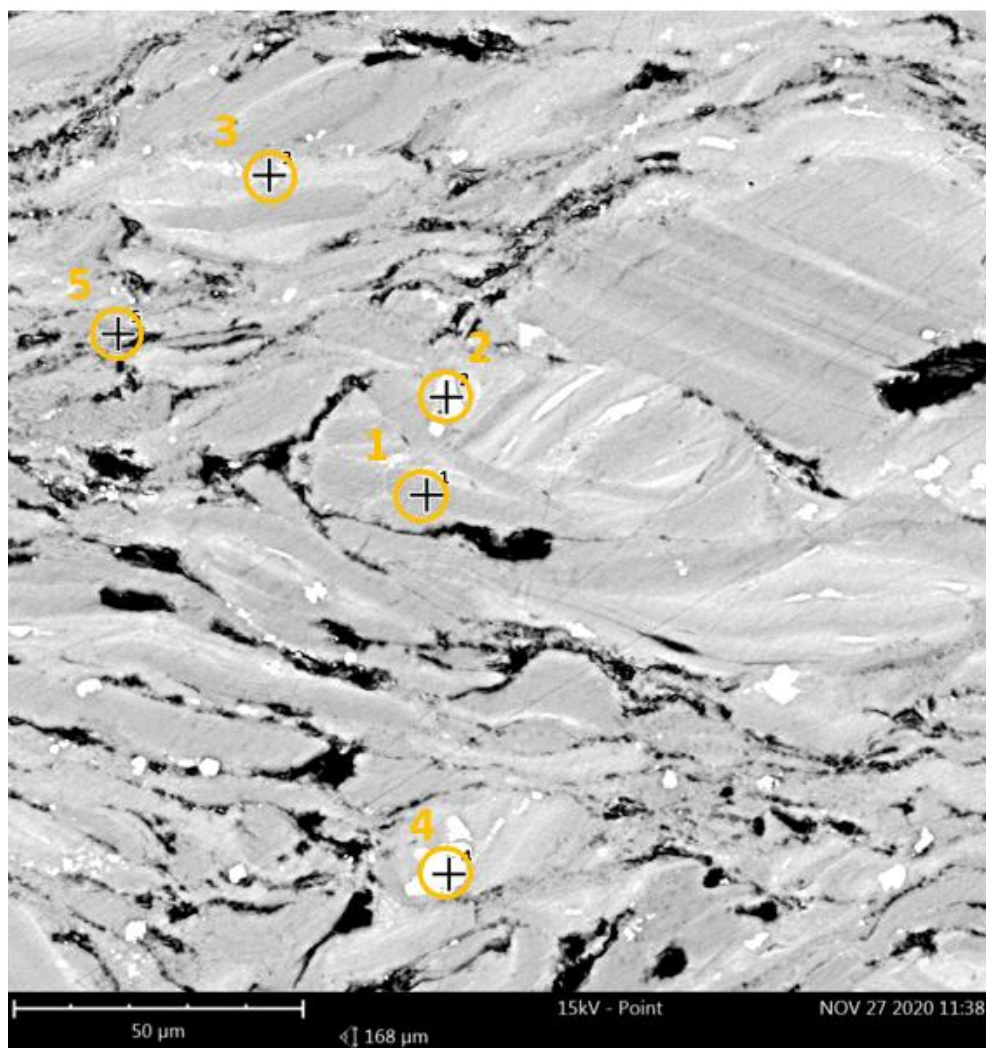


Figure A.10 : Point localization for EDS analysis on S2T

Table A.4 : Elemental EDS composition of S2T

Element	Point 1	Point 2	Point 3	Point 4	Point 5
Mg	88,17	42,00	60,86	37,64	44,81
Y	6,68	24,35	33,64	25,81	52,39
Zn	5,16	33,65	5,50	36,55	2,81

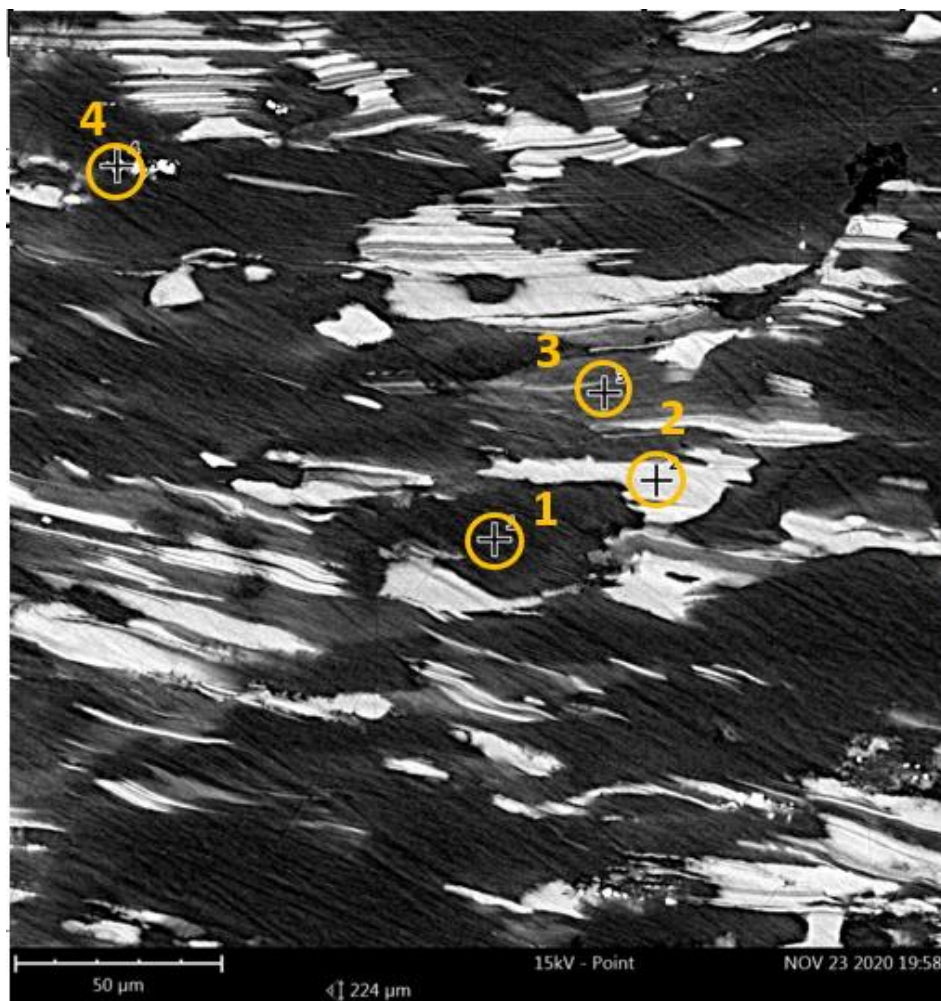


Figure A.11 : Point localization for EDS analysis on S3L

Table A.5 : Elemental EDS composition of S3L

Element	Point 1	Point 2	Point 3	Point 4
Mg	100	89,32	99,10	27,97
Y	-	6,01	-	71,15
Zn	-	4,67	0,90	0,89

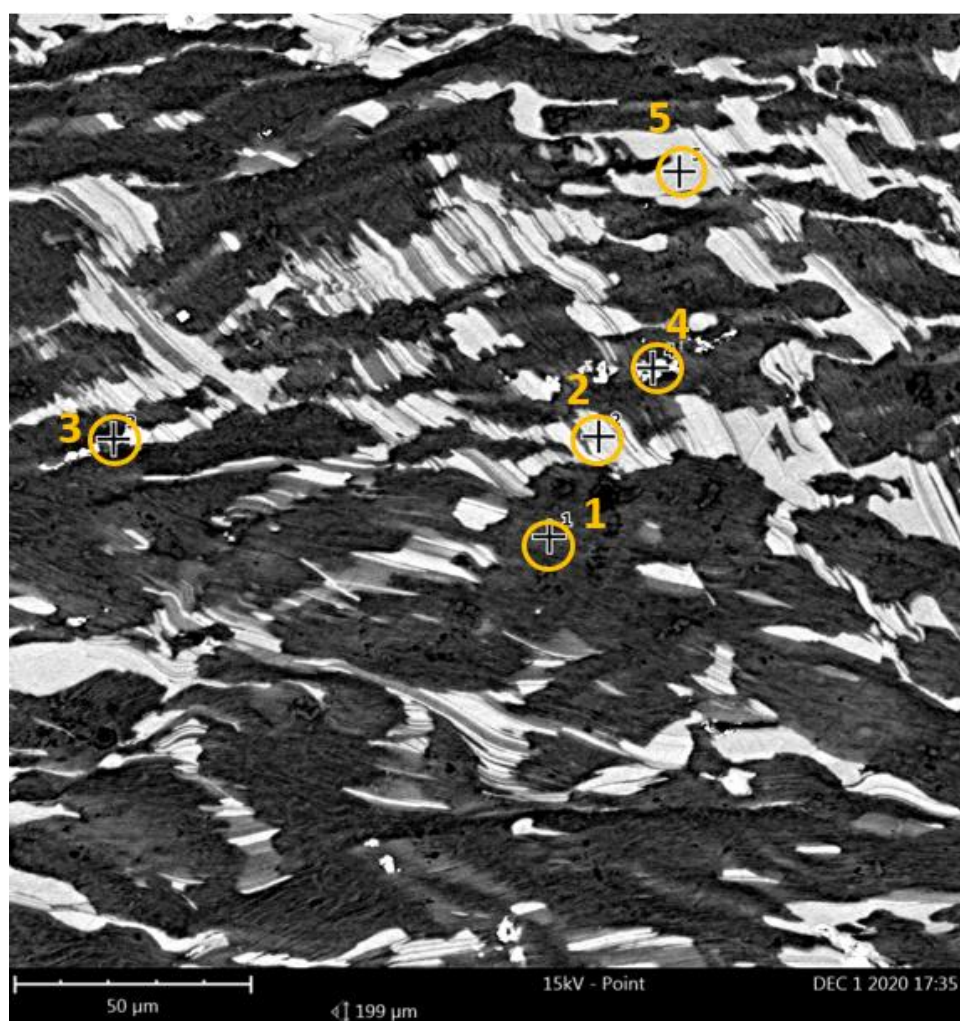


Figure A.12 : Point localization for EDS analysis on S3T

Table A.6 : Elemental EDS composition of S3T

Element	Point 1	Point 2	Point 3	Point 4	Point 5
Mg	100	89,63	56,66	30,18	90,09
Y	-	6,05	42,54	68,67	5,70
Zn	-	4,32	0,79	1,14	4,21

